UNIVERSITY OF ADELAIDE

THE UNIVERSITY
OF ADELAIDE
AUSTRALIA

DOCTORAL THESIS

Dual energy image reconstruction and systems for application in proton therapy treatment planning

JIAHUA ZHU

March 2017

Dual energy image reconstruction and systems for application in proton therapy treatment planning

A thesis submitted in fulfilment of the requirements for the degree of Doctor of Philosophy

Doctor of Philosophy

from

School of Physical Science

University of Adelaide

by

Jiahua Zhu

Supervisors:

Dr. Scott Penfold

Dr. Judith Pollard

Dr. Puthenparampil Wilson

2017

Declaration

I, Jiahua Zhu, certify that this work contains no material which has been accepted for the award of any other degree or diploma in my name, in any university or other tertiary institution and, to the best of my knowledge and belief, contains no material previously published or written by another person, except where due reference has been made in the text. In addition, I certify that no part of this work will, in the future, be used in a submission in my name, for any other degree or diploma in any university or other tertiary institution without the prior approval of the University of Adelaide and where applicable, any partner institution responsible for the joint-award of this degree.

I give consent to this copy of my thesis when deposited in the University Library, being made available for loan and photocopying, subject to the provisions of the Copyright Act 1968.

I acknowledge that copyright of published works contained within this thesis resides with the copyright holder(s) of those works.

I also give permission for the digital version of my thesis to be made available on the web, via the University's digital research repository, the Library Search and also through web search engines, unless permission has been granted by the University to restrict access for a period of time.

Name: Jiahua Zhu

Signed:

Date:

Acknowledgements

I would like to thank my principal supervisor, Dr. Scott Penfold, for his advice, guidance and continuous trust in my PhD project. His support and suggestions encouraged me to exploit the unknown knowledge and improve the comprehensive ability. I am deeply grateful for him not to abandon me when I was in dilemma and to support me to continue my project. His rigorous attitude on science influences me in pursuit of the scientific essence. The completion of my project includes his effort and contribution.

My appreciation also goes to Professor Eva Bezak for her encouragement and guidance. Thank her for giving me the opportunity to accomplish my dream. I would like to thank my supervisor, Dr. Judith Pollard for editing my paper and thesis. Her suggestions helped me make progress. I would also like to thank Dr. Puthenparampil Wilson for training me the clinical skills. I cannot realise the standard workflow of radiotherapy without his introduction and demonstration. A proved editor, Dr. Dana Thomsen, also engaged in the English writing revision.

I would like to thank my fellow graduate students Leyla Moghaddasi and Ruqaya Al Darwish. Their sincere attitudes and selfless shares gave me continuous support.

To my parents, Xiuhai Zhu and Lifang Guo, thank you for your spiritual and financial support throughout my research period. To my wife and children, He Wang, Chunying Zhu and Ruiheng Zhu, thank you all for your understanding and love without any condition. Your support is indispensable for me to accomplish my project.

Publications and Submitted Papers Contained Within Thesis

Published

P1. Zhu, Jiahua, and Scott N. Penfold. "Review of 3D image data calibration for heterogeneity correction in proton therapy treatment planning." Australasian Physical & Engineering Sciences in Medicine (2016): 1-12.

P2. Zhu, Jiahua, and Scott N. Penfold. "Dosimetric comparison of stopping power calibration with dual-energy CT and single-energy CT in proton therapy treatment planning." Medical Physics 43.6 (2016): 2845-2854.

P3. Zhu, Jiahua, and Scott N. Penfold. "Total Variation Superiorization in Dual-energy CT Reconstruction for Proton Therapy Treatment Planning" Inverse Problem, Vol 33, No.4 (2017)

Submitted

P4. Zhu, Jiahua, and Scott N. Penfold. "Europium-155 as a source for dual energy cone beam computed tomography in adaptive radiotherapy: a simulation study" Submitted to Medical Physics

These publications and papers submitted are included within this thesis. When referred to in the text the reference number is prefixed by a ‘P’. For example, the first publication in this list is referred to P1.

Grants and Scholarships

- Australasian College of Physical Scientists and Engineers in Medicine (ACPSEM) Student Scholarship to attend the annual Engineering and Physical Sciences in Medicine (EPSM) Meeting 2013.
- Chinese Government Award for Outstanding Self-financed Students Abroad 2016

Conference Presentations

- Zhu J., Penfold S., *An Alternative Material Definition Scheme for Monte Carlo Radiotherapy Dose Calculation*, EPSM 2013, Perth, Australia

- Zhu J., Penfold S., *Investigation Into Robustness of Stopping Power Calculated by DECT and SECT for Proton Therapy Treatment Planning,* AAPM Annual Meeting, 2015, Anaheim, CA, USA

Other Presentation

- Zhu J., Penfold S., *The optimization of dose calculation by DECT in proton therapy*, ACPSEM Student Night 2015, Adelaide, Australia [Second Prize]

- Zhu J., Penfold S., *Effective atomic number calculation by DECT*, ACPSEM Student Night 2014, Adelaide, Australia [Second Prize]

Abstract

Proton therapy is the use of a proton beam rather than a traditional X-ray beam in the treatment of cancer. This technique is being developed all over the world due to the unique Bragg peak feature of proton beams. In order to guarantee accurate dose delivery to the tumour, the stopping power ratio (SPR) of the tissue must be known. This parameter is dependent on the electron density and effective atomic number of the material and describes the energy loss per unit length in the tissue. In current clinical practice, the SPR of patient tissues is obtained through single energy CT (SECT) scanning. The SECT scan results in a map of kilovoltage X-ray attenuation coefficients relative to the attenuation coefficient of water for the beam energy. This quantitative information is then converted to SPR via an empirically derived look-up table. If the patient tissues do not have a similar chemical composition to the materials used to generated the look-up table, this approach can lead to diminished dose calculation accuracy. As a result, the patient may experience increased normal tissue complication or decreased tumour control probability. An alternative approach that has been suggested recently is the use of dual energy CT (DECT).

DECT is an emerging imaging modality that makes use of CT spectra to create two sets of CT images simultaneously. DECT relies on the energy independence of relative electron density, and the energy and atomic number dependence of X-ray interaction atomic cross-sections. Post processing of the two reconstructed CT images results in two separate images quantifying electron density and effective atomic number. The SPR of the tissue can be calculated once electron density and effective atomic number are known. In theory, the use of DECT for SPR estimation should be more robust than SECT combined with an empirically derived look-up table. This hypothesis has been tested with phantoms of known composition in the current work.

Unfortunately, the post processing of DECT images results in effective atomic number images with a low contrast to noise ratio, which can affect SPR calculation accuracy. To counteract this, an iterative DECT image reconstruction approach has been developed. Two image reconstruction algorithms, FBP and TVS-DROP, are implemented to reconstruct the

CT images, where an advanced parallel calculation code was designed for TVS-DROP to improve work efficiency. The iterative reconstruction algorithm was also applied to a radioisotope form of cone beam DECT. A feasibility study into the use of this novel imaging method in adaptive proton therapy was conducted.

In summary, the objective of this thesis is to examine the application of DECT for proton therapy treatment planning, develop improved image reconstruction techniques for DECT, and investigate the feasibility of a novel radioisotope-based form of cone beam DECT for adaptive proton therapy.

Table of Contents

Chapter 1

Introduction

1.1 Development of proton therapy

Proton therapy is the use of proton beams in the treatment of tumours. Robert Wilson[1] first proposed the feasibility of using proton beams for cancer treatment while involved in the design of the Harvard Cyclotron Laboratory[2], citing the therapeutic potential of the Bragg peak, a unique characteristic of a charged particle beam. In order to extend the high dose region to cover the whole tumour volume, the Bragg peak is spread out with energy and intensity modulation. The result is a uniform high dose over the target volume before descending to almost zero after the target volume (Fig. 1). Therefore, a proton beam is able to accumulate a high radiation dose in deep-seated tumours and reduce the dose in surrounding normal tissues.

Since the first patient to receive proton therapy was treated at the University of California, Berkeley[4], the number of proton machines has increased to over 70 proton or ion machines in operation[5] globally and more than 150,000 patients having received charged particle therapy[6].

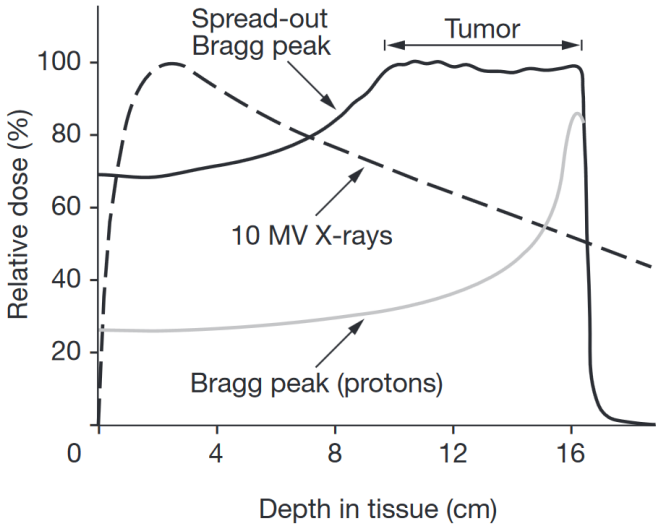

Figure 1. Percentage depth dose for protons and X-rays. The solid line is the spread-out Bragg peak (SOBP), the dashed line corresponds to a 10MV X-ray beam and the grey line is a pristine Bragg peak[3].

1.2 Single energy CT in proton therapy

To accurately plan a proton therapy treatment, information about the patient anatomy is required. This information is used to define target tissues, avoidance tissues and also to perform dose calculation. For the latter, details of the chemical composition and density of each 3D image voxel are required. Single energy computed tomography (SECT) is currently the method of choice for obtaining this information.

The data contained in a SECT relates to the rate of attenuation of kilovoltage X-rays in human tissue. This cannot be used directly for proton therapy dose calculation. For proton therapy, stopping power in each image voxel is required. The stopping power of protons in

the therapeutic energy range (<300 MeV) for a given material can be calculated with the Bethe[7] equation.

For practicality, the stopping power ratio (SPR) is used for treatment planning as this parameter is energy independent to a good approximation. The SPR is simply the ratio of stopping power of a given material to the stopping power of water at a given energy. To convert CT data to SPR, the stoichiometric calibration technique of Schneider and Pedroni[8] is typically used. This method constructs a calibration curve between CT number and SPR by chemical compositions and densities of standard tissues from ICRU44[9].

The stoichiometric calibration method reduces systematic errors caused through the direct calibration of a CT scanner with tissue substitute materials as these materials typically do not have the same Z and Z/A properties as real tissues. This method does, however, assume that individual patient tissues can be well approximated by a representative average tissue dataset, such as ICRU 44. It is known that tissue composition varies with age, sex and health status[9]. Therefore, a more favourable approach to SPR calibration would utilize an imaging technique that can produce quantities more closely related to material specific parameters. Dual energy computed tomography (DECT) is one such imaging modality.

1.3 Dual energy CT in proton therapy

DECT was first proposed by Rutherford *et al*[10] in 1976. The potential applications to radiotherapy treatment planning lie in its ability to decompose human tissue into electron density (ρ_e) and effective atomic number (Z_{eff}). These tissue properties can be used for dose calculation in all ionizing radiation beam types. Despite being proposed four decades ago, the potential applications of DECT to radiotherapy treatment planning are only now being

widely explored. The use of DECT in proton therapy is particularly attractive as the advantages of treating with a Bragg peak can only be fully realised if the range of protons in human tissues can be calculated with a high degree of accuracy.

The SPR is dependent upon the mean excitation energy (I) and electron density (ρ_e) of tissues. The mean excitation energy is known to depend on atomic number of the absorbing material. Thus, if effective atomic number (Z_{eff}) is used to calculate I, the SPR can be obtained. Two approaches have been described for SPR calculation with DECT. Yang *et al*[11] were the first to propose an empirical relationship between Z_{eff} obtained from DECT and mean excitation energy. Using this relationship and the electron density obtained directly from DECT, one has all parameters required to calculate stopping power. The second approach is based on the allocation of reference tissues to a given voxel using a predefined look-up table based on the measured electron density and effective atomic number.

1.4 Influence of image reconstruction algorithms in proton therapy

A limitation of DECT is that any noise in the reconstructed images is amplified in the calculation of effective atomic number[12]. DECT images reconstructed with filtered backprojection typically result in poor contrast when examining the effective atomic number distribution. To counter this, iterative reconstruction algorithms with noise suppression should be considered. One such algorithm known as total variation superiorization with diagonally relaxed orthogonal projections (TVS-DROP) has already been applied in proton computed tomography (pCT) reconstructions with promising results. The application of this reconstruction algorithm to DECT for the purpose of SPR reconstruction was investigated as part of this thesis.

1.5 Dual energy cone beam CT in proton therapy

To fully exploit the physical advantages of proton therapy, the geometry and SPR of patient tissues at the time of treatment should be known with a high degree of accuracy. Cone beam computed tomography (CBCT) is a popular tool for obtaining three dimensional geometrical information at the time of treatment in X-ray therapy. In more advanced treatment workflows, CBCT can also be used as a tool for dose accumulation studies and offline adaptive radiotherapy[13, 14]. Despite the widespread use of cone beam computed tomography (CBCT) in conventional X-ray radiotherapy, this technology is only now becoming a standard offering of proton therapy vendors.

Dual energy CBCT (DECBCT) refers to an imaging device with two cone beams of photons of different energies, capable of reconstructing two sets of CT images simultaneously. The aim of studying DECBCT is to obtain a SPR map prior to proton therapy treatment delivery, monitor the actual dose delivery over the course of treatment, and potentially allow for online adaptive therapy proton dose calculations.

Although DECBCT has significant potential for application in proton therapy, no clinical sites are making use of such a device. A novel approach to this form of imaging, making use of a radioisotope with dual energy emissions and a pixelated spectroscopic detector, is described in Chapter 5.

1.6 Structure of the thesis

As described above, proton therapy treatment currently includes uncertainties relating to the use of SECT information for dose calculation during treatment planning. The aim of this

project is to demonstrate the benefits of DECT and optimize its use in proton therapy treatment planning.

This thesis is comprised of two publications and two submitted papers listed on page iii. Each Chapter includes a foreword and the original publication.

Chapter 2 contains a literature review of data calibration for inhomogeneous correction in dose calculation for proton therapy. Different methods to translate image data to interaction parameters of interest are summarised and implementations in commercial proton TPSs are also reviewed.

Chapter 3 contains a dosimetric comparison of SPR with DECT and SECT approaches and the implementation of dose deposition calculation in a commercial proton TPS. This work simulated a clinical process with DECT and compared dose deposition with that of SECT. The novelty of this paper lies in the evaluation of DECT accuracy for dose calculation.

Chapter 4 contains an investigation into image reconstruction algorithms and their influence on the dose calculation accuracy in proton therapy. This chapter is an extension of Chapter 3 and answers the question of how to improve dose calculation accuracy when DECT is applied in proton therapy.

Chapter 5 details a feasibility study into a novel DECBCT system with a radioactive material as the source. The system utilizes a unique source to obtain two monoenergetic signals on a spectroscopic pixelated detector panel. The image reconstruction algorithm proposed in Chapter 4 is also used here. An analysis of the accuracy of the reconstructed images is presented and the potential applications to adaptive proton therapy discussed.

Chapter 6 contains a conclusion and summary of the thesis. A discussion of future work which may improve the accuracy of proton treatment is also provided.

Chapter 2

Literature review of 3D image calibration for heterogeneity correction in proton therapy treatment planning

The following forms the basis of this chapter.

Zhu, Jiahua, and Scott N. Penfold. "Review of 3D image data calibration for heterogeneity correction in proton therapy treatment planning." Australasian Physical & Engineering Sciences in Medicine (2016): 1-12.

2.1 Introduction and motivation

The stopping power ratio (SPR) of tissue directly influences the dose deposition calculation in proton therapy treatment planning. The traditional approach to converting CT numbers to SPR carries with it an assumption that a given patients' tissues have a similar chemical composition and density to the materials used to generate the conversion function. However, this conversion inevitably has potential risk to incur the error due to the unknown chemical composition and the electron density of the real tissue. Therefore, it is important that alternate imaging methods such as dual energy CT and proton CT are considered.

In this chapter, proton interactions with tissues are introduced. Stopping power, scattering power and nuclear interactions are compared and the weight of each term to the entire dose deposition are described. Furthermore, the tissue parameterization and tissue decomposition employed for proton dose calculation are also analysed within single energy CT, dual energy CT and proton CT. Finally, the current CT calibration methods employed in commercial proton treatment planning system are reported.

2.2 Statement of Contribution

2.2.1 Conception

The idea to review 3D image data calibration in proton therapy treatment planning systems was first proposed by Scott Penfold. The process to compare and analyse the different approaches were conceptualised by Jiahua Zhu and Scott Penfold.

2.2.2 Realisation

This chapter was developed by Jiahua Zhu. The drawings and tables were copied or redrawn by Jiahua Zhu. The work to review and summarise papers was conducted by all authors.

2.2.3 Documentation

This paper was primarily written by Jiahua Zhu. Editing was performed by all authors. Dr. Judith Pollard also engaged in the editing work.

Statement of Authorship

Title of Paper	Review of 3D image data calibration for heterogeneity correction in proton therapy treatment planning
Publication Status	☑ Published ☐ Accepted for Publication ☐ Submitted for Publication ☐ Unpublished and Unsubmitted w ork w ritten in manuscript style
Publication Details	Zhu, Jiahua, and Scott N. Penfold. "Review of 3D image data calibration for heterogeneity correction in proton therapy treatment planning." Australasian Physical & Engineering Sciences in Medicine (2016): 1-12.

Principal Author

Name of Principal Author (Candidate)	Jiahua Zhu
Contribution to the Paper	Collected and reviewed the papers. Chose the related papers to group and analyse for writing. Wrote the manuscript and acted as corresponding author.
Overall percentage (%)	70%
Certification:	This paper reports on original research I conducted during the period of my Higher Degree by Research candidature and is not subject to any obligations or contractual agreements with a third party that would constrain its inclusion in this thesis. I am the primary author of this paper.
Signature	Date 30/10/16

Co-Author Contributions

By signing the Statement of Authorship, each author certifies that:

i. the candidate's stated contribution to the publication is accurate (as detailed above);

ii. permission is granted for the candidate in include the publication in the thesis; and

iii. the sum of all co-author contributions is equal to 100% less the candidate's stated contribution.

Name of Co-Author	Scott Penfold
Contribution to the Paper	Supervised development of work and helped in manuscript evaluation.
Signature	Date 31/10/16

Name of Co-Author	
Contribution to the Paper	
Signature	Date

Please cut and paste additional co-author panels here as required.

Australas Phys Eng Sci Med (2016) 39:379–390
DOI 10.1007/s13246-016-0447-9

REVIEW

Review of 3D image data calibration for heterogeneity correction in proton therapy treatment planning

Jiahua Zhu[1] · **Scott N. Penfold**[1,2]

Received: 23 December 2015 / Accepted: 18 April 2016 / Published online: 26 April 2016

Abstract Correct modelling of the interaction parameters of patient tissues is of vital importance in proton therapy treatment planning because of the large dose gradients associated with the Bragg peak. Different 3D imaging techniques yield different information regarding these interaction parameters. Given the rapidly expanding interest in proton therapy, this review is written to make readers aware of the current challenges in accounting for tissue heterogeneities and the imaging systems that are proposed to tackle these challenges. A summary of the interaction parameters of interest in proton therapy and the current and developmental 3D imaging techniques used in proton therapy treatment planning is given. The different methods to translate the imaging data to the interaction parameters of interest are reviewed and a summary of the implementations in several commercial treatment planning systems is presented.

Keywords Proton therapy · Heterogeneity correction · Dual-energy CT · Proton CT

Introduction

Treatment planning in radiation therapy (RT) plays a pivotal role in determining the dose received by a patient during treatment. Accurate delivery of the prescribed dose is dependent upon accurate dose calculation during treatment planning. While radiation transport calculations in homogeneous materials can be carried out accurately and efficiently, calculations in heterogeneous materials can be problematic [1–3]. This is true for any treatment modality. Proton therapy however, is particularly susceptible to uncertainties in dose calculation due to heterogeneities [4, 5].

Therapeutic protons are energetic charged particles that undergo electromagnetic interactions with the electrostatic field of atomic electrons and nuclei and also nuclear interactions [6, 7]. The energy loss associated with ionization of atomic electrons plays the largest role in determining the dose distribution of a proton beam. However, multiple Coulomb scattering, large angle elastic nuclear scattering and proton fluence attenuation via inelastic and nonelastic nuclear interactions also have an effect on the spatial distribution of deposited dose [6].

Because of the overriding importance of determining the Bragg peak location for a given treatment beam, proton treatment planning systems (TPSs) have until recently attempted only to determine the water equivalent path length (WEPL) of patient tissues [8, 9]. Differences in mass scattering power and nuclear interactions between water and patient tissues were ignored. With advances in image-guided radiotherapy, emphasis is again being placed on improved dose calculation accuracy to facilitate PTV margin reductions. Recent studies have proposed methods for inclusion of more accurate models of scattering power and nuclear interactions into analytical dose calculation [10].

Advances in dose calculation algorithms have in turn led to the need for more accurate determination of the dosimetric properties of human tissues. Irrespective of the sophistication of the radiation transport model, if the dosimetric properties of human tissues are poorly estimated, errors will result [4, 11]. The methods used to

✉ Jiahua Zhu
jiahua.zhu@adelaide.edu.au

[1] Department of Physics, University of Adelaide, Adelaide, SA 5005, Australia

[2] Department of Medical Physics, Royal Adelaide Hospital, Adelaide, SA 5000, Australia

model the dosimetric properties of human tissues may be subdivided into two broad categories: tissue parameterization and tissue decomposition. Tissue parameterization techniques utilize a continuous, usually empirically derived, calibration function to link the 3D imaging quantitative data with the proton dosimetric parameters of interest, see for examples [8, 12, 13]. Tissue decomposition techniques attempt to estimate the chemical composition and density of each voxel and determine the interaction parameters for these compositions, see for examples [14–17].

The focus of this review article is on the methods used to approximate the dosimetric properties of human tissues for proton therapy treatment planning. A summary of the interaction parameters of interest in proton therapy and the current and developmental 3D imaging techniques used in proton therapy treatment planning is given. The different methods to translate the imaging data to the interaction parameters of interest are reviewed and a summary of the implementations in several commercial TPSs is presented.

Proton interaction parameters

Stopping power

In the therapeutic energy range, proton energy loss is dominated by electromagnetic interactions with atomic electrons. The collisional electronic stopping power (S), or the rate of energy loss dE per unit length of a material dx due to these interactions can be approximated by the Bethe-Bloch formula (Eq. 1) [18].

$$S = -\frac{dE}{dx} = \frac{4\pi}{\beta^2} r_e^2 m_e c^2 \rho_e \left[\ln\left(\frac{2m_e c^2}{I} \frac{\beta^2}{1-\beta^2} \right) - \beta^2 \right] \quad (1)$$

Here, β is the velocity of the particle relative to the speed of light c, r_e is the classical electron radius, m_e is the electron rest mass, ρ_e is the number of electrons per unit volume, and I is the mean excitation energy of the material. The shell correction, which accounts for the assumption that the proton is travelling at a significantly higher velocity than the orbital electron, has been neglected in Eq. (1). This correction becomes significant at low proton energies and more so for larger atomic number absorbers. The correction has a negligible effect when calculating energy deposition in pixel sizes on the order of millimetres. According to Eq. (1), therefore, when dealing with inhomogeneous materials one must know the electron density and mean excitation energy in order to calculate the stopping power for a given proton energy.

In analytical dose calculation algorithms, it is more common to make use of the stopping power *ratio*, SPR. Here, the stopping power is divided by the stopping power of a reference material (most commonly water) at each kinetic energy. However, whether absolute or relative stopping powers are being considered, knowledge of the electron density and mean excitation energy of a material is required.

Scattering power

All charged particles are subject to Coulombic interactions with the orbital electrons and nuclei of materials through which they pass. The majority of interactions are elastic, small angle scattering deflections. The root mean square (RMS) multiple Coulomb scattering (MCS) angle of protons as they traverse a slab is well described by Moliere's theory [19]. However, different MCS theories are required for quantities of interest other than the rms scattering angle. The Fermi-Eyges theory of MCS [20, 21] provides the charged particle number density at a given location with a given trajectory. For thick absorbers, the Fermi-Eyges distribution is Gaussian in shape.

The Fermi-Eyges theory includes a material specific parameter known as scattering power. The scattering power (T) of a material characterises the mean scattering angle per unit path length of a material at a given energy. A review of scattering power models relevant to therapeutic proton beams can be found in Kanematsu and Gottschalk [22, 23]. As described in [23], the model of scattering power provided by ICRU 35 [24] is a reasonable representation of MCS in low atomic number materials. Gottschalk made some proton specific simplifications to the ICRU 35 formalism and summarized the scattering power as [23].

$$T = \left(\frac{E_s}{pv} \right)^2 \frac{1}{X_s} \quad (2)$$

$$E_s = \left(\frac{2\pi}{\alpha} \right)^{1/2} m_e c^2 = 15.0 \text{ MeV} \quad (3)$$

$$\frac{1}{X_s} = \alpha r_e^2 \rho_e Z \left\{ 2 \log\left(33219 (AZ)^{-1/3} \right) - 1 \right\} \quad (4)$$

where X_s is a parameter known as the scattering length, α is the fine structure constant, p and v are the proton momentum and velocity respectively, A is the atomic weight, Z denotes the atomic number, and all other parameters are as defined in Eq. (1). When calculating the scattering power for composite materials, Eq. (5) may be applied [23], where w_j is the fraction by weight of the j-th constituent and ρ is the mass density.

$$\frac{1}{\rho X_s} = \sum_j w_j \left(\frac{1}{\rho X_s} \right)_j \quad (5)$$

To incorporate scattering power into the dose calculations of a treatment planning system, it is once again convenient to define $\hat{T}$ as the scattering power relative to the scattering power of water at a given energy. Since Eq. (5) does not contain any kinetic energy dependent terms, $\hat{T}$ by this definition is independent of proton energy. Now, the energy dependent scattering power of water can be scaled by $\hat{T}$ of the material through which the proton beam passes to calculate both the lateral and angular dispersion.

From Eq. (4) it is apparent that for determination of $\hat{T}$, knowledge of the electron density, effective atomic number and effective atomic weight of the material are required. This is different to the requirements for stopping power calculated with Eq. (1). Therefore, a different relationship between X-ray CT data and SPR can be expected than that obtained for X-ray CT data and $\hat{T}$.

Nuclear interactions

The primary effect of nuclear interactions in proton therapy dose calculation is that of attenuation of the proton fluence. However, as pointed out by Fippel and Soukup [25], the probability of nuclear reactions compared to ionization interactions is less than 5 % for 50 MeV protons and less than 1 % for 200 MeV and can therefore be considered as a correction to the primary energy loss mechanism of electronic stopping power.

The macroscopic cross-sections for nuclear interactions of protons with the main elemental constituents of soft tissues (carbon, nitrogen and oxygen) are on the same order of magnitude [26]. Furthermore, the approximate weight of hydrogen in soft tissues (9–12 %) [27] is approximately equal to that of water and thus the effect of assuming soft tissue consists of water when modelling proton nuclear interactions results in negligible errors in the proton dose calculation [25]. The cross-sections for nuclear interactions between protons and calcium are significantly smaller than for oxygen, which can result in cross-section errors of up to 5 % when approximating bony tissues by water. However, Fippel and Soukup [25] suggest that when all nuclear and electromagnetic processes are taken into account, the influence of this error results in a negligible effect on calculated dose distribution.

While modelling patient tissues as water in the context of nuclear interactions may have minimal effect on the calculated dose distribution, there has been increasing interest in calculation of prompt gamma emission activity and positron emission activity for the purpose of in vivo range verification for proton therapy, see for example [28]. Accurate calculation of these activity distributions requires estimation of the chemical composition of the patient in the imaging data set [17]. In light of this growing area of research interest, tissue modelling techniques for in vivo range verification calculations are presented in "Tissue decomposition techniques" section.

Quantitative 3D imaging for proton therapy treatment planning

Single-energy CT

X-ray computed tomography (CT) is the most common tool used for heterogeneity corrections in RT treatment planning. Single-energy CT (SECT) relies on the differential absorption of X-rays by tissues of different density and chemical composition. X-ray attenuation of the patient is measured at many projection angles and a 2D cross-section of the patient is generated by inverse radon transforms or iterative techniques. The images reconstructed from a CT scan reflect the X-ray energy spectrum weighted attenuation coefficients, μ, of tissues. Commonly, attenuation coefficients are transferred to Hounsfield units for presentation as defined in Eq. (6) [18].

$$\mathrm{HU} = 1000 \times \left(\frac{\mu}{\mu_w} - 1\right) \tag{6}$$

Here μ_w is the attenuation coefficient of water. The μ of tissue in the diagnostic X-ray spectrum is representative of the rate of photon intensity reduction due to photoelectric absorption, Compton (incoherent) scattering and coherent scattering. Equation (7) represents the relationship between total attenuation coefficient, atomic density and atomic cross-section of the individual interaction mechanisms [18].

$$\mu = \rho \frac{N_A}{A}\left(\sigma_{PE} + \sigma_{coh} + \sigma_{incoh}\right) \tag{7}$$

Here σ_{PE}, σ_{coh} and σ_{incoh} represent the atomic cross-section of photoelectric absorption, coherent scattering and incoherent scattering respectively and N_A is Avogadro's number.

Equation (7) applies only to pure elements. When determining the attenuation coefficient for composite materials, one must incorporate the fraction by weight w_j of each element in the material composition as in Eq. (8) [29].

$$\mu = \rho N_A \sum_j \frac{w_j}{A_j}\left(\sigma_{PE,j}\left(Z_j, A_j\right) + \sigma_{coh,j}\left(Z_j, A_j\right) + \sigma_{incoh,j}\left(Z_j, A_j\right)\right) \tag{8}$$

From Eq. (6), it can be understood that there is a linear relationship between the HU and μ of a tissue. However, as demonstrated in Eqs. (7) and (8), μ cannot uniquely define both ρ and the chemical composition of tissue. Schneider

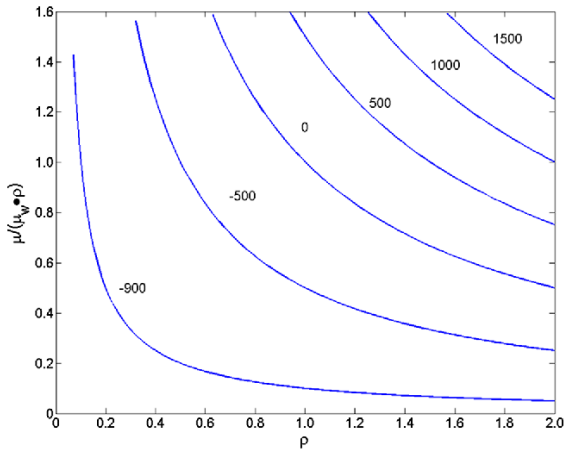

Fig. 1 Iso-HU *curves* showing constant HU for varying density. The *vertical axis* is determined by the chemical compositions and is independent of density. Adapted from [29]

et al. [29] illustrated this concept with a plot of iso-HU curves (Fig. 1). The iso-HU concept illustrates that although two materials may have the same HU, they may not have the same density and chemical composition. Therefore, the material definitions required for calculation of the proton interaction parameters described in "Proton interaction parameters" section cannot be uniquely provided by HUs.

Dual-energy CT

The use of dual-energy CT (DECT) as a tool for tissue characterization dates back to the formative days of X-ray CT [30]. The first description of calibration of CT data for radiotherapy treatment planning for heavy ion therapy by Chen et al. [8] even pointed to the theoretical advantages of DECT over SECT for this application. Due to the atomic number and energy dependence of X-ray interactions and the photoelectric effect in particular, the difference in attenuation between scans with two different X-ray spectra can be used to estimate chemical compositions of body tissues as described below.

Despite the proposal of DECT in the 1970s, it is only recently that specialised DECT scanners have become commercially available (Fig. 2).There are now several different methods for obtaining DECT data. These include, but are not limited to, the simultaneous use of rapid kV switching of a single X-ray tube, detector systems with different energy responses and two X-ray tubes at different potentials [31].

DECT was first proposed by Rutherford et al. [30] to identify the electron density and effective atomic number

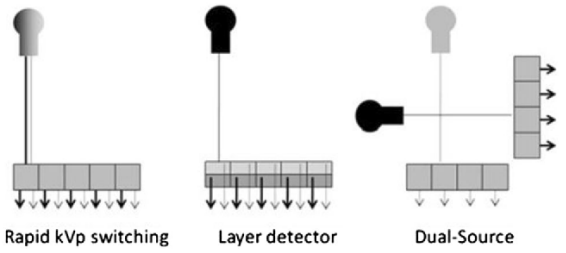

Fig. 2 Some of the different configurations proposed to achieve dual-energy CT. Reproduced from [31]

(Z_{eff}) of materials. By taking the ratio of attenuation coefficients at two different energy spectra, the density term in Eq. (7) is cancelled out and we are left only with differences in attenuation due to chemical composition. Rutherford et al. [30] used the expression in Eq. (9) to calculate the effective atomic number.

$$\frac{\mu(E_1)}{\mu(E_2)} = \frac{20.64E_1^{-3.28}Z_{eff}^{4.62} + \sigma_e(E_1)Z_{eff} + 2.8E_1^{-2.02}Z_{eff}^{2.86}}{20.64E_2^{-3.28}Z_{eff}^{4.62} + \sigma_e(E_2)Z_{eff} + 2.8E_2^{-2.02}Z_{eff}^{2.86}} \tag{9}$$

Here E_1 and E_2 are the representative energies of the two X-ray spectra and σ_e is the Klein-Nishina cross section at each representative energy.

Torikoshi et al. [32] adapted Rutherford's method for monoenergetic synchrotron radiation. Considering the limited availability of synchrotron radiation, Bazalova et al. [16] proposed the use of Eq. (10) in order to better represent the attenuation coefficient of the polyenergetic X-ray spectra used in DECT.

$$\mu_k = \rho_e \sum_{i-1}^{N} \omega_{k,i}\left[Z^4F(E_{k,i},Z) + G(E_{k,i},Z)\right] \tag{10}$$

Here F and G denote polynomial fits to the photoelectric and scattering terms of elemental electronic cross-sections and ω represents the weight of a given energy of index i within the X-ray spectrum. The index k represents the different X-ray spectra. For composite materials, Z can be replaced by the effective atomic number, Z_{eff}, which Bazalova et al. [16] represented by a power law relationship suggested by Johns and Cunningham [33].

Combining Eqs. (6) and (10), the relation between HU and Z_{eff} can be summarized by Eq. (11) [13].

$$\frac{HU_{x,k}}{1000} + 1 = \frac{\rho_{e,x}\sum_{i-1}^{N}\omega_{k,i}\left[Z_x^4F(E_{k,i},Z) + G(E_{k,i},Z)\right]}{\rho_{e,w}\sum_{i-1}^{N}\omega_{k,i}\left[Z_w^4F(E_{k,i},Z_w) + G(E_{k,i},Z_w)\right]} \tag{11}$$

Here the index x represents the x-th pixel and the subscript w signifies water.

Taking the ratio of *HU*s acquired with different X-ray spectra, the electron density dependence can be removed and an expression in terms of Z can be generated [13].

$$Z_x^4 = \frac{\mu'_{x,2} \times A_{w,2} \times SumG(Z,1) - \mu'_{x,1} \times A_{w,1} \times SumG(Z,2)}{\mu'_{x,1} \times A_{w,1} \times SumF(Z,2) - \mu'_{x,2} \times A_{w,2} \times SumF(Z,1)} \tag{12}$$

where

$$A_{w,k} = \sum_{i-1}^{N} \omega_{k,i} \left[Z_w^4 F\left(E_{k,i}, Z_w\right) + G\left(E_{k,i}, Z_w\right) \right] \tag{13}$$

$$SumF(Z,k) = \sum_{i-1}^{N} \omega_{k,i} F\left(E_{k,i}, Z\right) \tag{14}$$

$$SumG(Z,k) = \sum_{i-1}^{N} \omega_{k,i} G\left(E_{k,i}, Z\right) \tag{15}$$

Bazalova et al. [16]. obtained the solution to Eq. (12) by iterative means, giving the effective atomic number Z_{eff} for pixel x. The corresponding relative electron density of each pixel is defined in Eq. (16) and calculated from DECT with Eq. (17) [13].

$$\hat{\rho}_{e,x} \equiv \frac{\rho_{e,x}}{\rho_{e,w}} \tag{16}$$

$$\hat{\rho}_{e,x} = \frac{\mu'_{x,k} \times A_{water,k}}{SumF(Z,k) \times Z_x^4 + SumG(Z,k)} \tag{17}$$

From Eq. (10) it can be seen that knowledge of the X-ray spectrum is required for the above calculation. Measurement of clinical X-ray spectra can be problematic and the X-ray spectrum will vary depending on position in the patient. These difficulties led to the development of several methods for $\hat{\rho}_e$ and Z_{eff} from DECT data that do not require knowledge of the X-ray spectra. See for example [34, 35]. Regardless of the method, the end result is two images representing electron density and effective atomic number.

Proton CT

The most direct way to measure the interaction parameters of patients' tissues is to expose them to a beam of protons of large enough energy such that the Bragg peak occurs beyond the patient and measure the resulting beam energy and spatial distribution. This method has been proposed for stopping power measurements of patient tissues in a technique known as proton CT (pCT).

Computed tomography with heavy charged particles, and protons in particular, was first proposed as a possible alternative to X-ray CT by Allan Cormack in 1963 [36]. Even at this point, Cormack suggested that the values reconstructed with charged particle CT would be an important tool in the treatment planning process of heavy charged particle therapy, where the depth of the Bragg peak must be determined with a high degree of accuracy.

A tomographical reconstruction with alpha particles was first carried out by Goitein in 1972 [37]. It was not until 1976 that a prototype pCT system was constructed by Cormack and Koehler and tested at the Harvard Cyclotron Laboratory [38]. Further experimental systems were developed by Hanson et al. at Los Alamos laboratory [39–41]. The latter detector system consisted of a scintillator crystal mounted on a photomultiplier to measure the energy of protons after traversing the phantom. With this simple system, it was shown that density differences of 0.5 % could easily be distinguished. However, the authors also noted that reconstruction artefacts were present at boundaries between substances of differing density. It was suggested that this was the result of a differing degree of MCS in the two regions.

A description of a pCT system currently under development was published by Schulte et al. in 2004 [38]. The detector system has its origins in high-energy physics applications. The particle tracking component consists of two 2D sensitive silicon tracking modules upstream and downstream of the patient. This configuration allows for the measurement of individual proton positions and directions pre- and post-patient. In the initial prototypes, each 2D sensitive tracking module consisted of orthogonally oriented 1D sensitive single sided silicon strip detectors (SSD). The residual energy detector is a segmented scintillation crystal calorimeter, located downstream of the exiting tracking modules. Each crystal is individually wrapped and coupled with a silicon photodiode. A schematic of the head imaging system is illustrated in Fig. 3. The defining characteristic of this pCT system is the use of *individual* protons in the reconstruction procedure. That is, line integrals through the image space correspond to the paths of individual protons, which are estimated based on measurements made by the silicon tracking modules. For simple, fast reconstructions, straight line paths may be used. However, as has been shown by previous pCT studies, such an approach results in a decrease in spatial resolution [40–44]. The most accurate approach proposed to date is known as the most likely path (MLP) approach [45–47]. In this method, energy loss of protons is accounted for as they traverse the object, and material specific parameters are included in the MCS modelling. The result is a mathematical formalism that allows for the calculation of the lateral displacement and angular divergence of maximum likelihood at any given depth in the patient, based purely on the external measurements made by the silicon tracking modules.

Following the path estimation procedure, the integral SPR is calculated from the residual energy measurements.

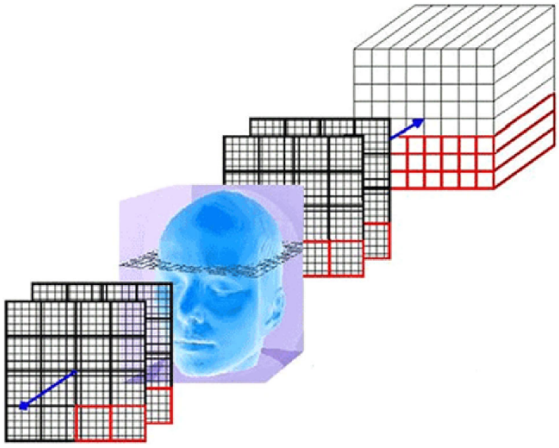

Fig. 3 Conceptual design of the proton computed tomography system. Two 2D sensitive proton tracking modules are positioned pre- and post-patient. A segmented crystal calorimeter records residual energy. The *red outline* indicates the components that comprise the first generation pCT system. The *blue line* represents a proton path terminating in the crystal calorimeter. Reproduced from [39]

In the energy range relevant to pCT (20–250 MeV), proton stopping power is well described by the Bethe-Bloch theory [48]. For protons in this energy range, the density effect and shell corrections are relatively small [49] and can therefore be neglected. In this case, the stopping power of a proton of energy E at spatial location $\mathbf{r}$ can be calculated by the Bethe-Bloch equation (Eq. 1). A number of works have suggested means for incorporating the nonlinear proton trajectories, which are not compatible with standard filtered backprojection, into image reconstruction algorithms (see for example Li et al. [50], Penfold et al. [51]., Rit et al. [52] and Poludniowski et al. [53]). Iterative techniques have been experimented with most widely. A review of iterative techniques in pCT reconstruction can be found in [54].

The calculation of integral SPR values requires one important approximation. The mean excitation potential, $I(\mathbf{r})$, of the inhomogeneous material is assumed to be constant and equal to that of some reference material. Since depth-dose curves for treatment planning are usually measured in water, I_{water} is the value used in pCT reconstructions. This approximation is justified by the logarithmic dependence of stopping power on I and the fact that I does not vary greatly from I_{water} for tissues encountered within the human body. It has been suggested in other work that this approximation will result in underestimation and overestimation of the stopping power values of adipose tissue and compact bone by at most 2 %, respectively [55].

In this manner, the pCT system described is capable of reconstructing proton SPR values and can be directly used by proton treatment planning software.

Tissue parameterization techniques

Single-energy CT

Chen et al. [8] were the first to discuss the use of CT data specifically for heavy ion therapy treatment planning. The parameter of interest for proton dose calculation in the formative days of proton therapy was WEPL. The WEPL of a heterogeneous tissue is defined as the thickness of water required to result in the same energy loss as the given tissue. Chen et al. [8] described the process by which the SECT HU of a given tissue pixel could be linked with the WEPL of that pixel. The authors proposed scanning of tissue substitute materials with a clinical CT scanner and then placing these materials in the therapeutic heavy ion beam to determine the water equivalent range. Use of multiple materials allowed for the generation of a calibration curve. The authors used solutions of water and potassium phosphate to simulate a variety of bone densities, alcohol and water mixtures to simulate adipose tissues and phantom lung and cork to simulate low density tissues. The authors observed a general agreement within 3 % between calculated and measured WEPLs when scanning and irradiating an anthropomorphic phantom, but did suggest a systematic error of approximately 1.5 % was present. The difference in carbon and oxygen content between water and the phantom materials was suggested as the likely source of this error.

The direct use of tissue substitute materials for calibrating HUs in terms of WEPLs was the primary heterogeneity correction used in proton therapy planning until the publication of the stoichiometric calibration technique of Schneider and Pedroni [12]. The stoichiometric technique attempts to correct for the differences in Z and Z/A between tissue substitute phantoms and real human tissues. As demonstrated in Fig. 1, HUs cannot distinguish between changes in mass density and chemical composition and therefore a tissue substitute material with the same HU as real human tissues may not have the same Z and Z/A.

The stoichiometric calibration curve is based on calculated data points pertaining to human tissue compositions estimated from publications such as ICRU 44 [27], ICRU 46 [56] and ICRP 23 [57]. For pure elements, the X-ray linear attenuation coefficient as calculated with Eq. (8) can be rewritten as [30].

$$\mu = \rho \frac{N_A}{A}\left[ZK^{KN}(E) + Z^n K^{SCA}(E) + Z^m K^{PE}(E)\right] \tag{18}$$

where K^{PE}, K^{SCA} and K^{KN} are X-ray spectra dependent variables corresponding to the relative contribution of photoelectric absorption, coherent scattering and incoherent scattering, respectively to total attenuation. The parameters m and n represent the exponent dependence of

photoelectric absorption and coherent scattering, respectively on atomic number. Jackson and Hawkes suggested values of 4.62 and 2.86 respectively for the range of atomic numbers encountered in human tissues and the X-ray energy spectra used in CT scanners [58].

Making use of electron density, ρ_e, Eq. (18) can be rewritten as Eq. (19) [12].

$$\mu = \rho_e \left[K^{KN}(E) + Z^{n-1} K^{SCA}(E) + Z^{m-1} K^{PE}(E) \right] \tag{19}$$

For composite materials, Eq. (20) may be used.

$$\mu = \rho N_g(Z, A) \left\{ K^{ph} \tilde{Z}^{3.62} + K^{coh} \tilde{Z}^{1.86} + K^{KN} \right\} \tag{20}$$

where

$$\tilde{Z} = \left[\lambda_i Z_i^{3.62} \right]^{1/3.62} \tag{21}$$

$$\tilde{Z} = \left[\lambda_i Z_i^{1.86} \right]^{1/1.86} \tag{22}$$

$$N_g = \sum_i N_A \frac{\omega_i Z_i}{A_i} \tag{23}$$

$$\lambda_i = N_g^i / N_g \tag{24}$$

N_g is the number of electrons per unit mass of the mixture.

The values of K^{PE}, K^{SCA} and K^{KN} should be obtained for each clinical CT scanner. This can be done by scanning a tissue substitute phantom with various inserts of known composition, measuring the mean HU for each insert and performing a fit of Eq. (10) to the measured data points. Theoretical HUs can thus be obtained for the reference human tissues of interest. Similarly, SPR must be calculated from the density and chemical composition of the reference human tissues and that of water via Eq. (1). A plot of SPR vs HU for the reference human tissues removes systematic uncertainties associated with a calibration approach based on tissue substitute materials. An example of a stoichiometric HU-SPR calibration curve is shown in Fig. 4 [4]. Here the tissues derived from Jani [59] and ICRU 49 [60] were chosen to calculate the values of HU and SPR. A piecewise linear fit to the data points is used as the final calibration function.

Although the stoichiometric calibration technique has been shown to improve patient stopping power estimations relative to the tissue substitute approach, it is still not a patient specific calibration technique. Schneider et al. [9] proposed the use of proton radiography in conjunction with X-ray CT stoichiometric calibration to obtain patient specific calibration functions. Here, the residual range of a proton beam measured with a proton radiograph was compared to the predicted residual range from a digitally reconstructed radiograph calculated via the stoichiometric calibration of HU. The stoichiometric calibration function was then optimized to minimize the difference between measured and calculated residual range. The authors found that range errors of 3.6 mm could be reduced to 0.4 mm with the optimized calibration curve. A more recent study [61] further explored this technique with the use of only a single detector distal to the patient and a more efficient optimization engine. The single detector was seen as a cost-efficient solution to allow for wider clinical implementation, but had the drawbacks of reduced spatial resolution due to a lack of individual proton tracking which was

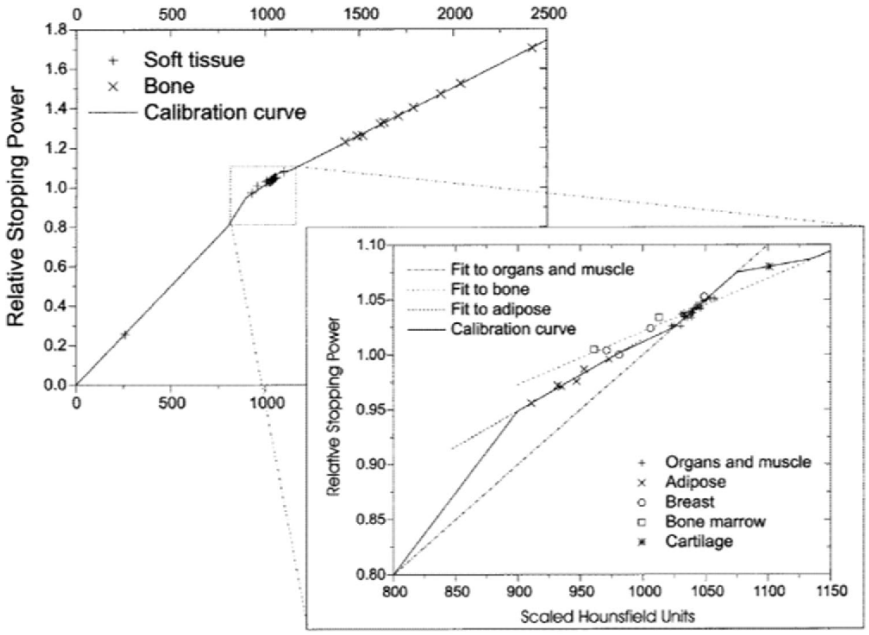

Fig. 4 An example of a stoichiometric HU-SPR curve. Reproduced from [4]

implemented in the previous study. Despite the technical challenges, this continues to be an area of interest and development in proton SPR calibration.

These CT calibration methods summarized thus far were proposed only for calibration of relative stopping power (or equivalently WEPL). As described in "Proton interaction parameters" section, other interaction mechanisms in proton therapy can influence dose distributions. An alternative CT parameterization approach was proposed by Fippel and Soukup [25] originally for application in a voxelized Monte Carlo (MC) algorithm for proton therapy (VMCpro). Here, the authors parameterize both SPR and $\hat{T}$ in terms of mass density. In a similar approach to Schneider and Pedroni [45] reference tissue datasets are used to generate calibration functions to link mass density of human tissues with these proton interaction parameters. A calibration of HUs to mass density is required, as is common practice in X-ray TPSs. Although the authors do not recommend a particular calibration procedure for this, a stoichiometric calibration as described by Schneider et al. [12] should be used for accurate calculations in human tissues.

The VMCpro CT calibration approach does not account for non-water materials when considering nuclear interactions. As the authors point out, this will result in a negligible error in dose calculation. Recently, however, there has been growing interest in the field of in vivo range verification for proton therapy which requires accurate estimation of nuclear interaction induced nuclear emissions. In this application, non-water substances must be modelled and to date this has been approached with the tissue decomposition techniques outlined in "Tissue decomposition techniques" section.

Dual-energy CT

DECT is well suited to proton therapy dose calculations because relative electron density is reconstructed directly and this is the dominant material parameter in the calculation of stopping power as can be seen in Eq. (1). This fact was noted at the time of Chen's publication [8]. The other material dependent parameter I_m, representing the mean excitation energy, is known to have a dependence on atomic number of the absorbing material. Yang et al. [13] proposed the calibration of ln I_m in terms of Z_{eff} for proton therapy dose calculation. Because of the dependence of Z_{eff} on X-ray energy, this calibration should follow a similar stoichiometric method to that of Schneider et al. [12] originally proposed for SECT. The relationship derived by Yang et al. [13] is illustrated in Fig. 5.

Compared with the SECT stoichiometric calibration method introduced by Schneider et al. [12], the DECT approach showed a greater accuracy in the determination of SPR when variation in tissue density and composition was introduced. Due to the direct determination of $\hat{\rho}_e$, which is the dominant tissue parameter in proton SPR, tissue SPRs derived from DECT showed less than 1 % RMS error compared with 3.24 % for SECT.

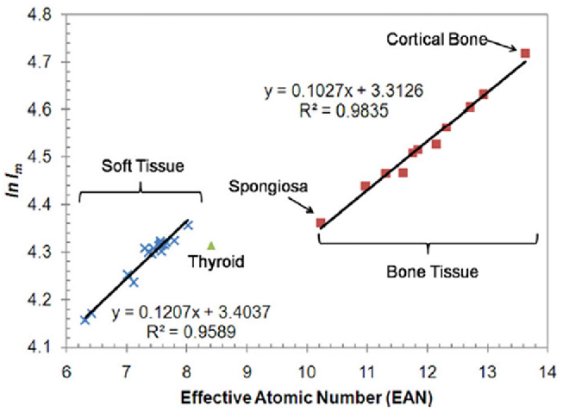

Fig. 5 The relationship between Z_{eff} and lnI_m. *Two lines* represent the trends of soft tissues and bone tissues respectively. Reproduced from [13]

Another recent study by Bourque et al. [62] applied Schneider's stoichiometric calibration concept to DECT scans. The authors scanned a calibration phantom with a Siemens SOMATOM Definition Flash dual source CT scanner to show that the DECT stoichiometric formalism resulted in mean absolute errors of (0.3 ± 0.4) and (1.6 ± 2.0) % for $\hat{\rho}_e$ and Z_{eff} respectively. This translated to mean absolute errors in I_m and proton stopping powers of (4.1 ± 0.4) and (0.5 ± 0.4) % respectively. In this case the relationship between Z_{eff} and I_m was characterised by a piecewise polynomial.

Tissue decomposition techniques

The concept of decomposing a pixel into constituent chemical elements and density was originally investigated for the purpose of MC dose calculation. Because radiation transport with MC is based on determining the interaction cross-section at each interaction site, weights of each elemental constituent are required. Modern TPSs are now also applying material decomposition techniques to analytical dose calculation algorithms.

As mentioned in the previous section, tissue decomposition is currently of interest in proton therapy treatment planning due to the potential application of in vivo range verification. *In vivo* range verification utilises the increased nuclear interaction cross-sections close to the end of the

proton range. A by-product of nuclear interaction can be excitation of the nucleus which then promptly decays with the emission of a gamma ray, or by transmuting the nucleus to an unstable isotope. If the isotope decays via positron emission, the two 511 keV photons emitted upon annihilation of the positron with an atomic electron can be detected with a conventional PET system. To be able to use this measured information, an accurate MC derived prediction of activity distribution is required, which requires knowledge of the chemical elements in each tissue. For further information on in vivo range verification techniques in hadron therapy, the reader is referred to [28].

Single-energy CT

The most commonly used method for defining tissue parameters from HUs is to define a representative set of tissues, each with fixed chemical composition but variable density. An early example of such an approach was provided in 1998 by DeMarco et al. [14] when demonstrating the applicability of the MC toolkit MCNP4 to CT-based dose calculations in radiotherapy treatment planning. DeMarco et al. generated a table to divide the region of HUs of a CT scan into five tissue types (lung, fat, water, muscle or bone) with chemical compositions as defined by ICRP 23 [57] and ICRU44 [27]. Within each tissue type the HUs were further subdivided into regions of varying density for a total of 17 materials defined in the MC simulation.

While De Marco et al. clearly demonstrated improved accuracy of CT-based MC dose calculation over the conventional correction-based algorithms commonly in use at the time, it was less obvious how the division of the HU scale should be performed and the importance of this division on dose calculation accuracy. Another publication in the late 1990's by du Plessis et al. [15] attempted to provide guidance as to the number of materials required when dividing the HU scale into discrete materials. The authors performed MC simulations with the 16 most common tissue types found in the human body according to ICRU 44 [27]. For lung and bone, the tissue was further subdivided into materials of different density. By performing MC depth dose calculations with an 8 MV photon beam in homogeneous materials, du Plessis et al. classified materials as dosimetrically equivalent if the depth dose values were within 1 %. The authors concluded that a total of 57 tissue types should be defined. These comprised 21 types of cortical bone, 31 types of lung tissue and 5 types of soft tissue. It was suggested that intervals of 30 HU are sufficient for lung and soft tissues and 100 HU is sufficient for bone tissues when dividing a tissue into materials of different density.

While this was an important study in providing guidance in establishing a material definition scheme for accurate CT-based MC dose calculations, the authors correctly commented that the applicability of the findings to other types of radiation beams or indeed other photon beam energies was not clear. In 2000 Schneider et al. [29] proposed a material definition approach that would be independent of the type and energy of the therapeutic beam. The authors proposed that all tissues within a given HU region could be described by an interpolation of the chemical compositions and densities of two bounding tissues. For example, skeletal tissues are composed of bone marrow and osseous tissue of different proportions. Therefore, HUs could be used to interpolate the weight of chemical elements and physical density between bone marrow and osseous bone for all skeletal tissues. For soft tissues, the authors defined two regions bounded by adipose and adrenal glands, and small intestine and connective tissue respectively. The authors suggested that the HU scale be divided into 24 material types with further subdivisions based on density. This was significantly different to the seven material types proposed by du Plessis et al., but was intended to be a more general calibration approach. While the approach of Schneider et al. [29] may have wider applicability, the drawback was that interpolated tissues, in the soft tissue region in particular, were not real body tissues, but rather a mix of organ compositions.

A study by Jiang et al. [11] examined the effect of CT based tissue decomposition schemes on MC dose calculation accuracy in proton therapy. Three approaches of varying complexity were studied. The first assumed only water of varying density, the second consisted of a basic tissue decomposition table with four tissue types and the third was that of Schneider et al. [29] as described above. The authors compared DVH parameters using the different tissue decomposition schemes for head and neck treatment sites. Jiang et al. demonstrated that slight discrepancies in assignment of mass density in the target region did not play a significant role in dose calculation accuracy, while assignment of chemical composition could play a significant role in dose calculation accuracy. Outside of the target region, within the beam path, both mass density and chemical composition assignment could affect dose calculation accuracy in the target and the surrounding organ at risk. The authors did not compare to a reference dose calculation in a phantom of known composition and thus could only comment on differences between calculated dose with each scheme, rather than accuracy of the calculated dose.

Dual-energy CT

Bazalova et al. [16] suggested that tissue decomposition could be performed more accurately with the use of DECT. As described previously, one is able to reconstruct $\hat{\rho}_e$ and

Z_{eff} with DECT. Relative electron density is directly related to mass density, and effective atomic number is independent of mass density. This decoupling of density and chemical composition in the CT data allows for a more accurate assignment of a representative tissue to each voxel of the CT image [32].

Bazalova et al. performed a comparison of MC dose calculation accuracy with tissues defined by DECT and SECT for therapeutic high energy photon and electron beams [16]. The results indicated the improvements in dose calculation possible with the DECT. For an 18 MeV electron beam, dose calculation errors up to 6 % were found for SECT but they were below 1 % in the DECT approach. With the 18 MV photon beam, dose calculation errors ranged up to 3 % using SECT but were below 1 % with DECT [16].

A proton therapy specific DECT tissue decomposition study was performed by Landry et al. [17]. These authors investigated the accuracy in determining the oxygen and carbon content in human tissue using SECT and DECT with the end goal being the application to positron emission tomography for range verification. They investigated relationships between Z_{eff} as calculated by DECT and the oxygen and carbon content. In a calculation study, they compared DECT and SECT derived values for carbon and oxygen content with reference values for 73 tissue types. RMS errors and maximum errors in carbon and oxygen content were calculated to demonstrate the accuracy of each approach. In the absence of noise and systematic errors in stoichiometric calibration, the DECT approach resulted in a more accurate determination of carbon and oxygen content. The results also showed, however, that an increase in noise or systematic error in stoichiometric calibration degraded the advantages of DECT. This is a potential problem in DECT where noise can be significant in the Z_{eff} reconstructed image.

Hünemohr et al. [34] adapted the SECT decomposition method of Schneider et al. [29] for application to DECT data. This study differed from the original SECT approach which was based only on HU, by utilising $\hat{\rho}_e$ and Z_{eff} to better characterize the relative weights of individual elements. The authors established a parametric fit for the weight of chemical components and mass density as a function of Z_{eff} and $\hat{\rho}_e$ (Eqs. (25), (26)) [34].

$$\omega_i = a_i \cdot \hat{\rho}_e + b_i \cdot Z_{eff} + c_i \cdot \hat{\rho}_e Z_{eff} + d_i \quad (25)$$

$$\rho = a \cdot \hat{\rho}_e + b \quad (26)$$

These authors used the same reference tissues as Schneider et al. [29] to establish a relationship between chemical weights and $\hat{\rho}_e$ and Z_{eff} of human tissues. Applying this method to proton therapy dose calculation, Hünemohr et al. examined the differences in mean excitation energy, relative electron density and stopping power ratio obtained by the SECT and DECT approaches. They concluded the maximum difference in I_m can be improved from 5.8 to 1.3 % when DECT replaces SECT. The maximum SPR deviation of tissue was reduced from 3.1 to 0.7 %.

Commercial treatment planning system techniques

While many of the formative proton therapy centres make use of in-house designed TPSs, several commercial options have become available. This section provides a description of the CT calibration methods for proton planning in four of the available or soon to be available commercial TPSs: XiO (Elekta AB, Stockholm, Sweden), Varian Eclipse (Varian Medical System, Palo Alto, CA, USA), Philips Pinnacle (Philips Radiation Oncology Systems, Fitchburg, WI) and RaySearch Raystation (RaySearch Laboratories AB, Stockholm, Sweden) TPSs.

The Elekta XiO, Varian Eclipse and Philips Pinnacle[3] TPSs are all based on the tissue parameterization method [61] described in "Single-energy CT" section. The TPSs require the creation of a HU-SPR calibration function for proton therapy planning. While no requirements are placed on the method used to create this function, the stoichiometric calibration method suggested by Schneider et al. [12] is generally accepted as the most accurate technique. Pinnacle[3] also requires an additional HU-density function to be defined. For proton planning, the density calibration is used in the relative scattering power and nuclear interaction functions, as described by Fippel and Soukup [25], while the SPR calibration is used to define proton range and energy deposition.

The Raystation approach more closely resembles the tissue decomposition methods described in "Single-energy CT" section. Raystation requires only a user defined HU-density calibration function. The density of each CT voxel is matched to a look-up table of approximately 50 reference tissue types containing elemental weights, density and mean excitation energy. The chemical composition and mean excitation energy of the tissue closest in density to the voxel density is assigned to that voxel and from this all proton interaction parameters can be calculated.

Conclusion

Successful delivery of dose in proton therapy is far more sensitive to tissue heterogeneities than in X-ray therapy. One of the primary challenges in accounting for tissue heterogeneity is calibrating the 3D imaging data for the interaction parameters of interest. While SECT has a long

history in radiotherapy treatment planning, the ability to reconstruct electron density and effective atomic number in DECT is receiving growing interest in proton therapy. Studies have demonstrated the potential advantages of DECT to proton treatment planning with both analytical and MC calculation techniques, however, a commercial DECT-based treatment planning system is yet to be developed. Proton CT systems also continue to be investigated with many seeing this as the ultimate in reducing range uncertainty in proton therapy treatment planning.

Acknowledgments The authors would like to acknowledge J. Pollard for her constructive comments in reviewing this article.

References

1. Papanikolaou N, Battista JJ, Boyer AL, Kappas C, Klein E, Mackie TR, Sharpe M, Van Dyk J (2004) Tissue inhomogeneity corrections for megavoltage photon beams. AAPM Task Gr 65:1–142
2. Robinson DM (2008) Inhomogeneity correction and the analytic anisotropic algorithm (AAA). J Appl Clin Med Phys 9(2):1–12
3. Verhaegen F, Devic S (2005) Sensitivity study for CT image use in Monte Carlo treatment planning. Phys Med Biol 50(5):937
4. Schaffner B, Pedroni E (1998) The precision of proton range calculations in proton radiotherapy treatment planning: experimental verification of the relation between CT-HU and proton stopping power. Phys Med Biol 43(6):1579
5. Paganetti H (2012) Range uncertainties in proton therapy and the role of Monte Carlo simulations. Phys Med Biol 57(11):R99
6. Newhauser WD, Zhang R (2015) The physics of proton therapy. Phys Med Biol 60(8):R155
7. Tavernier S (2010) Experimental techniques in nuclear and particle physics. Springer Science & Business Media, Heidelberg
8. Chen GT, Singh RP, Castro JR, Lyman JT, Quivey JM (1979) Treatment planning for heavy ion radiotherapy. Int J Radiat Oncol Biol Phys 5(10):1809–1819
9. Schneider U, Pemler P, Besserer J, Pedroni E, Lomax A, Kaser-Hotz B (2005) Patient specific optimization of the relation between CT-Hounsfield units and proton stopping power with proton radiography. Med Phys 32(1):195–199
10. Kanematsu N, Inaniwa T, Koba Y (2012) Relationship between electron density and effective densities of body tissues for stopping, scattering, and nuclear interactions of proton and ion beams. Med Phys 39(2):1016–1020
11. Jiang H, Seco J, Paganetti H (2007) Effects of Hounsfield number conversion on CT based proton Monte Carlo dose calculations. Med Phys 34(4):1439–1449
12. Schneider U, Pedroni E, Lomax A (1996) The calibration of CT Hounsfield units for radiotherapy treatment planning. Phys Med Biol 41(1):111
13. Yang M, Virshup G, Clayton J, Zhu X, Mohan R, Dong L (2010) Theoretical variance analysis of single-and dual-energy computed tomography methods for calculating proton stopping power ratios of biological tissues. Phys Med Biol 55(5):1343
14. DeMarco J, Solberg T, Smathers JB (1998) A CT-based Monte Carlo simulation tool for dosimetry planning and analysis. Med Phys 25(1):1–11
15. Du Plessis F, Willemse C, Lötter M, Goedhals L (1998) The indirect use of CT numbers to establish material properties needed for Monte Carlo calculation of dose distributions in patients. Med Phys 25(7):1195–1201
16. Bazalova M, Carrier J-F, Beaulieu L, Verhaegen F (2008) Dual-energy CT-based material extraction for tissue segmentation in Monte Carlo dose calculations. Phys Med Biol 53(9):2439
17. Landry G, Parodi K, Wildberger JE, Verhaegen F (2013) Deriving concentrations of oxygen and carbon in human tissues using single-and dual-energy CT for ion therapy applications. Phys Med Biol 58(15):5029
18. Johns HE, Cunningham JR (1974) The physics of radiology. Charles C Thomas, Springfield, p 457
19. Gottschalk B, Koehler A, Schneider R, Sisterson J, Wagner M (1993) Multiple Coulomb scattering of 160 MeV protons. Nucl Instrum Methods Phys Res Sect B 74(4):467–490
20. Fermi E (1940) The ionization loss of energy in gases and in condensed materials. Phys Rev 57(6):485
21. Eyges L (1948) Multiple scattering with energy loss. Phys Rev 74(10):1534
22. Kanematsu N (2009) Semi-empirical formulation of multiple scattering for the Gaussian beam model of heavy charged particles stopping in tissue-like matter. Phys Med Biol 54(5):N67
23. Gottschalk B (2010) On the scattering power of radiotherapy protons. Med Phys 37(1):352–367. doi:10.1118/13264177
24. Ibbott GS (1985) Radiation dosimetry: electron beams with energies between 1 and 50 MeV (ICRU report No. 35). Med Phys 12(6):813–813
25. Fippel M, Soukup M (2004) A Monte Carlo dose calculation algorithm for proton therapy. Med Phys 31(8):2263–2273
26. ICRU (2000) Nuclear data for neutron and proton radiotherapy and for radiation protection dose. International commission on radiation units and measurements report 63
27. ICRU (1989) Tissue substitutes in radiation dosimetry and measurement. International commission on radiation units and measurements report 44
28. Knopf A-C, Lomax A (2013) In vivo proton range verification: a review. Phys Med Biol 58(15):R131
29. Schneider W, Bortfeld T, Schlegel W (2000) Correlation between CT numbers and tissue parameters needed for Monte Carlo simulations of clinical dose distributions. Phys Med Biol 45(2):459
30. Rutherford R, Pullan B, Isherwood I (1976) Measurement of effective atomic number and electron density using an EMI scanner. Neuroradiology 11(1):15–21
31. Fornaro J, Leschka S, Hibbeln D, Butler A, Anderson N, Pache G, Scheffel H, Wildermuth S, Alkadhi H, Stolzmann P (2011) Dual-and multi-energy CT: approach to functional imaging. Insights Imaging 2(2):149–159
32. Torikoshi M, Tsunoo T, Sasaki M, Endo M, Noda Y, Ohno Y, Kohno T, Hyodo K, Uesugi K, Yagi N (2003) Electron density measurement with dual-energy X-ray CT using synchrotron radiation. Phys Med Biol 48(5):673
33. Johns H, Cunningham J (1983) The physics of radiology, 4th edn. Thomas, Springfield
34. Hünemohr N, Paganetti H, Greilich S, Jäkel O, Seco J (2014) Tissue decomposition from dual energy CT data for MC based dose calculation in particle therapy. Med Phys 41(6):061714
35. Landry G, Seco J, Gaudreault M, Verhaegen F (2013) Deriving effective atomic numbers from DECT based on a parameterization of the ratio of high and low linear attenuation coefficients. Phys Med Biol 58(19):6851
36. Cormack AM (1963) Representation of a function by its line integrals, with some radiological applications. J Appl Phys 34(9):2722–2727
37. Goitein M (1972) Three-dimensional density reconstruction from a series of two-dimensional projections. Nucl Instrum Methods 101(3):509–518
38. Schulte R, Bashkirov V, Li T, Liang Z, Mueller K, Heimann J, Johnson LR, Keeney B, Sadrozinski HF, Seiden A (2004)

Conceptual design of a proton computed tomography system for applications in proton radiation therapy. Nucl Sci IEEE Trans 51(3):866–872
39. NICADD (2015) http://www.niu.edu/nicadd/research/medical/
40. Cormack A, Koehler A (1976) Quantitative proton tomography: preliminary experiments. Phys Med Biol 21(4):560
41. Hanson KM (1979) Proton computed tomography. Nucl Sci IEEE Trans 26(1):1635–1640
42. Hanson K, Bradbury J, Cannon T, Hutson R, Laubacher D, Macek R, Paciotti M, Taylor C (1981) Computed tomography using proton energy loss. Phys Med Biol 26(6):965
43. Hanson K, Bradbury J, Koeppe R, Macek R, Machen D, Morgado R, Paciotti M, Sandford S, Steward V (1982) Proton computed tomography of human specimens. Phys Med Biol 27(1):25
44. Zygmanski P, Gall KP, Rabin MS, Rosenthal SJ (2000) The measurement of proton stopping power using proton-cone-beam computed tomography. Phys Med Biol 45(2):511
45. Schneider U, Pedroni E (1994) Multiple Coulomb scattering and spatial resolution in proton radiography. Med Phys 21(11):1657–1663
46. Williams D (2004) The most likely path of an energetic charged particle through a uniform medium. Phys Med Biol 49(13):2899
47. Schulte R, Penfold S, Tafas J, Schubert K (2008) A maximum likelihood proton path formalism for application in proton computed tomography. Med Phys 35(11):4849–4856
48. Bethe H (1930) Zur theorie des durchgangs schneller korpuskularstrahlen durch materie. Ann Phys 397(3):325–400
49. Leo W (1988) Techniques for nuclear and particle physics experiments. Nucl Instrum Methods Phys Res 834:290
50. Li T, Liang Z, Singanallur JV, Satogata TJ, Williams DC, Schulte RW (2006) Reconstruction for proton computed tomography by tracing proton trajectories: a Monte Carlo study. Med Phys 33(3):699–706
51. Penfold S, Schulte RW, Censor Y, Rosenfeld AB (2010) Total variation superiorization schemes in proton computed tomography image reconstruction. Med Phys 37(11):5887–5895
52. Rit S, Dedes G, Freud N, Sarrut D, Létang JM (2013) Filtered backprojection proton CT reconstruction along most likely paths. Med Phys 40(3):031103
53. Poludniowski G, Allinson N, Evans P (2014) Proton computed tomography reconstruction using a backprojection-then-filtering approach. Phys Med Biol 59(24):7905
54. Penfold S, Censor Y (2015) Techniques in iterative proton CT image reconstruction. Sens Imaging 16(1):1–21
55. Schulte RW, Bashkirov V, Klock MCL, Li T, Wroe AJ, Evseev I, Williams DC, Satogata T (2005) Density resolution of proton computed tomography. Med Phys 32(4):1035–1046
56. ICRU (1992) Photon, electron, proton, and neutron interaction data for body tissues. International commission on radiation units and measurements report 46
57. ICRP (1975) Reference man: anatomical, physiological and metabolic characteristics. ICRP Publication 23
58. Jackson DF, Hawkes D (1981) X-ray attenuation coefficients of elements and mixtures. Phys Rep 70(3):169–233
59. Janni JF (1982) Proton range-energy tables, 1 keV–10 GeV, energy loss, range, path length, time-of-flight, straggling, multiple scattering, and nuclear interaction probability. Part I. For 63 compounds. At Data Nucl Data Tables 27:147
60. Berger M, Inokuti M, Andersen H, Bichsel H (1993) Stopping powers and ranges for protons and alpha particles. ICRU report 49
61. Doolan P, Testa M, Sharp G, Bentefour E, Royle G, Lu H (2015) Patient-specific stopping power calibration for proton therapy planning based on single-detector proton radiography. Phy Med Biol 60(5):1901
62. Bourque AE, Carrier J-F, Bouchard H (2014) A stoichiometric calibration method for dual energy computed tomography. Phys Med Biol 59(8):2059

Chapter 3

Dosimetric comparison of stopping power calibration with DECT and SECT in proton therapy treatment planning

The following forms the basis of this chapter.

Zhu, Jiahua, and Scott N. Penfold. "Dosimetric comparison of stopping power calibration with dual-energy CT and single-energy CT in proton therapy treatment planning." Medical Physics 43.6 (2016): 2845-2854.

3.1 Introduction and motivation

The accuracy of proton dose calculation is dependent on the accuracy of the stopping power ratio (SPR) of human tissues traditionally obtained by single energy CT (SECT). CT numbers, however, cannot uniquely quantify both atomic number and density of tissue. Thus dual

energy CT (DECT) was proposed as a means to obtain the tissue characteristics necessary for accurate dose calculation in proton therapy.

In this chapter, a novel approach for DECT-based dose calculation in proton therapy treatment planning is demonstrated. The effective atomic number and electron density of materials are obtained through DECT imaging of a plastic phantom and used for dose calculation in a commercial proton treatment planning system. Compared with the traditional SECT approach, the new method improves the accuracy of dose calculation in the PTV and OAR regions.

3.2 Statement of Contribution

3.2.1 Conception

The idea to compare the differences of SPR with DECT and SECT was first conceptualised by Scott Penfold. The method to analyse the dose difference in proton TPS was conceptualised by all authors.

3.2.2 Realisation

The theory was developed by Jiahua Zhu. The model was then checked by Scott Penfold. Matlab code and proton planning were performed by Jiahua Zhu.

3.2.3 Documentation

This paper was primarily written by Jiahua Zhu. Editing was performed by all authors.

Statement of Authorship

Title of Paper	Dosimetric comparison of stopping power calibration with dual-energy CT and single-energy CT in proton therapy treatment planning
Publication Status	☑ Published ☐ Accepted for Publication ☐ Submitted for Publication ☐ Unpublished and Unsubmitted work written in manuscript style
Publication Details	Zhu, Jiahua, and Scott N. Penfold. "Dosimetric comparison of stopping power calibration with dual-energy CT and single-energy CT in proton therapy treatment planning." Medical Physics 43.6 (2016): 2845-2854.

Principal Author

Name of Principal Author (Candidate)	Jiahua Zhu
Contribution to the Paper	Developed the whole MATLAB code for the SPR calculation by DECT. Designed the SECT, DECT and theoretical proton treatment plans for the dose calculation comparison. Wrote and edited the manuscript.
Overall percentage (%)	80%
Certification:	This paper reports on original research I conducted during the period of my Higher Degree by Research candidature and is not subject to any obligations or contractual agreements with a third party that would constrain its inclusion in this thesis. I am the primary author of this paper.
Signature	Date 30/10/16

Co-Author Contributions

By signing the Statement of Authorship, each author certifies that:

i. the candidate's stated contribution to the publication is accurate (as detailed above);

ii. permission is granted for the candidate in include the publication in the thesis; and

iii. the sum of all co-author contributions is equal to 100% less the candidate's stated contribution.

Name of Co-Author	Scott Penfold
Contribution to the Paper	Supervised development of work, helped in data analysis and manuscript evaluation.
Signature	Date 31/10/16

Name of Co-Author	
Contribution to the Paper	
Signature	Date

Please cut and paste additional co-author panels here as required.

Medical Physics
The International Journal of Medical Physics Research and Practice

Dosimetric comparison of stopping power calibration with dual-energy CT and single-energy CT in proton therapy treatment planning

Jiahua Zhu and Scott N. Penfold

Citation: Medical Physics **43**, 2845 (2016); doi: 10.1118/1.4948683
View online: http://dx.doi.org/10.1118/1.4948683
View Table of Contents: http://scitation.aip.org/content/aapm/journal/medphys/43/6?ver=pdfcov
Published by the American Association of Physicists in Medicine

Dosimetric comparison of stopping power calibration with dual-energy CT and single-energy CT in proton therapy treatment planning

Jiahua Zhu
Department of Physics, University of Adelaide, Adelaide, SA 5005, Australia

Scott N. Penfold[a)]
Department of Physics, University of Adelaide, Adelaide, SA 5005, Australia and Department of Medical Physics, Royal Adelaide Hospital, Adelaide, SA 5000, Australia

(Received 21 December 2015; revised 11 April 2016; accepted for publication 23 April 2016; published 13 May 2016)

Purpose: The accuracy of proton dose calculation is dependent on the ability to correctly characterize patient tissues with medical imaging. The most common method is to correlate computed tomography (CT) numbers obtained via single-energy CT (SECT) with proton stopping power ratio (SPR). CT numbers, however, cannot discriminate between a change in mass density and change in chemical composition of patient tissues. This limitation can have consequences on SPR calibration accuracy. Dual-energy CT (DECT) is receiving increasing interest as an alternative imaging modality for proton therapy treatment planning due to its ability to discriminate between changes in patient density and chemical composition. In the current work we use a phantom of known composition to demonstrate the dosimetric advantages of proton therapy treatment planning with DECT over SECT.
Methods: A phantom of known composition was scanned with a clinical SECT radiotherapy CT-simulator. The phantom was rescanned at a lower X-ray tube potential to generate a complimentary DECT image set. A set of reference materials similar in composition to the phantom was used to perform a stoichiometric calibration of SECT CT number to proton SPRs. The same set of reference materials was used to perform a DECT stoichiometric calibration based on effective atomic number. The known composition of the phantom was used to assess the accuracy of SPR calibration with SECT and DECT. Intensity modulated proton therapy (IMPT) treatment plans were generated with the SECT and DECT image sets to assess the dosimetric effect of the imaging modality. Isodose difference maps and root mean square (RMS) error calculations were used to assess dose calculation accuracy.
Results: SPR calculation accuracy was found to be superior, on average, with DECT relative to SECT. Maximum errors of 12.8% and 2.2% were found for SECT and DECT, respectively. Qualitative examination of dose difference maps clearly showed the dosimetric advantages of DECT imaging, compared to SECT imaging for IMPT dose calculation for the case investigated. Quantitatively, the maximum dose calculation error in the SECT plan was 7.8%, compared to a value of 1.4% in the DECT plan. When considering the high dose target region, the root mean square (RMS) error in dose calculation was 2.1% and 0.4% for SECT and DECT, respectively.
Conclusions: DECT-based proton treatment planning in a commercial treatment planning system was successfully demonstrated for the first time. DECT is an attractive imaging modality for proton therapy treatment planning owing to its ability to characterize density and chemical composition of patient tissues. SECT and DECT scans of a phantom of known composition have been used to demonstrate the dosimetric advantages obtainable in proton therapy treatment planning with DECT over the current approach based on SECT. [http://dx.doi.org/10.1118/1.4948683]

Key words: dual-energy CT, effective atomic number, stopping power ratio, proton therapy

1. INTRODUCTION

Tissue heterogeneity correction has been shown to be a crucial aspect in accurate proton therapy treatment planning and delivery for both passive scattered and spot scanned proton beams.[1,2] Commonly, tissue heterogeneity is accounted for by translating computed tomography (CT) numbers to proton stopping power ratios (SPRs). The stoichiometric calibration procedure of Schneider *et al.*[3] is the recommended method for obtaining the Hounsfield unit (HU)–SPR curve. This approach attempts to account for the difference in chemical composition between tissue substitute materials used during CT number-SPR calibration and real patient tissues. However, this method still relies on the real patient tissues corresponding to the chemical composition of the tissue database used during the stoichiometric calibration (often ICRU44 or ICRU46 tissues[4,5]). Differences in age, sex, diet, or health state can result in variability of the chemical composition of tissues.[6–9]

Errors in SPR calculation can therefore be expected when the patient tissue chemical composition does not match that of the calibration tissue set.[10]

Schneider *et al.*[11] have demonstrated that a single CT number cannot differentiate between a change in density or chemical composition of an imaged material. Dual-energy CT (DECT), however, is able to attribute changes in X-ray attenuation to either density or chemical composition. This is achieved by decomposing two simultaneous single-energy CT (SECT) scans into relative electron density ($\hat{\rho}_e$) and effective atomic number (Z_{eff}). The process exploits the energy dependency of kilovoltage X-ray interaction atomic cross sections and the energy independent parameter $\hat{\rho}_e$.

There have been a number of recent investigations into the calculation of proton SPR from DECT data.[10,12–16] Formative work by Yang *et al.*[10] demonstrated that Z_{eff} obtained with DECT can be correlated with the mean excitation energy (I) of human tissues. The mean excitation energy and $\hat{\rho}_e$ are the only tissue dependent parameters required for calculation of SPR. Utilizing this concept, Yang *et al.*[10] carried out theoretical calculations to demonstrate that proton SPRs obtained with the DECT stoichiometric calibration are more robust to situations in which the chemical composition of the patient tissue is different to that of the calibration tissue set. However, it has also been shown that DECT tissue characterization techniques are sensitive to noise in real CT data,[16] which may mean the conclusions of Yang *et al.* do not apply in practical applications. Hansen *et al.*[14] compared the accuracy of SPRs derived from SECT, DECT, and a Monte Carlo simulated proton CT system. Hudobivnik *et al.*[15] also assessed the accuracy of SPR calculation with SECT and DECT and compared the range of therapeutic proton beams calculated in Monte Carlo with SECT and DECT derived SPR maps.

The previous works outlined above have demonstrated the potential gains in SPR accuracy achievable with dedicated DECT scanners. In the current work the robustness of real DECT image data acquired with a conventional CT-simulator in predicting the proton SPR of materials that are not exactly matched to the stoichiometric calibration data set is examined. Expanding on the previous works, the dosimetric effect of this situation is examined when using SECT or DECT image data for intensity modulated proton therapy (IMPT) treatment planning with a commercial proton treatment planning system (TPS).

2. METHODS AND MATERIALS

2.A. Stoichiometric calibration of proton SPR

The SPR of materials can be calculated with the Bethe equation[17]

$$\text{SPR} = \hat{\rho}_e \ln\left[\frac{2m_e c^2\beta^2}{I_m(1-\beta^2)} - \beta^2\right] \Big/ \ln\left[\frac{2m_e c^2\beta^2}{I_{\text{water}}(1-\beta^2)} - \beta^2\right]. \quad (1)$$

Here m_e is the rest electron mass, $\hat{\rho}_e$ is the electron density of the material relative to that of water, c is the speed of light in vacuum, β is the speed of the proton relative to the speed of light, and I_m and I_{water} are the mean excitation energies of the material and water, respectively. Here, I_{water} was set to 75 eV as recommended by ICRU49.[18] ICRU49 report an uncertainty of ±3 eV in this quantity. The value used in the current work is not likely to have a significant effect in a comparison of SECT or DECT based on proton therapy planning, as long as a consistent value is used throughout. The mean excitation energy of a composite material can be calculated from the mean excitation energy of the component elements and the Bragg additivity rule.

2.A.1. SECT stoichiometric calibration

The stoichiometric CT number calibration method was first proposed by Schneider *et al.*[3] A brief summary will be given here, but for a more detailed derivation, the reader is referred to Ref. 3. The X-ray linear attenuation coefficient μ of a material can be expressed with

$$\mu = \rho\frac{N_A}{A}\left[ZK^{\text{KN}}(E) + Z^n K^{\text{SCA}}(E) + Z^m K^{\text{PE}}(E)\right]. \quad (2)$$

Here ρ denotes mass density, N_A is Avogadro's number, A is the atomic weight, Z is the atomic number, and K^{PE}, K^{SCA}, and K^{KN} are constants which characterize the relative importance of the photoelectric effect, coherent scattering, and incoherent scattering, respectively, of the CT X-ray energy spectrum.[19] Rutherford *et al.*[19] assigned values of 4.62 and 2.86 to m and n, respectively, for the energies encountered in kV X-ray imaging and the elements present in human tissues.

When dealing with CT numbers, the ratio of the attenuation coefficient of the material to the attenuation coefficient of water at the same energy must be considered. Therefore, for a single X-ray spectrum, Eq. (2) becomes

$$\frac{\mu}{\mu_w} = \frac{\rho\frac{N_A}{A}ZK^{\text{KN}}(E)\left[1 + Z^{1.86}k_1(E) + Z^{3.62}k_2(E)\right]}{\rho_w\frac{N_A}{A_w}Z_wK^{\text{KN}}(E)\left[1 + Z_w{}^{1.86}k_1(E) + Z_w{}^{3.62}k_2(E)\right]}, \quad (3)$$

where

$$k_1 = \frac{K^{\text{SCA}}}{K^{\text{KN}}}, \quad (4)$$

$$k_2 = \frac{K^{\text{PE}}}{K^{\text{KN}}}. \quad (5)$$

In Eq. (3), ρ_w, Z_w, and A_w represent the density, effective atomic number, and effective atomic weight of water, respectively. Defining relative electron density $\hat{\rho}_e$ and the Hounsfield unit (HU) as the unit of CT numbers for a single element as

$$\hat{\rho}_e = \frac{\rho\frac{N_A}{A}Z}{\rho_w\frac{N_A}{A_w}Z_w} \quad (6)$$

and

$$\text{HU} = 1000\times\left(\frac{\mu}{\mu_w} - 1\right). \quad (7)$$

Equation (3) can be written as

$$\frac{\text{HU}}{1000} + 1 = \hat{\rho}_e\frac{\left[1 + Z^{1.86}k_1(E) + Z^{3.62}k_2(E)\right]}{\left[1 + Z_w{}^{1.86}k_1(E) + Z_w{}^{3.62}k_2(E)\right]}. \quad (8)$$

TABLE I. Chemical compositions and densities of Catphan inserts.

Insert	Chemical composition	Density (g/cm^3)
PMP	$C_6H_{12}(CH_2)$	0.83
LDPE	C_2H_4	0.92
Polystyrene	C_8H_8	1.00
Acrylic	$C_5H_8O_2$	1.18
Delrin	$(OCH_2)_n$	1.42
Teflon	CF_2	2.16

When dealing with composite materials, Schneider *et al.*[3] suggest that the attenuation coefficient can be expressed as

$$\mu = \rho_e K^{\mathrm{KN}}\left[1 + k_1\hat{Z}^{1.86} + k_2\tilde{Z}^{3.62}\right], \tag{9}$$

where

$$\rho_e = \rho N_A \sum_i \frac{\omega_i Z_i}{A_i}, \tag{10}$$

$$\tilde{Z} = \left[\sum_i \lambda_i Z_i^{3.62}\right]^{1/3.62}, \tag{11}$$

$$\hat{Z} = \left[\sum_i \lambda_i Z_i^{1.86}\right]^{1/1.86}, \tag{12}$$

$$\lambda_i = \frac{\omega_i Z_i}{A_i}\Big/\sum_i \frac{\omega_i Z_i}{A_i}. \tag{13}$$

Here, ω_i is the fractional weight of element i in the composite material. Applying Eqs. (11)–(13) also to water, Eq. (8) finally becomes

$$\frac{\mathrm{HU}}{1000} + 1 = \hat{\rho}_e \frac{\left[1 + \hat{Z}^{1.86}k_1(E) + \tilde{Z}^{3.62}k_2(E)\right]}{\left[1 + \hat{Z}_w^{1.86}k_1(E) + \tilde{Z}_w^{3.62}k_2(E)\right]}. \tag{14}$$

A CT scan of a tissue equivalent phantom can be used to obtain k_1 and k_2 for the given CT spectrum. Using the known chemical composition of the tissue equivalent inserts of the phantom, Eqs. (6) and (10)–(13) can be used to calculate all tissue dependent parameters in Eq. (14). By obtaining the mean CT number of each insert from the CT scan, a nonlinear least squares regression algorithm can be used to obtain the unknown parameters k_1 and k_2 from Eq. (14). In the current work, the 140 kVp tube potential of a Philips Brilliance Big Bore CT-simulator was used to scan the CIRS Model 062M (CIRS, Inc., Norfolk, VA, USA) phantom for this calculation. The CIRS phantom contained nine different types of material inserts.

The purpose of the stoichiometric calibration is to generate a CT number to SPR calibration curve for materials expected during proton treatment planning. Using the known chemical composition and density of a representative set of materials, a theoretical relationship between CT number and proton SPR can be obtained with Eqs. (14) and (1), respectively.

2.A.2. DECT stoichiometric calibration

In the current work, the process for DECT stoichiometric calibration is based on the work of Landry *et al.*,[20] followed by a calibration of mean excitation energy in terms of Z_{eff} as suggested by Yang *et al.*[10] The stoichiometric calibration follows a similar principle to SECT, however, instead of scanning the object with a single X-ray spectrum, scans with two different spectra are acquired. In the current study, 90 and 140 kVp tube potentials were used for sequential DECT scanning of the CIRS phantom. The two additional 90 kVp spectral parameters denoted by $k_{1,90}$, $k_{2,90}$ were obtained in the same manner as outlined above for the 140 kVp tube potential.

TABLE II. Common plastics used for the HU–SPR and Z_{eff}–ln I_m curves.

Plastic	Chemical composition	Density (g/cm^3)
Furan	C_4H_4O	0.94
Acrylonitrile butadiene styrene	$C_{15}H_{17}N$	1.07
Polyamide	$C_6H_{11}NO$	1.13
Polycarbonate	$C_{15}H_{16}O_2$	1.20
Phenol formaldehyde resin	$C_7H_6O_2$	1.21
Polysulfone	$C_{27}H_{22}SO_4$	1.24
Polyetherimide	$C_{37}H_{24}O_6N_2$	1.27
Polylactic acid	$C_3H_4O_2$	1.30
PEEK	$C_{19}H_{18}O_3$	1.32
Polyethylene terephthalate	$C_{10}H_8O_4$	1.38
Polyester	$C_6H_4(COOH)_2$	1.38
Silicone	$Si(CH_3)_2O$	1.42
Ethylene chlorotrifluoroethylene	$C_4H_4F_3Cl$	1.68

The Philips Brilliance Big Bore CT-simulator (90, 120, and 140 kVp available tube potentials) was used for both SECT and DECT scanning. Bourque *et al.*[12] investigated the influence of X-ray tube combinations on Z_{eff} and $\hat{\rho}_e$ accuracy in DECT. They found that 100 kVp in conjunction with 140 kVp with additional Sn filtration gave better results when compared to 80 kVp–140/Sn kVp and 80–140 kVp. The closest available beam combinations were used in the current work. Due to noise and beam hardening in the lower kVp spectra, in particular, this may result in larger errors in Z_{eff} and $\hat{\rho}_e$ than one would obtain with a dedicated DECT scanner.

To obtain the Z_{eff} of an unknown scanned object, the ratio of the CT numbers obtained with the different X-ray spectra is used to cancel the energy independent $\hat{\rho}_e$. Therefore, Eq. (14) is expanded to

$$\frac{\mathrm{HU}_{90} + 1000}{\mathrm{HU}_{140} + 1000} = \frac{1 + \hat{Z}^{1.86}k_{1,90} + \tilde{Z}^{3.62}k_{2,90}}{1 + \hat{Z}_w^{1.86}k_{1,90} + \tilde{Z}_w^{3.62}k_{2,90}} \times \frac{1 + \hat{Z}_w^{1.86}k_{1,140} + \tilde{Z}_w^{3.62}k_{2,140}}{1 + \hat{Z}^{1.86}k_{1,140} + \tilde{Z}^{3.62}k_{2,140}}. \tag{15}$$

At this point, we assume that $\hat{Z}$ and $\tilde{Z}$ are equivalent to Z_{eff}. The accuracy of this assumption is not critical for the calculation of Z_{eff} as this quantity is not used directly in the calculation of SPR but rather is used to obtain ln I_m via a calibration function.

TABLE III. Spectral parameters k_1 and k_2 of the 90 and 140 kVp X-ray beams of the CT scanner.

CT spectrum (kVp)	k_1	k_2
90	2.85×10^{-5}	1.10×10^{-3}
140	1.49×10^{-5}	6.58×10^{-4}

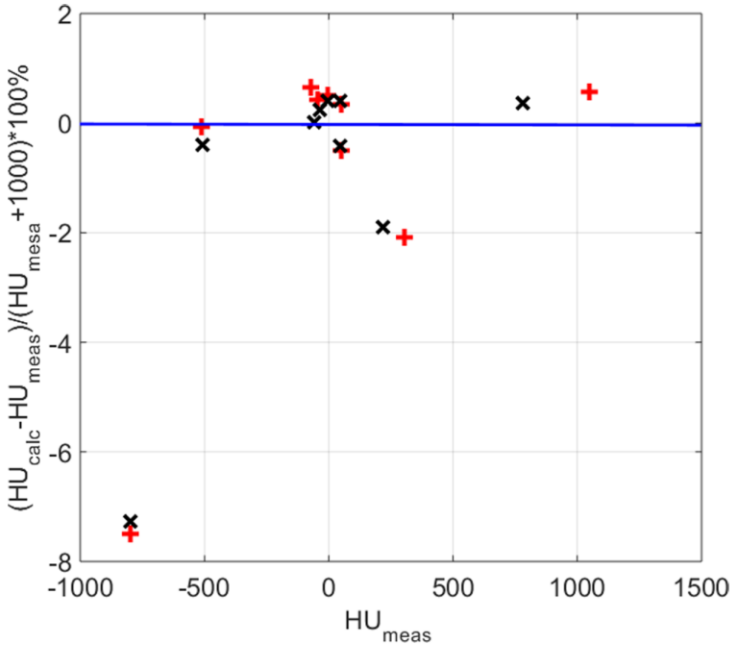

FIG. 1. Residual errors between measured and calculated CT numbers for the inserts of the CIRS phantom when using the spectral parameters shown in Table III. Red crosses correspond to the 90 kVp scan and black crosses to the 140 kVp scan. (See color online version.)

It is important, however, that the derived Z_{eff} can return the correct value of $\hat{\rho}_e$ when substituted into Eq. (14) as $\hat{\rho}_e$ is used explicitly in the SPR calculation for DECT proton planning. The accuracy of the $\hat{\rho}_e$ calculation is presented in Table V.

Having obtained the energy spectra parameters k, the Z_{eff} of an unknown material can be obtained from the ratio of the two CT numbers. The Matlab (The Mathworks, Inc.) *fzero* function was used to find the roots of Eq. (15). This differs from the approach of Landry *et al.*[20] who used a calibration function to translate from the ratio of high and low attenuation coefficients to Z_{eff}. The approach proposed in the current work does not rely on an additional curve-fitting step to generate the calibration function. Bazalova *et al.*[21] also used a MATLAB routine to iteratively determine Z_{eff} from the roots of a power equation. However, in that work an additional curve fitting step was required to characterize the relationship between X-ray interaction cross section and atomic number. Therefore, the method proposed in the current work requires fewer curve fitting approximations than those presented previously.

Substituting Z_{eff} into Eq. (16) for both $\hat{Z}$ and $\tilde{Z}$, $\hat{\rho}_e$ can then be calculated from one of the CT image sets. The image obtained with the spectrum of larger mean energy contains less noise and has been used for the $\hat{\rho}_e$ calculation in the current work. This method of $\hat{\rho}_e$ calculation is consistent with that of Bazalova *et al.*[21]

$$\hat{\rho}_e = \left(\frac{\text{HU}}{1000}+1\right)\Bigg/\frac{\left[1+\hat{Z}^{1.86}k_1(E)+\tilde{Z}^{3.62}k_2(E)\right]}{\left[1+\hat{Z}_w^{1.86}k_1(E)+\tilde{Z}_w^{3.62}k_2(E)\right]}. \tag{16}$$

TABLE IV. Calculated parameters for the representative plastics listed in Table I.

Material	Calculated HU at 140 kVp	Calculated Z_{eff}	Calculated I_m (eV)	Calculated SPR at 219 MeV
Furan	−121	6.3	69.7	0.90
Acrylonitrile butadiene styrene	18	5.7	63.5	1.06
Polyamide	96	6.1	62.8	1.14
Polycarbonate	135	6.1	66.6	1.17
Phenol formaldehyde resin	127	6.4	71.9	1.15
Polysulfone	185	8.1	74.3	1.17
Polyetherimide	171	6.3	72.3	1.19
Polylactic acid	224	6.8	73.1	1.24
PEEK	239	6.2	68.4	1.27
Polyethylene terephthalate	279	6.6	74.3	1.30
Polyester	275	6.8	76.1	1.28
Silicone	483	10.6	86.9	1.36
Ethylene Chlorotrifluoroethylene	689	11.7	100.8	1.46

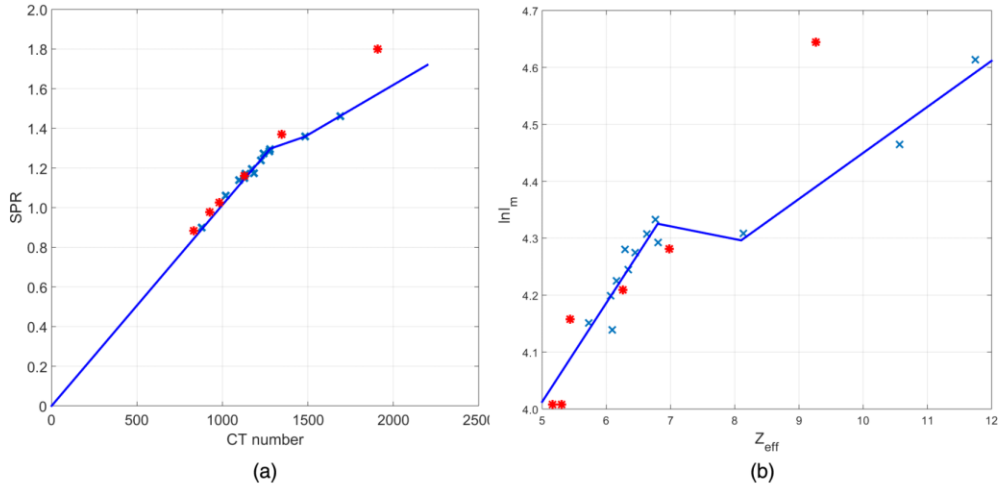

FIG. 2. (a) SECT HU–SPR and (b) DECT Z_{eff}–ln I_m stoichiometric calibration curves derived from common plastic materials. Blue crosses correspond to the calibration plastics and red stars correspond to the Catphan inserts. In both SECT and DECT, significant deviations from the calibration curve are seen with Teflon. (See color online version.)

Having obtained the quantity describing the chemical composition (Z_{eff}) from the DECT data, the correlation with the chemical dependent component of Eq. (1) is derived. The mean excitation energy of composite materials can be calculated with the Bragg additivity rule

$$\ln I_m = \frac{\sum \frac{\omega_i z_i}{A_i} \times \ln I_i}{\sum \frac{\omega_i z_i}{A_i}}. \tag{17}$$

In an analogous manner to SECT where a theoretical CT number–SPR calibration curve is generated for a representative material set, a theoretical Z_{eff}–ln I_m calibration curve can be generated for the same set. The advantage of the DECT approach is that differences in CT number can be attributed to changes in either chemical composition or density, or both.

2.A.3. Representative material set

Sequential CT scans at 90 and 140 kVp of the CIRS Model 062M electron density tissue substitute phantom was used to determine the CT spectral parameters. To test the accuracy of SECT and DECT in determining proton SPR, a phantom of known chemical composition and density is required. In the current study the phantom used was the Catphan Module 404 (The Phantom Laboratory, Salem, NY, USA). The vendor quoted density and chemical composition of the Catphan inserts are listed in Table I.

In clinical stoichiometric calibrations, tissue reference sets such as ICRU44 or ICRU46 (Refs. 4 and 5) are used to estimate human patient tissues. A phantom of known composition was required in the current work to allow for computation of reference SPRs. Therefore, instead of using ICRU44 or ICRU46 materials to simulate real human tissues, a set of common plastics was used to simulate the materials present in the Catphan. These materials possess a similar Z and Z/A ratio to the materials of the Catphan, which is not the case for ICRU materials. The representative plastics, listed in Table II, are used to generate the theoretical HU–SPR and Z_{eff}–ln I_m calibration curves for SECT and DECT, respectively.

2.B. Reference SPR calculation

The known chemical composition and density of the Catphan inserts (Table I) was used to calculate the expected proton SPR value directly from Eqs. (1) and (6), and (17). The proton SPR's of the different plastic inserts obtained with SECT and DECT stoichiometric calibrations were compared to these reference values.

TABLE V. Material parameters for the Catphan obtained from DECT and calculated parameters determined from vendor quoted compositions.

	Z_{eff}			$\hat{\rho}_e$			I_m		
Material	Calc.	Meas.	% diff.	Calc.	Meas.	% diff.	Calc.	Meas.	% diff.
Teflon	8.4	9.3 ± 0.4	10.7	1.87	1.81 ± 0.02	−3.21	104.0	80.4 ± 1.0	−22.7
PMP	5.4	5.2 ± 1.4	−3.7	0.85	0.85 ± 0.02	0.00	55.1	57.1 ± 2.4	3.6
Delrin	6.9	7.0 ± 0.9	1.4	1.36	1.36 ± 0.02	0.00	72.3	71.5 ± 1.8	−1.1
LDPE	5.4	5.3 ± 1.4	−1.9	0.95	0.97 ± 0.01	2.11	55.1	58.7 ± 2.3	6.5
Polystyrene	5.7	5.4 ± 1.5	−4.1	1.00	1.01 ± 0.02	1.00	63.9	59.5 ± 3.2	−6.9
Acrylic	6.5	6.3 ± 1.2	−3.1	1.15	1.14 ± 0.02	−0.87	67.3	66.5 ± 3.0	−1.2

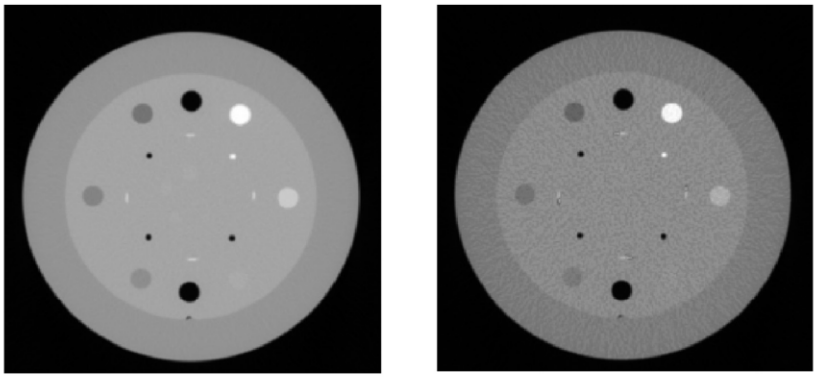

(a) (b)

FIG. 3. SPR images calculated by (a) SECT and (b) DECT.

2.C. IMPT dose calculation in a reference phantom

Previous investigations into the utilization of DECT for proton treatment planning have been limited to an assessment of the accuracy of SPR calculation.[10,14,22,23] In the current study a comparison of dose calculation accuracy with SECT and DECT data sets has been performed with the IMPT dose calculation engine of the research release of Philips PINNACLE[3] proton treatment planning system (TPS).

2.C.1. Reference IMPT dose calculation

A CT scan of the Catphan was acquired at 140 kVp. Reference calibration curves of HU–SPR and HU–ρ were directly constructed from measured HUs, calculated SPRs, and vendor quoted densities. SPRs were calculated from the chemical compositions and densities (see Table II) and Eqs. (1), (6), and (17).

A hollow cylinder centered on the Catphan axis was created as the target volume for an IMPT plan. The inner diameter was 3.8 cm and outer diameter was 10 cm. Four spot scanned proton beams were equally distributed over 360°. A grid spot pattern of 0.6 cm lateral spacing and 80% layer overlap of dose was created to cover the target volume. The target volume was prescribed 2 Gy. The PINNACLE[3] proton pencil beam scanning (PBS) dose calculation algorithm was used. This is an analytical algorithm that includes an approximation of nuclear attenuation effects and energy dependent multiple Coulomb scattering.

TABLE VI. SPRs of Catphan materials calculated by vendor quoted composition with associated uncertainty and measured with DECT and SECT. The mean values and standard deviation for a region of interest in each of the DECT and SECT data sets are reported.

Material	Calculated SPR	SPR_{DECT}	% diff.	SPR_{SECT}	% diff.
Teflon	1.80 ± 0.09[a]	1.81 ± 0.02	0.6	1.57 ± 0.02	−12.8
PMP	0.88 ± 0.06	0.89 ± 0.02	1.1	0.86 ± 0.01	−2.3
Delrin	1.37 ± 0.08	1.34 ± 0.02	−2.2	1.32 ± 0.00	−3.7
LDPE	0.98 ± 0.06	0.98 ± 0.02	0.0	0.95 ± 0.01	−3.1
Polystyrene	1.02 ± 0.05	1.04 ± 0.03	2.0	1.01 ± 0.01	−1.9
Acrylic	1.16 ± 0.07	1.17 ± 0.03	0.9	1.15 ± 0.01	−0.9

[a]As Teflon does not contain hydrogen, uncertainty is related only to density variation.

2.C.2. SECT based IMPT dose calculation

An analogous proton dose calculation was implemented with the SECT stoichiometric calibrated image set. The 140 kVp Catphan CT image was used once again. A stoichiometric HU–SPR calibration table was used in this case. The ROIs, pencil beam patterns, and MUs obtained from the reference plan were imported into the SECT image set to calculate the dose without re-optimization.

2.C.3. DECT based IMPT dose calculation

Current commercial proton TPS require SECT HU for dose calculation. This is not consistent with the output of DECT. To input the DECT data into the TPS, the two DECT HU images were first processed in Matlab to obtain the Z_{eff} and $\hat{\rho}_e$ images as detailed above. The single SPR image was then calculated from the $\hat{\rho}_e$ image, the stoichiometric calibration of Z_{eff} in terms of the mean excitation energy, and Eq. (1). The SPR image was saved as a CT DICOM dataset and imported to the TPS. A HU–SPR calibration curve was used for the DECT SPR calibration in PINNACLE.[3] The ROIs, pencil beam patterns, and MUs obtained from the reference plan were imported into the DECT image set and dose recalculated without re-optimization.

2.D. IMPT dose calculation in an anthropomorphic phantom

While the Catphan is useful to compare SECT and DECT based dose distributions with that calculated with reference SPRs, the cylindrical nature and regular spacing of inserts may not provide a realistic estimate of dosimetry in real human geometries. To perform an assessment of dose differences between SECT and DECT based proton treatment planning in human geometries, SECT and DECT scans of the cranial

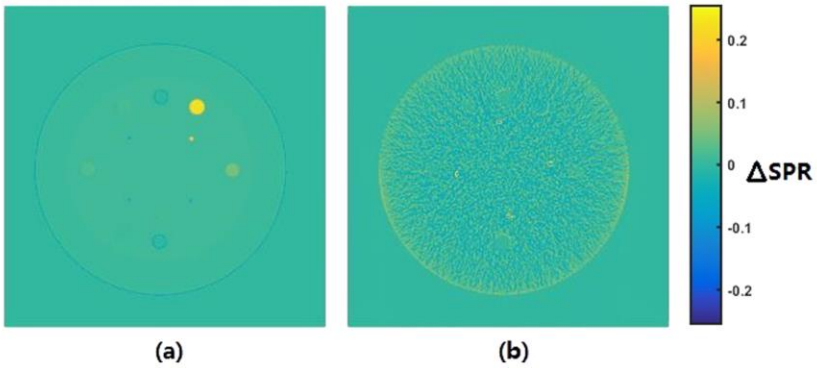

FIG. 4. SPR difference maps for (a) SECT and (b) DECT.

region of the Rando (Radiological Support Devices, Inc., CA, USA) phantom were acquired. The Rando phantom contains a human skeleton in a tough plastic based on a synthetic isocyanate rubber. Due to the real human skeleton, a reference dose distribution cannot be calculated, but dose differences can be assessed.

A treatment plan simulating a base of skull chordoma was created in PINNACLE. A brainstem and abutting PTV were contoured. Representative materials were required to generate the HU–SPR and Z_{eff}–ln I_m calibration curves for SECT and DECT based planning. The calibration plastics used in the Catphan study (Table II) were not applicable for the Rando phantom due to differences in the Z/A between the plastics and materials in Rando. Given the tissue equivalent nature of the plastic and the real human skeleton, calibration curves based on ICRU 44 tissues were created.

IMPT dose distributions were optimized based on the SECT image set. Pencil beam patterns and weights were then copied to the DECT image set and dose recomputed without reoptimization. Dose difference maps were generated to compare the difference in dose calculated based on SECT and DECT image sets.

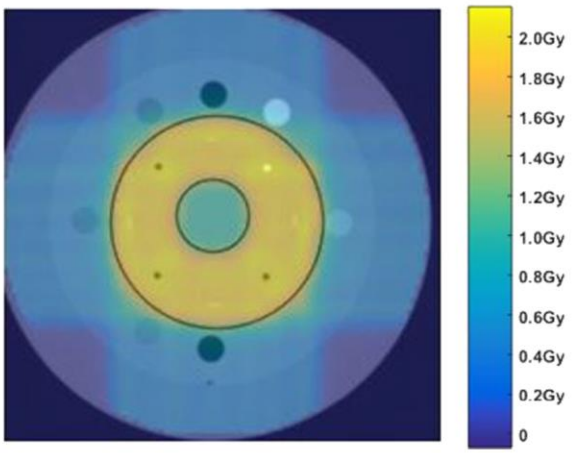

FIG. 5. Reference dose distribution calculated with the HU–SPR calibration table based on vendor quoted compositions.

3. RESULTS

3.A. CT spectra parameterization

The CT energy spectrum parameters, k_1 and k_2, for the 90 and 140 kVp beams of a Philips Brilliance Big Bore CT-simulator were obtained by scanning the CIRS electron density phantom (Model 062M). The values were obtained by a nonlinear least squares regression of Eq. (14) using the vendor quoted composition and density of the CIRS phantom. The values are displayed in Table III. To validate the parameters obtained from the regression, residuals of calculated and measured CT numbers for the inserts of the CIRS phantom are shown in Fig. 1. Largest relative errors are seen with the material simulating lung (inhale). This is not unexpected due to the division by a smaller CT number resulting in a larger relative error.

3.B. Catphan proton SPR calculation accuracy

Utilizing the parameters displayed in Table III, the HU, Z_{eff}, and $\hat{\rho}_e$ of the representative set of plastic materials could be calculated. The known composition of the plastics could also be used to calculate the mean excitation energy [Eq. (17)] and proton SPR [Eq. (1)]. The calculated parameters for these plastics are summarized in Table IV. The stoichiometric calibration curves for both SECT and DECT are shown in Fig. 2. For SECT and DECT, a piecewise linear fit of HU to SPR and Z_{eff}–ln I_m was performed, respectively. The calculated Z_{eff}, $\hat{\rho}_e$, and ln I_m of the Catphan inserts obtained from DECT scans are shown in Table V. The SECT and DECT proton SPR maps obtained from the stoichiometric calibration curves are shown in Fig. 3.

The calculated SPRs of the Catphan inserts obtained from the vendor quoted composition and density were compared to those obtained from the calibration curves of Fig. 2. With and without Teflon, root mean square errors in SPR of 5.7% and 2.3% were found for SECT, respectively. These are compared to values of 1.4% and 1.5% for DECT, respectively.

For both images shown in Fig. 3, a region of interest was created in each of the Catphan inserts. The mean pixel value and standard deviation were recorded. A comparison of the calculated reference values to those obtained via SECT and

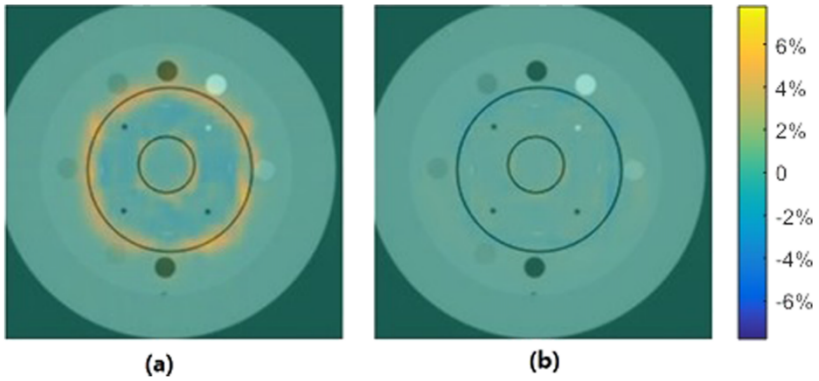

FIG. 6. Relative error between dose calculated with the reference and (a) SECT and (b) DECT calibrated image sets. The overlaid concentric circles illustrate the target region defined in the treatment planning system. The percentage differences are relative to the 2 Gy prescription dose.

DECT is shown in Table VI. Uncertainties in the reference SPR values for the Catphan inserts were calculated by varying the vendor quoted hydrogen content and density. By measuring the volume and mass of plugs in a tissue substitute phantom, Ainsley and Yeager[24] found variations of less than 1% from the vendor quoted density values. A conservative 0.5% variation in density was assumed in the current work. While vendors do not provide uncertainties in the chemical composition of their inserts, calculations with hydrogen content varying by 1% have been used to estimate the uncertainty in reference SPR. Due to the Z/A ratio being approximately 1 for hydrogen and close to 1/2 for all other elements, variations in hydrogen content have the largest effect on electron density and thus SPR.

The noise of the SPR images in Fig. 3 is represented by the standard deviation for each region of interest listed in Table VI. The mean standard deviation of all inserts derived from the DECT approach was 0.023, compared to 0.010 with SECT. This increased noise is visible in the two images shown in Fig. 3.

Using the reference HU–SPR calibration curve generated from the known composition of the Catphan, a reference SPR map could be obtained from the 140 kV CT scan. SPR difference maps created by subtracting the SECT and DECT SPR values from the reference values are shown in Fig. 4.

3.C. IMPT dose calculation in a reference phantom

IMPT dose distributions generated for the reference, stoichiometric SECT and DECT calibrated image sets were created. The dose distribution calculated with the reference HU–SPR calibration table is shown in Fig. 5. To facilitate the comparison of the doses, relative differences of the SECT and DECT calculated doses with respect to the reference dose distribution are shown in Fig. 6.

From Fig. 6, it is clear that there are greater dose calculation errors with the SECT image set than the DECT image set. Quantitatively, the maximum dose calculation error with the SECT image set is up to 7.8%, compared to a DECT value of 1.4%. When considering the high dose target region, the root mean square (RMS) errors in dose are 2.1% and 0.4% for SECT and DECT, respectively.

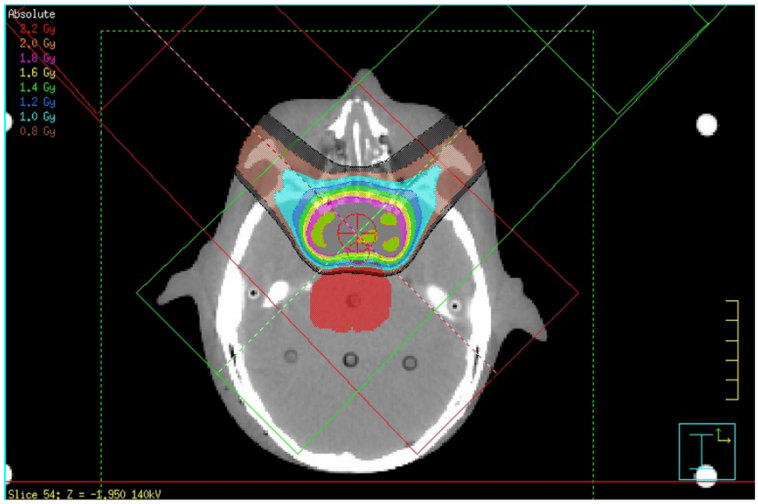

FIG. 7. Simulated base of skull chordoma IMPT treatment plan. Dose for a single fraction of 2.0 Gy prescription is shown.

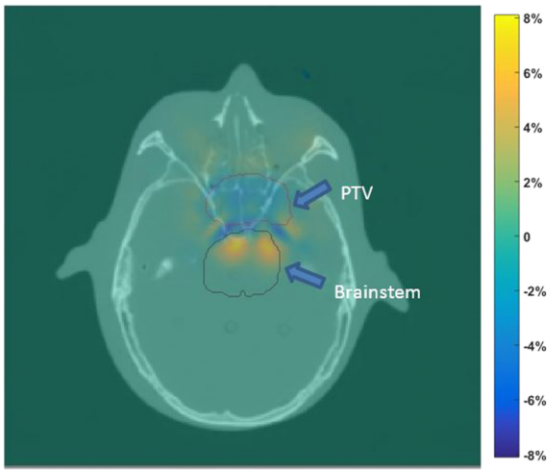

FIG. 8. Relative dose difference between doses calculated with the SECT and DECT image sets. Relative differences calculated as dose resulting from SECT, subtracted from that resulting from DECT, and normalized by a global prescription value of 2 Gy.

3.D. IMPT dose calculation in an anthropomorphic phantom

A single axial slice of the SECT simulated Rando base of skull chordoma proton treatment plan is shown in Fig. 7. Treatment beams were selected at ±45° to the patient anterior direction to match the C- shaped geometry of the PTV surrounding the brainstem. Dose differences between dose calculated on the SECT image set and DECT image set for this slice are shown in Fig. 8. While a comparison with a reference dose distribution was not possible in this case due to the unknown composition of the real human skeleton, it is evident that relative dose differences are similar in magnitude with those calculated on the reference Catphan. Given the improved accuracy of DECT based dose calculation demonstrated with the Catphan, it is reasonable to assume that the DECT based dose distribution is also more accurate in this realistic geometry. This suggests that range errors associated with SECT SPR calibration can lead to dose calculation errors of up to 8% at the distal end of the proton beam. If the target region is abutting a critical structure, this may have significant normal tissue complication effects.

4. DISCUSSION

Successful proton therapy delivery requires an accurate conversion of the parameters obtained via kV X-ray imaging to the parameters required for calculation of proton dose deposition. If the composition of the patient differs from that of the material set used in the calibration of HUs to proton SPRs, errors in dose calculation may result. The composition and density of human tissues are known to vary depending on the sex, age and disease state of an individual. Yang *et al.*[10] estimated that variations of 4% in density, 2% calcium content, and 1% hydrogen content are reasonable estimations for human tissues. With these variations introduced, Yang *et al.*[10] found root mean square (RMS) errors of 2.2%, 2.0%, and 1.3%, respectively, in the predicted proton SPR when obtained via a SECT HU–SPR stoichiometric calibration curve. The variation in the other major constituents of human tissue, carbon, and oxygen, was found to have a negligible effect on proton SPR calculation accuracy. The RMS errors presented by Yang *et al.* for proton SPR calculation via SECT are comparable with the RMS error value of 2.3% obtained for the Catphan plastics in the current work. This supports the use of the reference plastic materials for generating the stoichiometric calibration curves and suggests the results obtained with Catphan are representative of the level of SPR accuracy one can expect when assuming an individual is composed of ICRU tissues.

The Catphan was used in the current work as it provided an inhomogeneous object with vendor supplied compositions. This allowed for a comparison of dose calculated with SECT and DECT calibration techniques with a reference dose calculated via a Catphan material-specific calibration table. Variations in quoted hydrogen content and density were incorporated to assess the uncertainty in the reference calibration of HU–SPR and HU–density functions based on vendor supplied composition data. Reasonable variations of 1% in hydrogen content and 0.5% in density resulted in 0.05%–0.09% variation in reference stopping power values of the Catphan. DECT calculated SPRs were still significantly closer to the reference values when uncertainties were taken into account.

It was found that DECT was able to estimate the true SPR of the Catphan with greater accuracy than SECT. Although the correlation of the Catphan inserts with the calibration curves shown in Fig. 2 suggests SECT should result in superior calculation of the SPRs of Catphan, the opposite was found to be true. This is due to the fact that relative electron density, which is the dominant material parameter in proton SPRs, can be extracted directly by DECT. This is in contrast to the SECT approach which relies on a direct conversion of HU to SPR via the calibration curve shown in Fig. 2(a). The calibration curve for DECT [Fig. 2(b)] has only a minor influence on SPR calculation accuracy because the mean excitation energy is of secondary importance to relative electron density. Therefore, if the composition of the imaged material does not correspond well with the materials used to derive the calibration curves, larger errors can be expected on average for SECT than DECT.

The current work has demonstrated the superior robustness of DECT for proton therapy planning with real CT images acquired with a rescanning DECT approach for a clinical wide-bore radiotherapy CT-simulator. However, Figs. 3(b) and 4(b) demonstrate the higher noise levels one can expect from a SPR image calculated with DECT. This results from the combination of the uncorrelated noise in the low and high kV images. Further work will investigate the use of methods such as iterative reconstruction[25] to reduce this noise in DECT images.

The effect of SECT and DECT SPR calibration techniques on IMPT dose calculation accuracy was demonstrated. Significant errors (maximum of 7.8%) in dose calculation were found at the edges of the target region when dose was calculated on

the SECT image set. These errors were not reproduced when dose was calculated on the DECT image set (maximum of 2.1%).

To investigate differences in calculated dose in realistic human geometries, SECT and DECT based treatment plans simulating a base of skull chordoma in the Rando anthropomorphic phantom were created. While a reference dose distribution could not be calculated in this case due to the unknown composition of the real human skeleton in the Rando phantom, dose differences resulting from calculations on SECT and DECT image sets of a similar magnitude to those observed in the Catphan were reproduced. This suggests that the results obtained with the Catphan are a reasonable representation of potential advantages of DECT over SECT based clinical IMPT treatment planning.

5. CONCLUSION

DECT is capable of calculating the Z_{eff} and ρ_e of materials by processing two sets of CT images acquired with different X-ray spectra. These images have been incorporated into a commercial proton therapy treatment planning system and the associated improvement in dose calculation over the conventional SECT method has been demonstrated. Further work is required to reduce the noise of Z_{eff} data in DECT, which results from compounding of uncorrelated noise in the two CT images acquired.

ACKNOWLEDGMENT

The authors acknowledge the support of Philips Healthcare in providing an evaluation agreement for the PINNACLE[3] research release of intensity modulated proton therapy planning.

CONFLICT OF INTEREST DISCLOSURE

The authors have no COI to report.

[a]Author to whom correspondence should be addressed. Electronic mail: scott.penfold@adelaide.edu.au

[1]B. Schaffner, E. Pedroni, and A. Lomax, "Dose calculation models for proton treatment planning using a dynamic beam delivery system: An attempt to include density heterogeneity effects in the analytical dose calculation," Phys. Med. Biol. **44**, 27–41 (1999).
[2]A. Tourovsky, A. Lomax, U. Schneider, and E. Pedroni, "Monte Carlo dose calculations for spot scanned proton therapy," Phys. Med. Biol. **50**, 971–981 (2005).
[3]U. Schneider, E. Pedroni, and A. Lomax, "The calibration of CT Hounsfield units for radiotherapy treatment planning," Phys. Med. Biol. **41**, 111–124 (1996).
[4]ICRU, "Tissue substitutes in radiation dosimetry and measurement," International Commission on Radiation Units and Measurements Report 44, 1989.
[5]ICRU, "Photon, electron, proton, and neutron interaction data for body tissues," International Commission on Radiation Units and Measurements Report 46, 1992.
[6]D. T. Downing, J. S. Strauss, and P. E. Pochi, "Variability in the chemical composition of human skin surface lipids," J. Invest. Dermatol. **53**, 322–327 (1969).
[7]P. J. Roughley and R. White, "Age-related changes in the structure of the proteoglycan subunits from human articular cartilage," J. Biol. Chem. **255**, 217–224 (1980).
[8]J. Brožek, F. Grande, J. T. Anderson, and A. Keys, "Densitometric analysis of body composition: Revision of some quantitative assumptions," Ann. N. Y. Acad. Sci. **110**, 113–140 (1963).
[9]J. Dickerson and E. M. Widdowson, "Chemical changes in skeletal muscle during development," Biochem. J. **74**, 247–257 (1960).
[10]M. Yang, G. Virshup, J. Clayton, X. Zhu, R. Mohan, and L. Dong, "Theoretical variance analysis of single-and dual-energy computed tomography methods for calculating proton stopping power ratios of biological tissues," Phys. Med. Biol. **55**, 1343–1362 (2010).
[11]W. Schneider, T. Bortfeld, and W. Schlegel, "Correlation between CT numbers and tissue parameters needed for Monte Carlo simulations of clinical dose distributions," Phys. Med. Biol. **45**, 459–478 (2000).
[12]A. E. Bourque, J.-F. Carrier, and H. Bouchard, "A stoichiometric calibration method for dual energy computed tomography," Phys. Med. Biol. **59**, 2059–2088 (2014).
[13]P. Farace, "Experimental verification of ion stopping power prediction from dual energy CT data in tissue surrogates," Phys. Med. Biol. **59**, 7081–7084 (2014).
[14]D. C. Hansen, J. Seco, T. S. Sørensen, J. B. B. Petersen, J. E. Wildberger, F. Verhaegen, and G. Landry, "A simulation study on proton computed tomography (CT) stopping power accuracy using dual energy CT scans as benchmark," Acta Oncol. **54**, 1638–1642 (2015).
[15]N. Hudobivnik, F. Schwarz, T. Johnson, L. Agolli, G. Dedes, T. Tessonnier, F. Verhaegen, C. Thieke, C. Belka, and W. H. Sommer, "Comparison of proton therapy treatment planning for head tumors with a pencil beam algorithm on dual and single energy CT images," Med. Phys. **43**, 495–504 (2016).
[16]G. Landry, K. Parodi, J. E. Wildberger, and F. Verhaegen, "Deriving concentrations of oxygen and carbon in human tissues using single-and dual-energy CT for ion therapy applications," Phys. Med. Biol. **58**, 5029–5048 (2013).
[17]H. Bichsel, *Passage of Charged Particles Through Matter* (Department of Physics, California University, Berkeley, CA, 1969).
[18]ICRU, "Ranges for protons and alpha particles," International Commission on Radiation Units and Measurements Report 49, 1993.
[19]R. Rutherford, B. Pullan, and I. Isherwood, "Measurement of effective atomic number and electron density using an EMI scanner," Neuroradiology **11**, 15–21 (1976).
[20]G. Landry, J. Seco, M. Gaudreault, and F. Verhaegen, "Deriving effective atomic numbers from DECT based on a parameterization of the ratio of high and low linear attenuation coefficients," Phys. Med. Biol. **58**, 6851–6866 (2013).
[21]M. Bazalova, J.-F. Carrier, L. Beaulieu, and F. Verhaegen, "Dual-energy CT-based material extraction for tissue segmentation in Monte Carlo dose calculations," Phys. Med. Biol. **53**, 2439–2456 (2008).
[22]N. Hünemohr, H. Paganetti, S. Greilich, O. Jäkel, and J. Seco, "Tissue decomposition from dual energy CT data for MC based dose calculation in particle therapy," Med. Phys. **41**, 061714 (14pp.) (2014).
[23]N. Hünemohr, B. Krauss, C. Tremmel, B. Ackermann, O. Jäkel, and S. Greilich, "Experimental verification of ion stopping power prediction from dual energy CT data in tissue surrogates," Phys. Med. Biol. **59**, 83–96 (2014).
[24]C. G. Ainsley and C. M. Yeager, "Practical considerations in the calibration of CT scanners for proton therapy," J. Appl. Clin. Med. Phys. **15**, 202–220 (2014).
[25]G. Landry, M. Gaudreault, W. van Elmpt, J. E. Wildberger, and F. Verhaegen, "Improved dose calculation accuracy for low energy brachytherapy by optimizing dual energy CT imaging protocols for noise reduction using sinogram affirmed iterative reconstruction," Z. Med. Phys. **26**, 75–87 (2015).

Chapter 4

Total variation superiorization in dual-energy CT reconstruction for proton therapy treatment planning

The following forms the basis of this chapter.

Zhu, Jiahua, and Scott N. Penfold. "Total Variation Superiorization in Dual-energy CT Reconstruction for Proton Therapy Treatment Planning" Inverse Problem, Vol 33, No.4 (2017)

4.1 Introduction and motivation

DECT was proposed as an imaging modality in proton therapy because it can improve the accuracy of dose calculation. However, for effective use, two high quality images with low noise in particular are required. Hence, a new iterative reconstruction algorithm was investigated and compared to the traditional filtered back projection algorithm for image reconstruction to actualise this aim.

In this chapter, an iterative technique known as diagonally relaxed orthogonal projections with total variation superiorization (TVS-DROP) is used to reconstruct the CT images. Comparing with the images reconstructed by SECT, the images derived from DECT demonstrate superior image quality. Moreover, quantitative accuracy and variance of proton SPR derived from each image set prove that CT images reconstructed with TVS-DROP result in more accurate calculation of SPR. Finally, dose deposition calculation with DECT images is found to be closer to the theoretical dose deposition.

4.2 Statement of Contribution

4.2.1 Conception

The idea to compare the benefits of image reconstruction algorithms on dose calculation in proton TPS was first conceptualised by Scott Penfold. The method to analyse the image quality and the dose difference in proton TPS was conceptualised by all authors.

4.2.2 Realisation

The theory was developed by Jiahua Zhu. The model was then checked by Scott Penfold. Matlab code and GPU-CUDA code were performed by Jiahua Zhu and checked by Scott Penfold.

4.2.3 Documentation

This paper was primarily written by Jiahua Zhu. Editing was performed by all authors

Statement of Authorship

Title of Paper	Total Variation Superiorization in Dual-energy CT Reconstruction for Proton Therapy Treatment Planning
Publication Status	☑ Published ☐ Accepted for Publication ☐ Submitted for Publication ☐ Unpublished and Unsubmitted work written in manuscript style
Publication Details	Zhu, Jiahua and Scott N. Penfold, "Total Variation Superiorization in Dual-energy CT Reconstruction for Proton Therapy Treatment Planning," Inverse Problems, Vol 33, Number 4, (2017)

Principal Author

Name of Principal Author (Candidate)	Jiahua Zhu
Contribution to the Paper	Developed GPU-CUDA code for image reconstruction algorithm. Analysed the data in the image and evaluated image quality. Designed proton plan to compare the dose deposition of traditional plan and the new plan with advanced image reconstruction algorithm. Wrote the manuscript and acted as corresponding author.
Overall percentage (%)	85%
Certification:	This paper reports on original research I conducted during the period of my Higher Degree by Research candidature and is not subject to any obligations or contractual agreements with a third party that would constrain its inclusion in this thesis. I am the primary author of this paper.
Signature	Date 3/3/2017

Co-Author Contributions

By signing the Statement of Authorship, each author certifies that:

i. the candidate's stated contribution to the publication is accurate (as detailed above);

ii. permission is granted for the candidate in include the publication in the thesis; and

iii. the sum of all co-author contributions is equal to 100% less the candidate's stated contribution.

Name of Co-Author	Scott Penfold		
Contribution to the Paper	Supervised development of the work, helped in data analysis and manuscript preparation.		
Signature		Date	3/3/2017

Name of Co-Author			
Contribution to the Paper			
Signature		Date	

Please cut and paste additional co-author panels here as required.

IOP Publishing Inverse Problems

Inverse Problems **33** (2017) 044013 (18pp) https://doi.org/10.1088/1361-6420/33/4/044013

Total variation superiorization in dual-energy CT reconstruction for proton therapy treatment planning

Jiahua Zhu[1,3] **and Scott Penfold**[1,2]

[1] Department of Physics, University of Adelaide, Adelaide, SA 5005, Australia
[2] Department of Medical Physics, Royal Adelaide Hospital, Adelaide, SA 5000, Australia

E-mail: jiahua.zhu@adelaide.edu.au

Received 26 April 2016, revised 12 September 2016
Accepted for publication 30 November 2016
Published 1 March 2017

Abstract

Proton therapy is a precise form of radiotherapy in which the range of an energetic beam of protons within a patient must be accurately known. The current approach based on single-energy computed tomography (SECT) can lead to uncertainties in the proton range of approximately 3%. This range of uncertainty may lead to under-dosing of the tumour or over-dosing of healthy tissues. Dual-energy CT (DECT) theoretically has the potential to reduce these range uncertainties by quantifying electron density and the effective atomic number. In practice, however, DECT images reconstructed with filtered backprojection (FBP) tend to suffer from high levels of noise. The objective of the current work was to examine the effect of total variation superiorization (TVS) on proton therapy planning accuracy when compared with FBP. A virtual CT scanner was created with the Monte Carlo toolkit Geant4. Tomographic images were reconstructed with FBP and TVS combined with diagonally relaxed orthogonal projections (TVS-DROP). A total variation minimization (TVM) filter was also applied to the image reconstructed with FBP (FBP-TVM). Quantitative accuracy and variance of proton relative stopping power (RSP) derived from each image set was assessed. Mean RSPs were comparable with each image; however, the standard deviation of pixel values with TVS-DROP was reduced by a factor of 0.44 compared with the FBP image and a factor of 0.66 when compared with the FBP-TVM image. Proton doses calculated with the TVS-DROP image set were also better able to predict a reference dose distribution when compared with the FBP and FBP-TVM image sets. The study demonstrated the potential advantages of TVS-DROP as an image reconstruction method for DECT applied to proton therapy treatment planning.

[3] Author to whom any correspondence should be addressed.

Keywords: total variation superiorization, dual-energy CT, relative stopping power, proton therapy

(Some figures may appear in colour only in the online journal)

1. Introduction

Proton therapy is an expanding form of cancer treatment. While the particle accelerators required for proton therapy are significantly larger and more expensive than those required for traditional x-ray radiotherapy therapy, the physics of proton interactions with matter are favourable to those of x-rays when attempting to treat deep-seated tumours. While modern approaches to treatment with x-rays can result in target conformity similar to proton therapy, the latter requires a lower dose be deposited in healthy tissue surrounding the tumour, potentially reducing the risk of treatment side effects.

Treatment planning with proton therapy requires an accurate prediction of how the therapeutic proton beam will interact with the patient. The most important parameter to be quantified is that of relative stopping power (RSP). Conventionally, single-energy computed tomography (SECT) Hounsfield units (HU) are converted to RSPs via an empirically derived piecewise linear calibration function. The proton range uncertainty resulting from such an approach has been investigated by a number of authors [1–5]. Two alternative approaches have been proposed; dual-energy CT (DECT) and proton CT (pCT). A number of groups are working to develop prototype systems of the latter [6–9] and experiments with total variation superiorization (TVS) in pCT have already been conducted [10].

DECT is a form of tomographic imaging in which the imaged object (the patient in this case) is scanned with two x-ray beams differing in energy. In most applications, two reconstructed images are produced representing the attenuation properties of tissue in the two x-ray spectra. Processing of the two image sets allows for a calculation of electron density and effective atomic number. While early works in proton therapy treatment planning [11] suggested that DECT would be useful for determining electron density of tissues, Yang *et al* [12] were the first to propose the use of both electron density and the effective atomic number for the calculation of proton RSP. They demonstrated that the effective atomic number could be correlated with the mean excitation potential of tissues. As electron density and mean excitation potential are the only material dependent parameters in the calculation of RSP, DECT is well suited for this application. A number of recent publications have investigated the application of DECT to proton RSP calculation [12–14] and treatment planning [15, 16].

A limitation of DECT is that any noise in the reconstructed images is amplified in the calculation of the effective atomic number [17]. DECT images reconstructed with filtered backprojection (FBP) typically result in poor contrast when examining the effective atomic number distribution. To counter this, one vendor has released DECT scanning with sinogram-affirmed iterative reconstruction (SAFIRE). This algorithm iterates through both the raw data space to ensure correct quantitative reconstructions and the image space to reduce noise. This is conceptually similar to the process of TVS coupled with an iterative reconstruction algorithm, but the advantages of superiorization and feasibility seeking over minimization may not be realised in SAFIRE [18].

The aim of the current work was to compare the effect of the DECT image reconstruction method on dose calculation accuracy in proton therapy. Three approaches were examined; FBP, FBP followed by post-processing total variation minimization (FBP-TVM) and iterative reconstruction utilizing TVS coupled with diagonally relaxed orthogonal projections (TVS-DROP).

2. Methods

2.1. Monte Carlo CT simulation

The Geant4 Monte Carlo toolkit [19] was used to simulate an ideal fan beam CT scanner. Geant4 allows for the simulation of radiation with matter in a stochastic manner. The radiation source of the virtual CT scanner was a point source of x-rays. The x-ray energy spectrum for the 90 kVp and 140 kVp tube settings of a Philips brilliance big bore CT-simulator (Philips Radiation Oncology Systems, Fitchburg, WI) were obtained from the manufacturer. The Geant4 general particle source (GPS) was used as the simulator for these polyenergetic CT spectra.

A 40° detector arc was placed at a distance of 1 m opposite to the radiation source. The detector array consisted of 2000 discrete detector bins, each occupying 0.02°. Individual detector bins recorded the direction and unique identification number of each particle that entered its volume. A virtual collimator was simulated by placing a transparent sensitive volume close to the point source of radiation. When an x-ray traversed an element of the detector array, the direction of the x-ray at this point and the transparent detector was compared and an event counted if the direction through the imaged object was unchanged. Projections of the CT scanner were recorded in 1° increments over 360°.

An elliptical water phantom containing 17 different tissue types was placed at the centre of the CT scanner. The phantom and the location of the inserts is shown in figure 1 and the CT simulation is shown in figure 2. The composition of the inserts was derived from ICRU 44 [20] and is shown in table 1. Four simulations were run to obtain the integral attenuation along a ray joining the radiation point source and each detector bin; a simulation with each x-ray energy spectrum and with the phantom in and out of the beam. The output of the simulation was an array with each element containing the number of photons that did not change direction from the transparent detector at the source and the detector array at 1 m. Each simulation consisted of 2×10^9 primary photons per rotation angle.

2.2. Image reconstruction techniques

Three image reconstruction and processing techniques were investigated; FBP, FBP followed by post-processing with a TV minimization algorithm (FBP-TVM), and TVS applied to the DROP iterative reconstruction algorithm (TVS-DROP). A brief description of each reconstruction approach is given below.

2.2.1. Filtered backprojection. The well-known FBP algorithm has been broadly adopted in commercial CT products. The algorithm is based on a discrete implementation of the inverse radon transform of the measured sinogram. In the current work the MATLAB (The MathWorks, Inc., Natick, MA) the *ifanbeam* function was used to reconstruct the image from the Geant4 simulation data. The Shepp–Logan filter [21] option was selected. The reconstructed image was a 400×400 pixel image with a square pixel size of 1 mm.

2.2.2. Total variation minimization post-processing. In general terms, TV in image processing is a global measure of the level of change between neighbouring pixel values and can be calculated with equation (1). It was first proposed as a quantification of image noise by Rudin *et al* [22], and many investigations have since demonstrated that a reduction of TV can result in images with decreased noise, while maintaining spatial resolution [23–25].

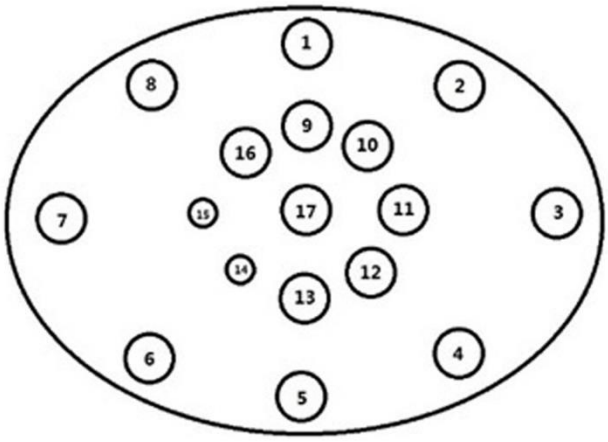

Figure 1. The simulated phantom with location and identification number of ICRU 44 tissue inserts listed in table 1. The cross-sectional dimensions of the phantom are $330 \times 270\,\mathrm{mm}^3$. The position of each insert is listed in table 1. Insert diameter is 32 mm, with the exception of inserts 14 and 15, which are 20 mm in diameter. The body material of the phantom is water.

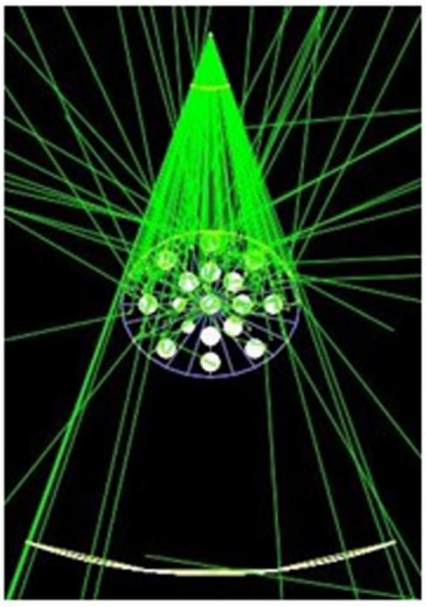

Figure 2. Geant4 CT simulation with the ICRU 44 phantom. Green lines denote photon trajectories.

Table 1. Elemental fractions by weight, density and electron density of 17 representative human tissues from ICRU 44. Reproduced with permission from [20]. ICRU (1989). International Commission on Radiation Units and Measurements, Tissue Substitutes in Radiation Dosimetry and Measurement, ICRU Report 44 (International Commission on Radiation Units and Measurements, Bethesda, Maryland).

	Element	H	C	N	O	Na	Mg	P	S	Cl	K	Ca	Fe			Insert position relative to phantom centre (cm)	
	Z	1	6	7	8	11	12	15	16	17	19	20	26				
	A	1.01	12.01	14.01	16.00	22.99	24.31	30.97	32.07	35.45	39.10	40.08	55.85				
ID	I (eV)	21.8	78.0	82.0	95.0	149.0	156.0	173.0	180.0	174.0	190.0	191.0	286.0	ρ (g cm^{-3})	ρ_e (10^{23}e g^{-1})	x	y
1	Adipose	0.112	0.517	0.013	0.355	0.001	0	0	0.001	0.001	0	0	0	0.97	3.24	0	11.60
2	Blood	0.102	0.110	0.033	0.745	0.001	0	0.001	0.002	0.003	0.002	0	0.001	1.06	3.51	8.20	8.20
3	Brain	0.107	0.145	0.022	0.712	0.002	0	0.004	0.002	0.003	0.003	0	0	1.04	3.46	11.60	0
4	Breast	0.115	0.387	0	0.498	0	0	0	0	0	0	0	0	0.96	3.22	8.20	−8.20
5	Eyelens	0.096	0.195	0.057	0.646	0.001	0	0.001	0.003	0.001	0	0	0	1.07	3.53	0	−11.60
6	GI tract	0.106	0.115	0.022	0.751	0.001	0	0.001	0.001	0.002	0.001	0	0	1.03	3.42	−8.20	−8.20
7	Heart	0.104	0.139	0.029	0.718	0.001	0	0.002	0.002	0.002	0.003	0	0	1.05	3.48	−11.60	0
8	Kidney	0.103	0.132	0.030	0.724	0.002	0	0.002	0.002	0.002	0.002	0.001	0	1.05	3.51	−8.20	8.20
9	Lipid	0.118	0.773	0	0.109	0	0	0	0	0	0	0	0	0.92	3.09	0	5.90
10	Liver	0.102	0.139	0.030	0.716	0.002	0	0.003	0.003	0.002	0.003	0	0	1.06	3.51	4.17	4.17
11	Lung	0.103	0.105	0.031	0.749	0.002	0	0.002	0.003	0.003	0.002	0	0	0.26	8.62	5.90	0
12	Muscle	0.102	0.143	0.034	0.71	0.001	0	0.002	0.003	0.001	0.004	0	0	1.05	3.48	4.17	−4.17
13	Cartilage	0.096	0.099	0.022	0.744	0.005	0	0.022	0.009	0.003	0	0	0	1.10	3.62	0	−5.90
14	Cortical bone	0.034	0.155	0.042	0.435	0.001	0.002	0.103	0.003	0	0	0.225	0	1.92	5.95	−4.17	−4.17
15	Femur	0.007	0.345	0.028	0.368	0.001	0.001	0.055	0.002	0.001	0	0.129	0	1.33	4.27	−5.90	0
16	Red marrow	0.105	0.414	0.034	0.439	0	0	0.001	0.002	0.002	0.002	0	0.001	1.03	3.42	−4.17	4.17
17	Water	0.112	0	0	0.888	0	0	0	0	0	0	0	0	1.00	3.34	0	0

$$\varphi\left(p^{k}\right)=\sum_{g=1}^{J-1}\sum_{l=1}^{J-1}\sqrt{\left(x_{g+1,l}^{k}-x_{g,l}^{k}\right)^{2}+\left(x_{g,l+1}^{k}-x_{g,l}^{k}\right)^{2}}, \tag{1}$$

where φ is the total variation of image, J is the number of row or column (we estimate the numbers of row and column are same), x is the iterated attenuation coefficient and k is the iterative times.

In the current work a MATLAB function based on the work of Rudin *et al* [22] was used to reduce the TV of the FBP image. Rudin *et al*'s approach is a constrained optimization algorithm for removing noise from the image by minimizing the total variation of images. This constrained algorithm is based on Lagrange multipliers and uses the gradient projection method to solve a time dependent partial differential equation (PDE).

The standard deviation of pixel values in the input image was required by the function. It was found that inputting a value of 0.5σ resulted in less noisy images, while still maintaining correct pixel values. While larger values for this parameter could produce less noisy images, the algorithm, acting as a filter, also tended to alter pixel values bringing outlying values towards the mean value of the phantom.

2.2.3. Iterative reconstruction with TVS. An alternative to the inverse radon transform of FBP, is to perform iterative image reconstruction. The problem of x-ray CT can be modelled as a collection of linear equations (equation (2)).

$$Ax=b \tag{2}$$

Here, A is an $I\times J$ matrix whose elements $a_{i,j}$ correspond to the length of the intersection of the ith ray with the jth pixel. x is a J-dimensional vector whose elements correspond to the linear attenuation coefficients of pixel j and b is an I-dimensional vector whose elements correspond to

$$b_{i}=\ln\left(\frac{I_{0,i}}{I_{i}}\right), \tag{3}$$

where I_i and $I_{0,i}$ are the number of photons measured at detector I with and without the phantom in place, respectively.

The earliest application of projection algorithms to CT reconstruction was demonstrated by Herman *et al* [26] with the algebraic reconstruction technique (ART) algorithm. The basis of this iterative projection algorithm is to sequentially perform orthogonal projections from the current image estimate onto the hyperplanes formed by each of the linear equations forming the rows of equation (2). As the iterations approach infinity, the solution estimate approaches the least squares solution to equation (2).

Since the initial demonstration of ART as an image reconstruction tool, a number of other projection algorithms have been applied to this field. Algorithms vary from fully sequential to fully simultaneous [27] with block-iterative [28–32] and string-averaging techniques [33] lying in between the two extremes. In the current work a block-iterative algorithm known as DROP [31] was used. This algorithm has been compared with other projection algorithms and has demonstrated minor noise and convergence rate advantages with pCT data [34].

DROP may be coupled with TVS in order to reduce image noise. The application of TVS-DROP to pCT has been demonstrated in previous work [10]. In [10], the noise reduction properties and maintenance of spatial resolution was successfully demonstrated. In the current work the TVS1-DROP* algorithm of Penfold *et al* [10] was modified to reconstruct x-ray CT images as opposed to pCT images and is here referred to as TVS-DROP. The algorithmic structure of TVS-DROP is summarized in algorithm 1.

Algorithm 1

(1) Set $k = 0$
(2) set $x^k = 0$, and $\beta_k = 1$
(3) repeat for around 150 cycles
(4) set s to a subgradient of φ at x^k
(5) if $s > 0$ set $v^k = -s/s$
(6) else set $v^k =$ s
(7) set *continue* = *true*
(8) while *continue*
(9) set $y^k = x^k + \beta_k v^k$
(10) calculate the merit function (total variation) with equation (1) and if $\varphi(y^k) \leqslant \varphi(x^k)$
(11) apply sequentially M times the projection operator $P_{t(k)}$ to y^k
(12) set $x^{k+1} = P_M y$
(13) set *continue* = *false*
(14) else set $\beta_k = \beta_k/2$
(15) else set $\beta_k = \beta_k/2$
(16) set $k = k + 1$

In algorithm 1, x^k denotes the vector of linear attenuation coefficients at iteration k, s is the subgradient of total variation as calculated with the method outlined in [35] and $P_{t(k)}$ denotes the DROP projection operator described in [10].

The reconstruction was performed with a uniform zero initial image estimate and run on a CPU-GPU workstation. The rows of equation (2) were divided into 20 blocks, with 100 detectors from each projection forming a block. It was found that 150 iterations were required for optimal image reconstruction results.

2.3. Quantitative CT accuracy analysis

Reconstruction accuracy was assessed by defining a region of interest for each insert shown in figure 1 and calculating the mean and standard deviation of pixel values. For x-ray CT, pixel values represent the mean linear attenuation coefficient for the x-ray energy spectrum used. Furthermore, the coefficient of determination (R^2) provides a single metric to evaluate how closely the reconstructed linear attenuation coefficients match the theoretical values. Conceptually, the R^2 value of an image corresponds to the accuracy of fit when a plot of the expected value against the reconstructed value for each pixel is fit with a straight line of gradient 1 and intercept of 0. This analysis method was applied to the reconstruction of the linear attenuation coefficient, using the known composition of the phantom simulated in Geant4.

2.4. Relative stopping power calculation

While the reconstruction approaches above generate a map of x-ray linear attenuation coefficients, the required quantity for proton therapy treatment planning is the RSP. Stopping power (S) describes the energy lost per unit length of energetic charged particles. Energy losses due to ionization and excitation of atomic electrons are the primary interaction mechanism of protons in the therapeutic energy range. The stopping power for this interaction can be described by the Bethe equation [36] (equation (4)).

$$S = -\frac{\mathrm{d}E}{\mathrm{d}x} = \frac{4\pi}{\beta^2} r_e^2 m_e c^2 \rho_e \left[\ln\left(\frac{2m_e c^2}{I} \frac{\beta^2}{1-\beta^2} \right) - \beta^2 \right]. \tag{4}$$

Here, β is the velocity of the particle relative to the speed of light c, r_e is the classical electron radius, m_e is the electron rest mass, ρ_e is the number of electrons per unit volume, and I is the mean excitation energy of the material.

The RSP represents the ratio of the stopping power of a given material to that of water. The advantage of using the RSP rather than S of a given material during treatment planning is that the RSP is independent of proton energy to a good approximation for most human tissues, meaning that the energy dependent S of water can be scaled by the appropriate RSP.

The two material dependent parameters in the RSP are the relative electron density, and the mean excitation energy. A brief description of how these quantities can be obtained from DECT is given.

Let us assume the three image reconstruction/processing approaches described above result in the creation of a map of linear attenuation coefficients at 90 kVp and 140 kVp. The linear attenuation coefficient can be written in terms of the electron density as

$$\mu(Z,E) = \rho_e({}_e\sigma_{\mathrm{PE}}(Z,E) + {}_e\sigma_{\mathrm{coh}}(Z,E) + {}_e\sigma_{\mathrm{incoh}}(Z,E)), \tag{5}$$

where ${}_e\sigma_{\mathrm{PE}}$, ${}_e\sigma_{\mathrm{coh}}$ and ${}_e\sigma_{\mathrm{incoh}}$ are the electronic interaction cross sections for the photoelectric effect, coherent scattering, and incoherent scattering respectively. These cross sections have an atomic number (Z) and photon energy (E) dependence. Schneider *et al* [1] suggested that equation (5) can be approximated by equation (6)

$$\mu(Z,E) = \rho_e[K^{\mathrm{incoh}}(E) + Z^{1.86}K^{\mathrm{coh}}(E) + Z^{3.62}K^{\mathrm{PE}}(E)], \tag{6}$$

where K^{PE}, K^{coh} and K^{incoh} are x-ray spectra dependent variables corresponding to the relative contribution of photoelectric absorption, coherent scattering and incoherent scattering, respectively, to total attenuation. Schneider *et al* [37] also proposed a means for obtaining these parameters for a given CT scanner.

Taking the ratio of the reconstructed pixel values at 90 kVp and 140 kVp, the electron density dependence is removed and we are left only with an expression in terms of atomic number.

$$\frac{\mu_{90}}{\mu_{140}} = \frac{[K_{90}^{\mathrm{incoh}} + Z^{1.86}K_{90}^{\mathrm{coh}} + Z^{3.62}K_{90}^{\mathrm{PE}}]}{[K_{140}^{\mathrm{incoh}} + Z^{1.86}K_{140}^{\mathrm{coh}} + Z^{3.62}K_{140}^{\mathrm{PE}}]}. \tag{7}$$

Equation (7) can be solved for Z with numerical means. The solution is known as the effective atomic number of the pixel, Z_{eff}.

Yang *et al* [12] demonstrated that Z_{eff} obtained with DECT could be correlated with the natural logarithm of the mean excitation energy. The correlation of these quantities for ICRU 44 tissues is shown in figure 3.

Having obtained the mean excitation energy, the electron density is now required to complete the calculation of RSP. In the current work the method of Saito [38] was implemented. Here, the electron density is determined from a difference of HU values in the two images, where the HU is defined as

$$\mathrm{HU} = 1000\left(\frac{\mu - \mu_{\mathrm{w}}}{\mu_{\mathrm{w}}} \right). \tag{8}$$

In equation (8), μ_{w} is the attenuation coefficient of water for the given x-ray energy spectrum. Saito suggested the calculation of electron density from

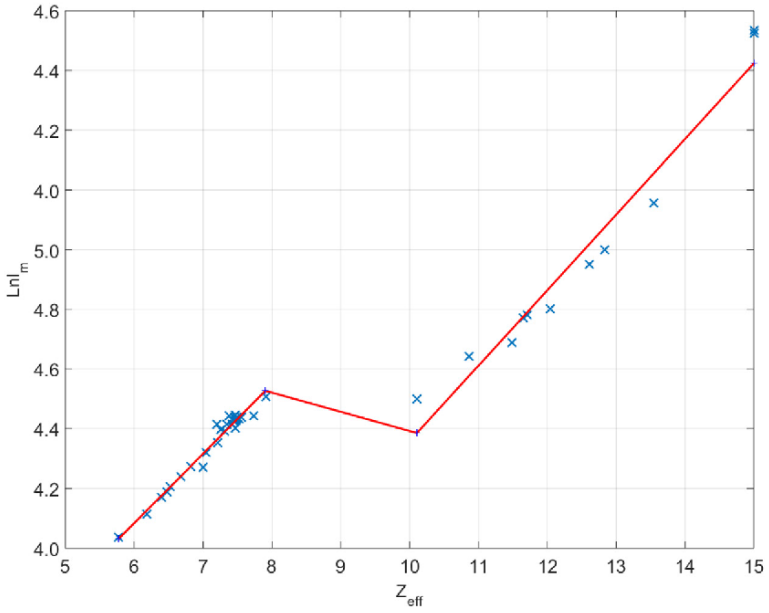

Figure 3. Correlation between Z_{eff} and $\text{Ln}I_m$ for the ICRU 44 tissue dataset.

$$\rho_{\text{e}} = \frac{\Delta\text{HU}}{1000} + 1, \tag{9}$$

where

$$\Delta\text{HU} = (1+\alpha)\text{HU}_{\text{H}} - \alpha\text{HU}_{\text{L}}. \tag{10}$$

Here, HU_{H} and HU_{L} are the HU obtained from the higher (140 kVp) and lower (90 kVp) energy CT scans, respectively, and α is a scanner dependent variable. The reader is referred to Saito [38] for a description of the method for obtaining α.

Incorporating the mean excitation energy and the relative electron density into equation (4), the RSP at a representative kinetic energy can be calculated.

2.5. Proton therapy treatment planning

The Philips Pinnacle^3 (Philips Radiation Oncology Systems, Fitchburg, WI) radiotherapy treatment planning system (TPS) is a research release of proton pencil beam scanning that includes intensity modulated proton therapy (IMPT) optimization algorithms. All current commercial proton TPS systems are designed to import SECT images of HU and apply a conversion to RSPs. In a recent work [16] we presented a method to incorporate DECT images into the TPS and demonstrated the advantages in dose calculation accuracy when using DECT rather than SECT image sets.

Using the same approach as in [16], the three RSP image sets derived from DECT scanning were imported to the Pinnacle^3 TPS. A reference image set was also imported, containing the same geometrical and material properties as the phantom used in the Geant4 CT simulation. Although the CT simulation only allowed for 2D (x,y) image reconstruction, each reconstruction was extended in the z-dimension to create a 3D image set for proton therapy planning.

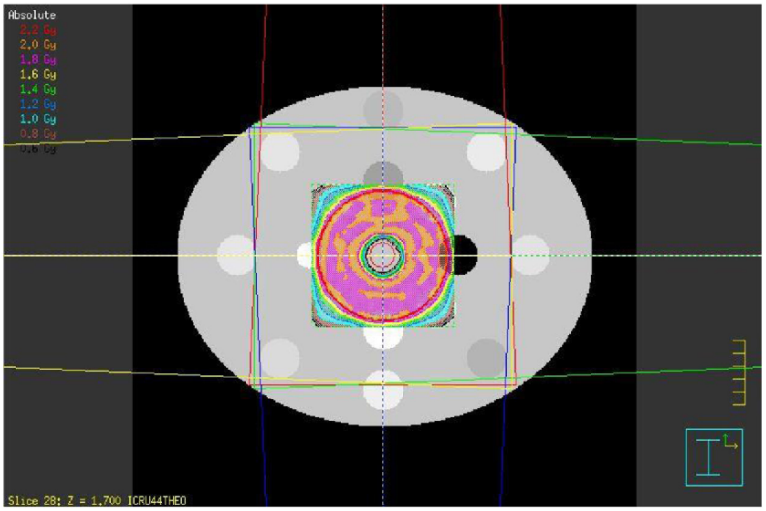

Figure 4. Axial view of proton treatment plan in Pinnacle^3 TPS with reference image set. Solid coloured lines emerging from the side of the figure represent the maximum divergence of each beam, with dashed lines representing the central axis. The Bragg peak locations of each pencil beam were contained within the target volume and thus maximum divergence was not required. Colour wash shows optimized uniform dose distribution of 2 Gy to donut target volume.

A donut shaped target region was contoured on the reference image. Four cardinal beam directions were selected to deliver proton pencil beams to the target region. A lateral pencil beam spacing of 0.6 cm and 80% layer overlap were selected. A screenshot of dose calculated on the reference image set is shown in figure 4.

Dose was calculated on a 2 mm grid covering the target region. Pencil beam weights were optimized with the Pinnacle^3 IMPT algorithm. The donut target structure and pencil beam weights were then imported to treatment plans based on the three test image sets. Dose was recalculated on the test image sets without re-optimization of the pencil beam weights.

The dose grids calculated on each image set were exported from the Pinnacle^3 TPS and analysed in MATLAB. Dose difference maps were created by subtracting the dose calculated on the test image sets from that calculated with the reference image.

3. Results

3.1. CT image reconstruction

The x-ray attenuation coefficient images reconstructed from 90 kVp and 140 kVp CT scans are shown in figure 5. A quantitative comparison of reconstructed linear attenuation coefficients for the different inserts is presented in figures 6 and 7. Reference attenuation coefficients were calculated with the known composition of the inserts and equation (6). In general, all three images tended to overestimate reference attenuation coefficients. The root mean square errors (RMSE) for inserts were 1.58%, 1.54% and 1.46% for the 90 kVp images and 1.31%, 1.30% and 1.28% for the 140 kVp images using FBP, FBP-TVM and TVS-DROP reconstructions, respectively.

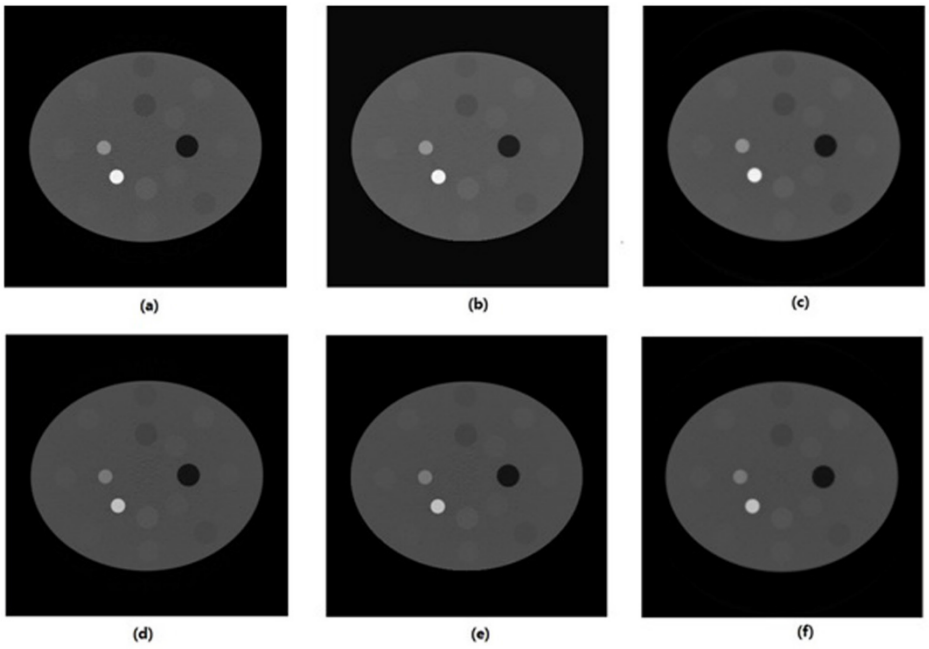

Figure 5. X-ray CT images at 90 kVp (top row) and 140 kVp (bottom row) reconstructed by (a) and (d) FBP, (b) and (e) FBP-TVM, and (c) and (f) TVS-DROP. The pixel value viewing range is 0.00–0.67.

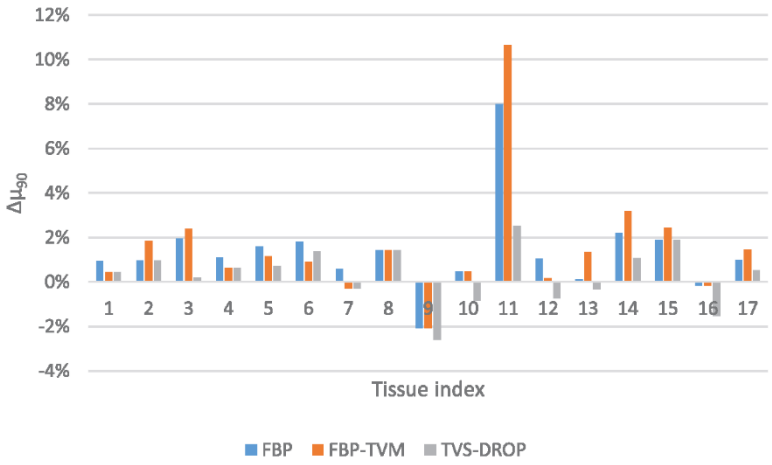

Figure 6. Relative difference in attenuation coefficient compared with theoretical attenuation coefficient at 90 kVp.

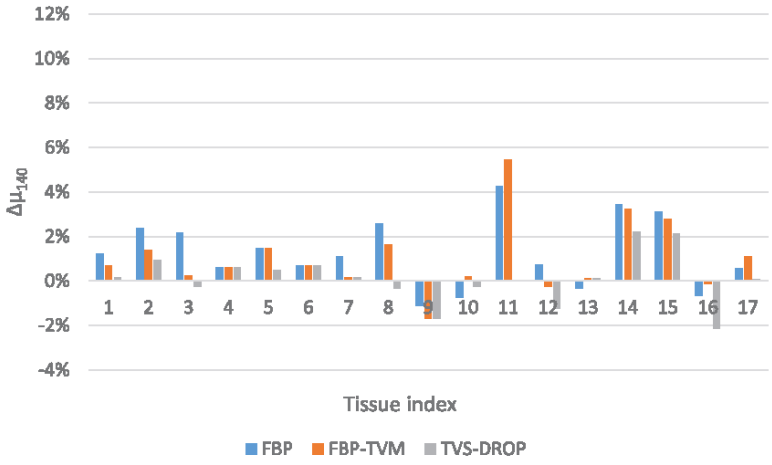

Figure 7. Relative difference of attenuation coefficient compared with theoretical attenuation coefficient at 140 kVp.

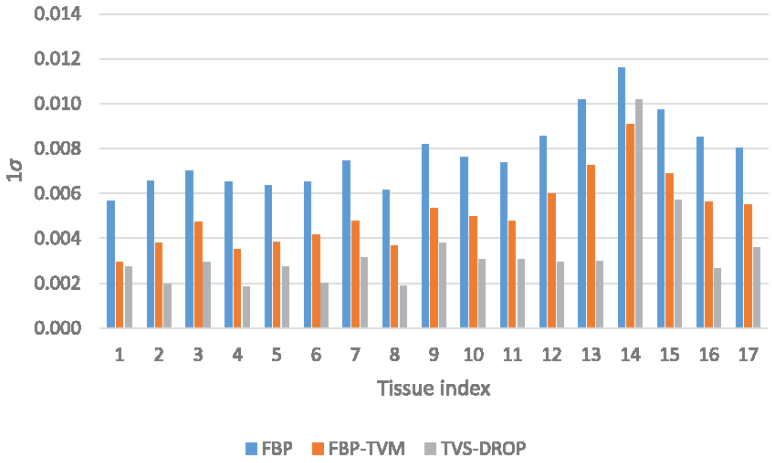

Figure 8. Standard deviations of attenuation coefficients in the 90 kVp image.

The standard deviation of pixel values within each insert are shown in figures 8 and 9. The mean standard deviations across all inserts were 7.77×10^{-3}, 5.11×10^{-3} and 3.38×10^{-3} for FBP, FBP-TVM and TVS-DROP, respectively.

The coefficient of determination combines the effects of both the quantitative accuracy and the variance of the pixel values. R^2 values for the different image sets are shown in table 2. Values closer to 1 indicate a better match of reconstructed to values calculated based on known composition. Generally, a larger R^2 value corresponds to smaller relative error, as expected. An exception to this observation occurs with the TVS-DROP reconstructions. The larger R^2 value of 90 kVp compared with 140 kVp with this reconstruction technique despite the larger average relative error with 90 kVp can be explained by the method of calculation for the two metrics. The relative error applies to regions of interest defined within the inserts. The R^2 calculation is based on the entire image, including the phantom and the surrounding air.

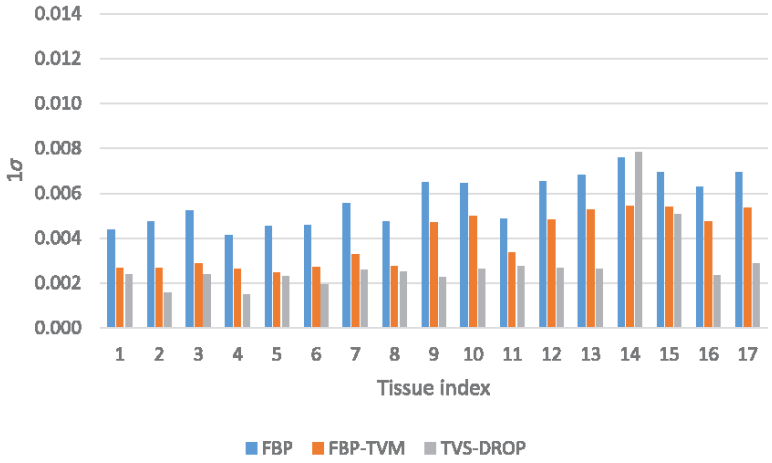

Figure 9. Standard deviations of attenuation coefficients in the 140 kVp image.

Table 2. Coefficient of determination R^2 for the reconstructed images.

Algorithm	90 kVp	140 kVp
FBP	0.753	0.765
FBP-TVM	0.771	0.779
TVS-DROP	0.832	0.814

The relative errors were found to be 0.24% and 0.34% for 90 kVp and 140 kVp reconstructions with TVS-DROP, respectively, resulting in a larger R^2 value for the 90 kVp reconstruction.

3.2. RSP calculation

Relative electron density, Z_{eff} and RSP images are shown in figure 10. It is apparent that the images derived from the TVS-DROP reconstruction contain significantly less noise than both the FBP and FBP-TVM derived images. This is particularly evident in the Z_{eff} image.

Quantitative accuracy in RSP values is of upmost importance in proton therapy planning. Relative errors of the calculated RSP values with reference values for each insert is shown in figure 11. The RMSEs in RSP were 0.096, 0.081 and 0.064 for FBP, FBP-TVM and TVS-DROP, respectively. The standard deviation of the RSPs values are also shown in figure 12 to demonstrate the improvement in noise associated with the use of TVS-DROP.

3.3. Dosimetric effect of image reconstruction method

Relative dose difference maps for each reconstruction approach compared with the reference dose distribution shown in figure 4 are presented in figure 13. Absolute dose differences were normalized to the prescription dose of 2 Gy to give a global relative difference. Significantly larger dose errors were present with the FBP and FBP-TVM images than with the TVS-DROP image. RMS percentage difference values of 0.122, 0.112 and 0.036 for FBP, FBP-TVM and TVS-DROP, respectively, were found in the square region shown in figure 4.

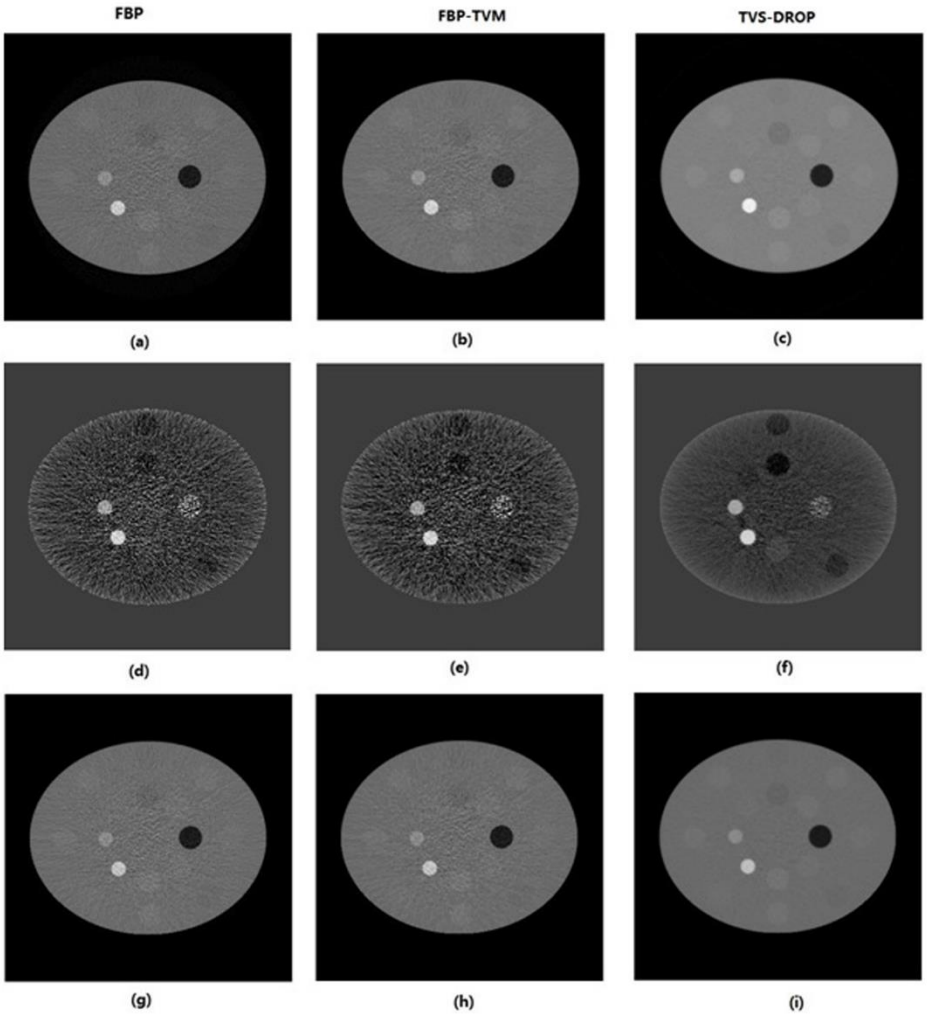

Figure 10. Electron density (top row), Z_{eff} (middle row) and RSP (bottom row) derived from FBP, FBP-TVM and TVS-DROP reconstructions. Viewing windows were set at [0, 2.4] for relative electron density [5, 15], for Z_{eff} and [0, 2.4] for RSP.

The large under-dose observed at the inner edge of the target volume was investigated. Further analysis showed that range errors of 4.7 mm, 4.5 mm and 2.1 mm were present for the beam entering from the left of the phantom with the FBP, FBP-TVM and TVS-DROP methods, respectively. This was primarily due to the overestimation of the stopping power in the high density femur insert neighbouring the target volume.

4. Discussion

All reconstruction approaches were found to result in accurate estimates of linear attenuation coefficients with insignificant differences in mean attenuation coefficient values observed. Significant differences were observed in the variance of pixel values for tissue inserts however.

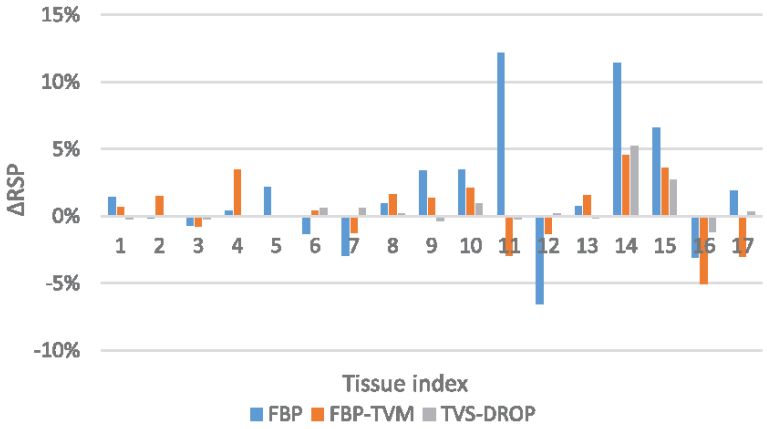

Figure 11. Relative difference in RSP between measured reconstructed images and expected values.

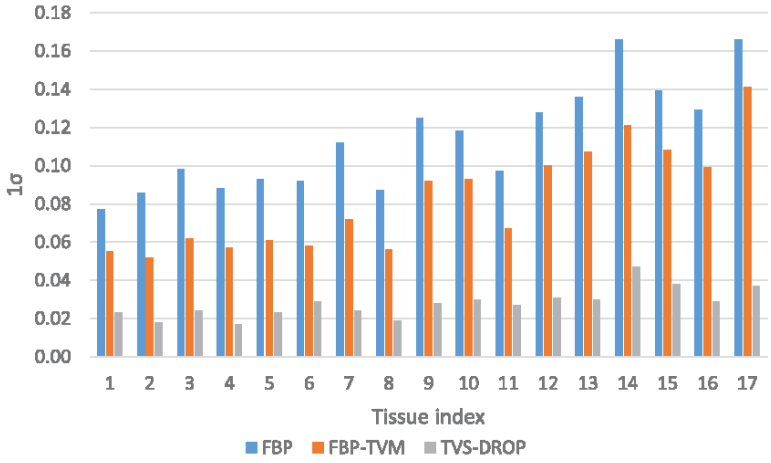

Figure 12. Standard deviation of tissues inserts derived from FBP, FBP-TVM and TVS-DROP images.

While the FBP-TVM post-processing method could be adjusted to further reduce the standard deviation of the image, it was found that this came at the expense of quantitative accuracy. More smoothing with TVM tended to force the outlying pixel values towards the mean value of the phantom.

The noise reduction possible with TVS-DROP most clearly presented itself in the calculation of effective atomic number from the two CT data sets. Effective atomic number is calculated from a ratio of corresponding pixel values in the two image sets. Furthermore, for low effective atomic number materials, as in the case of soft tissue, there is only a small difference in mass attenuation coefficients for the two energy spectra. These two factors result in particularly noisy Z_{eff} images as shown in figure 10.

The clinical dose calculation effect of noise reduction with TVS-DROP was demonstrated by comparing doses calculated on a reference phantom with that calculated on the three test image sets. A significant reduction of calculated dose RMSE was found when using the

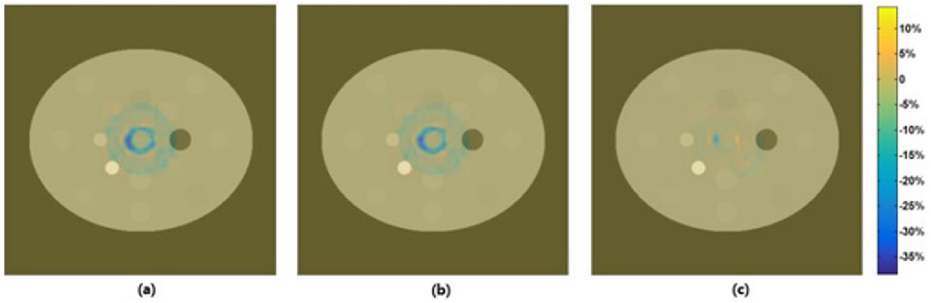

Figure 13. Relative dose differences with respect to the reference dose distribution shown in figure 4. Dose calculated on (a) FBP, (b) FBP-TVM and (c) TVS-DROP image sets.

TVS-DROP image. Acknowledging that there were no significant differences in the accuracy of x-ray attenuation coefficient reconstruction on average, this work supports the findings of Chvetsov and Paige [39] that noise in image data can have a significant impact on dose calculation accuracy in proton therapy.

The largest dose differences were found to arise from an error in calculated range of the proton beams. Range was here defined as the depth of 10% dose on the central axis of the beam. The range of the beam entering from the left of screen was 14.91 cm for the reference phantom and 14.44 cm, 14.46 cm and 14.70 cm for the FBP, FBP-TVM and TVS-DROP algorithm, respectively. This significant underestimation of the range was due to the overestimation of stopping power of the femur insert by the FBP algorithm.

An error in range calculation at the treatment planning stage can have a significant impact on treatment outcome in proton therapy. If the target region is abutting a critical structure and range is underestimated by the TPS, large doses may be delivered to the critical structure during treatment, resulting in severe side effects. Alternatively, if the range is overestimated by the TPS, the tumour may not receive a great enough dose to destroy the tumour cells, resulting in a poor probability of local control.

5. Conclusion

The application of TVS to the reconstruction of DECT images for proton therapy treatment planning was investigated. It was found that the use of TVS resulted in significantly superior estimates of proton RSP when compared with images reconstructed with FBP. This in turn translated to a significant improvement in dose calculation accuracy when generating a proton therapy treatment plan.

References

[1] Schneider U, Pedroni E and Lomax A 1996 The calibration of CT Hounsfield units for radiotherapy treatment planning *Phys. Med. Biol.* **41** 111

[2] Schaffner B and Pedroni E 1998 The precision of proton range calculations in proton radiotherapy treatment planning: experimental verification of the relation between CT-HU and proton stopping power *Phys. Med. Biol.* **43** 1579

[3] Paganetti H 2012 Range uncertainties in proton therapy and the role of Monte Carlo simulations *Phys. Med. Biol.* **57** R99
[4] Unkelbach J, Chan T C and Bortfeld T 2007 Accounting for range uncertainties in the optimization of intensity modulated proton therapy *Phys. Med. Biol.* **52** 2755
[5] Yang M, Zhu X R, Park P C, Titt U, Mohan R, Virshup G, Clayton J E and Dong L 2012 Comprehensive analysis of proton range uncertainties related to patient stopping-power-ratio estimation using the stoichiometric calibration *Phys. Med. Biol.* **57** 4095
[6] Naimuddin M, Coutrakon G, Blazey G, Boi S, Dyshkant A, Erdelyi B, Hedin D, Johnson E, Krider J and Rukalin V 2016 Development of a proton computed tomography detector system *J. Instrum.* **11** C02012
[7] Price T and PRaVDA Consortium 2016 PRaVDA: high energy physics towards proton computed tomography *Nucl. Instrum. Methods Phys. Res.* A **824** 226–7
[8] Scaringella M, Brianzi M, Bruzzi M, Bucciolini M, Carpinelli M, Cirrone G A P, Civinini C, Cuttone G, Presti D L and Pallotta S 2013 The PRIMA (PRoton IMAging) collaboration: development of a proton computed tomography apparatus *Nucl. Instrum. Methods Phys. Res.* A **730** 178–83
[9] Karonis N T, Duffin K L, Ordoñez C E, Erdelyi B, Uram T D, Olson E C, Coutrakon G and Papka M E 2013 Distributed and hardware accelerated computing for clinical medical imaging using proton computed tomography (pCT) *J. Parallel Distrib. Comput.* **73** 1605–12
[10] Penfold S, Schulte R W, Censor Y and Rosenfeld A B 2010 Total variation superiorization schemes in proton computed tomography image reconstruction *Med. Phys.* **37** 5887–95
[11] Chen G T, Singh R P, Castro J R, Lyman J T and Quivey J M 1979 Treatment planning for heavy ion radiotherapy *Int. J. Radiat. Oncol. Biol. Phys.* **5** 1809–19
[12] Yang M, Virshup G, Clayton J, Zhu X, Mohan R and Dong L 2010 Theoretical variance analysis of single-and dual-energy computed tomography methods for calculating proton stopping power ratios of biological tissues *Phys. Med. Biol.* **55** 1343
[13] Hünemohr N, Paganetti H, Greilich S, Jäkel O and Seco J 2014 Tissue decomposition from dual energy CT data for MC based dose calculation in particle therapy *Med. Phys.* **41** 061714
[14] Hansen D C, Seco J, Sørensen T S, Petersen J B B, Wildberger J E, Verhaegen F and Landry G 2015 A simulation study on proton computed tomography (CT) stopping power accuracy using dual energy CT scans as benchmark *Acta Oncol.* **54** 1638–42
[15] Hudobivnik N, Schwarz F, Johnson T, Agolli L, Dedes G, Tessonnier T, Verhaegen F, Thieke C, Belka C and Sommer W H 2016 Comparison of proton therapy treatment planning for head tumors with a pencil beam algorithm on dual and single energy CT images *Med. Phys.* **43** 495–504
[16] Zhu J and Penfold S N 2016 Dosimetric comparison of stopping power calibration with dual-energy CT and single-energy CT in proton therapy treatment planning *Med. Phys.* **43** 2845–54
[17] Brooks R A 1977 A quantitative theory of the Hounsfield unit and its application to dual energy scanning *J. Comput. Assist. Tomogr.* **1** 487–93
[18] Landry G, Gaudreault M, van Elmpt W, Wildberger J E and Verhaegen F 2016 Improved dose calculation accuracy for low energy brachytherapy by optimizing dual energy CT imaging protocols for noise reduction using sinogram affirmed iterative reconstruction *Z. Med. Phys.* **26** 75–87
[19] Agostinelli S 2003 Geant4 collaboration *Nucl. Instrum. Methods* A **506** 01368
[20] ICRU 1989 Tissue substitutes in radiation dosimetry and measurement *International Commission on Radiation Units and Measurements Report* 44 (The International Commission on Radiation Units and Measurements)
[21] Shepp L A and Logan B F 1974 The Fourier reconstruction of a head section *IEEE Trans. Nucl. Sci.* **21** 21–43
[22] Rudin L I, Osher S and Fatemi E 1992 Nonlinear total variation based noise removal algorithms *Physica* D **60** 259–68
[23] Chambolle A 2004 An algorithm for total variation minimization and applications *J. Math. Imaging Vis.* **20** 89–97
[24] Osher S, Burger M, Goldfarb D, Xu J and Yin W 2005 An iterative regularization method for total variation-based image restoration *Multiscale Model. Simul.* **4** 460–89
[25] Vogel C R and Oman M E 1996 Iterative methods for total variation denoising *SIAM J. Sci. Comput.* **17** 227–38
[26] Herman G T, Lent A and Rowland S W 1973 ART: mathematics and applications: a report on the mathematical foundations and on the applicability to real data of the algebraic reconstruction techniques *J. Theor. Biol.* **42** 1–32

[27] Cimmino G 1938 Calcolo approssimato per le soluzioni dei sistemi di equazioni lineari *La Ricerca Scientifica II* **9** 326–33
[28] Aharoni R and Censor Y 1989 Block-iterative projection methods for parallel computation of solutions to convex feasibility problems *Linear Algebr. Appl.* **120** 165–75
[29] Hudson H M and Larkin R S 1994 Accelerated image reconstruction using ordered subsets of projection data *IEEE Trans. Med. Imaging* **13** 601–9
[30] Censor Y, Gordon D and Gordon R 2001 BICAV: a block-iterative parallel algorithm for sparse systems with pixel-related weighting *IEEE Trans. Med. Imaging* **20** 1050–60
[31] Censor Y, Elfving T, Herman G T and Nikazad T 2008 On diagonally relaxed orthogonal projection methods *SIAM J. Sci. Comput.* **30** 473–504
[32] Andersen A H and Kak A C 1984 Simultaneous algebraic reconstruction technique (SART): a superior implementation of the ART algorithm *Ultrason. Imaging* **6** 81–94
[33] Censor Y, Elfving T and Herman G 2001 Averaging strings of sequential iterations for convex feasibility problems *Stud. Comput. Math.* **8** 101–13
[34] Penfold S N 2010 Image reconstruction and Monte Carlo simulations in the development of proton computed tomography for applications in proton radiation therapy *PhD Thesis* University of Wollongong, Australia
[35] Combettes P L and Luo J 2002 An adaptive level set method for nondifferentiable constrained image recovery *IEEE Trans. Image Process.* **11** 1295–304
[36] Bichsel H 1972 *Passage of Charged Particles through Matter* (*American Institute of Physics Handbook*) (Berkeley, CA: California University)
[37] Schneider W, Bortfeld T and Schlegel W 2000 Correlation between CT numbers and tissue parameters needed for Monte Carlo simulations of clinical dose distributions *Phys. Med. Biol.* **45** 459
[38] Saito M 2012 Potential of dual-energy subtraction for converting CT numbers to electron density based on a single linear relationship *Med. Phys.* **39** 2021–30
[39] Chvetsov A V and Paige S L 2010 The influence of CT image noise on proton range calculation in radiotherapy planning *Phys. Med. Biol.* **55** N141

Chapter 5

Europium-155 as a source for dual energy cone beam computed tomography in adaptive proton therapy: a simulation study

The following manuscript forms the basis of this chapter.

Zhu, Jiahua, and Scott N. Penfold. "Europium-155 as a source for dual energy cone beam computed tomography in adaptive proton therapy: a simulation study," Medical Physics, submitted.

5.1 Introduction and motivation

The advantages of DECT for dose calculation accuracy in proton therapy have been demonstrated in the previous Chapters. However, to fully utilize the physical potential of proton therapy, dose calculation should be performed on the patient geometry at the time of treatment. Due to effects associated with X-ray scatter and beam hardening, current cone beam CT imaging systems with flat panel detectors do not allow for direct dose calculation.

A novel approach to this task utilizing dual-energy imaging concepts is presented in this Chapter. Monte Carlo simulation of a CBCT system with a radioactive isotope of Europium is used as the radiation source and a pixelated cadmium-zinc-telluride (CZT) material as the detector panel. Reconstructions of a head phantom are presented and accuracy of SPR quantitatively assessed.

5.2 Statement of Contribution

5.2.1 Conception

The idea to use the ^{155}Eu and CZT panel to construct DECBCT modality was first conceptualised by Scott Penfold. The method to model the DECBCT and design a 3D TVS-DROP algorithm to reconstruct CT images was conceptualised by Jiahua Zhu. The comparison of SPR created by different algorithms was conceptualised by all authors.

5.2.2 Realisation

The theory was developed by Jiahua Zhu. Geant4 modelling and GPU-CUDA code were performed by Jiahua Zhu and checked by Scott Penfold.

5.2.3 Documentation

This paper was primarily written by Jiahua Zhu. Editing was performed by all authors.

Statement of Authorship

Title of Paper	Europium-155 as a source for dual energy cone beam computed tomography in adaptive proton therapy: a simulation study
Publication Status	☐ Published ☐ Accepted for Publication ☑ Submitted for Publication ☐ Unpublished and Unsubmitted work written in manuscript style
Publication Details	

Principal Author

Name of Principal Author (Candidate)	Jiahua Zhu
Contribution to the Paper	Modelled a dual energy cone beam CT (DECBCT) system by using ^{155}Eu and CZT panel in Geant4. Made a GPU-CUDA code for image reconstruction algorithm. Calculated the stopping power ratios and compared the results of this novel modality and the traditional CBCT. Wrote the manuscript and acted as correspondent author.
Overall percentage (%)	80%
Certification:	This paper reports on original research I conducted during the period of my Higher Degree by Research candidature and is not subject to any obligations or contractual agreements with a third party that would constrain its inclusion in this thesis. I am the primary author of this paper.
Signature	Date 20/11/16

Co-Author Contributions

By signing the Statement of Authorship, each author certifies that:

i. the candidate's stated contribution to the publication is accurate (as detailed above);
ii. permission is granted for the candidate in include the publication in the thesis; and
iii. the sum of all co-author contributions is equal to 100% less the candidate's stated contribution.

Name of Co-Author	Scott Penfold
Contribution to the Paper	Supervised development of work, help in data analysis and manuscript evaluation
Signature	Date 21/11/16

Name of Co-Author	
Contribution to the Paper	
Signature	Date

Please cut and paste additional co-author panels here as required.

Europium-155 as a source for dual energy cone beam computed tomography in adaptive proton therapy: a simulation study

Jiahua Zhu[1], Scott N. Penfold[1,2]

[1]Department of Physics, University of Adelaide, Adelaide, SA 5005, Australia
[2]Department of Medical Physics, Royal Adelaide Hospital, Adelaide, SA 5000, Australia

Purpose: To investigate the feasibility of a 3D imaging system utilizing a ^{155}Eu source and pixelated cadmium-zinc-telluride (CZT) detector for applications in adaptive radiotherapy. Specifically, to compare the reconstructed stopping power ratio (SPR) values of a head phantom obtained with the proposed imaging technique with a more conventional cone beam computed tomography (CBCT) X-ray source spectrum.

Method: A Geant4 Monte Carlo simulation was performed with the novel imaging system. The simulation was repeated with a typical 120 kV X-ray tube spectrum while maintaining all other parameters. Dual energy ^{155}Eu source CBCT images were reconstructed with an iterative projection algorithm known as total variation superiorization with diagonally relaxed orthogonal projections (TVS-DROP). Single energy 120 kV source CBCT images were reconstructed with a Feldkamp-Davis-Kress implementation of the filtered backprojection (FDK-FBP) reconstruction algorithm as well as TVS-DROP. Reconstructed images were converted to SPR with stoichiometric calibration techniques based on ICRU 44 tissues. Quantitative accuracy of reconstructed attenuation coefficient images as well as SPR images were compared.

Results: Images generated by gamma emissions of ^{155}Eu showed superior contrast resolution to those generated by the 120 kV spectrum. Quantitatively, all reconstructed images correlated with reference

attenuation coefficients of the head phantom within 1 standard deviation. Mean values were closer to reference values with the ^{155}Eu source which also showed a smaller standard deviation of pixel values. Use of a dual energy conversion to SPR resulted in superior SPR accuracy with the ^{155}Eu.

Conclusion: ^{155}Eu was found to display desirable qualities when used as a source for dual energy CBCT. Further work is required to demonstrate whether the simulation results presented here can be translated into an experimental prototype.

Keywords

Europium-155, dual energy cone beam computed tomography, adaptive proton therapy, pixelated cadmium-zinc-telluride detectors.

1. Introduction

Proton therapy is a highly conformal form of external beam radiotherapy. To fully exploit the physical advantages of proton therapy, the geometry and stopping power ratio (SPR) of patient tissues at the time of treatment should be known with a high degree of accuracy. Cone beam computed tomography (CBCT) is a popular tool for obtaining three dimensional geometrical information at the time of treatment in X-ray therapy. In more advanced treatment workflows, CBCT can also be used as a tool for dose accumulation studies and offline adaptive radiotherapy[1,2]. Despite the widespread use of CBCT in conventional X-ray radiotherapy, this technology is only now becoming a standard offering of proton therapy vendors. The most effective utilization of CBCT in a clinical proton therapy environment is a topic receiving increasing interest[3-6].

Due to the dependence of CBCT Hounsfield units (HUs) on the particular scatter environment created by the patient, CBCT image data are not typically used directly for dose calculation[7,8]. Rather, CBCT images are typically only used for geometrical information in online use. In offline adaptive radiotherapy, however, the original planning CT may be registered to the CBCT geometry with rigid or deformable image registration algorithms and dose calculation performed on this data set. This allows for dose accumulation studies and assessment of the need for replanning during the course of treatment. While this undoubtedly a step in the right direction, a CBCT system capable of producing reliable HUs would allow for efficient *online* adaptive radiotherapy.

Furthermore, a number of recent studies have examined the potential advantages of dual energy CT (DECT) for proton therapy dose calculation[9-11]. Various DECT scanning approaches have been proposed, however the most common scenario consists of imaging with two differing X-ray spectra emanating from an X-ray tube. The resulting reconstructed images can be processed to produce images of electron density and effective atomic number[9-11]. The effective atomic number data can be correlated with mean

excitation energy, allowing for a calculation of stopping power[9]. This approach has been shown to result in superior dose calculation accuracy for proton therapy in certain cases when compared to the standard approach based on single energy CT and an empirically derived conversion of HU to SPR[9,11].

Despite the promising results obtained thus far with DECT for proton therapy, a number of technical and logistical issues need to be addressed. Firstly, beam hardening of the polyenergetic bremsstrahlung spectra emitted from X-ray tubes means that a given tissue does not possess a unique effective atomic number, as determined from DECT. Rather, the effective atomic number is dependent on the spectral composition at the point of the tissue, which will be differ at different projection angles. This results in a lack of data fidelity. Furthermore, truly coincident imaging with dual-energy spectra is not possible. The acquired data is either temporally separated in the case of kV switching of a single tube, or sequential scanning at different tube potentials, or spatially separated in the case dual tubes operating at different angles simultaneously.

In the current work a dual energy CBCT (DECBCT) system making use of Europium-155 (^{155}Eu) and a pixelated detector capable of energy discrimination is proposed to meet the needs for accurate online dose calculation in proton therapy. A description of the favorable characteristics of ^{155}Eu for this purpose is presented. A Monte Carlo simulation of a CBCT acquisition of a head phantom with ^{155}Eu and a pixelated cadmium-zinc-telluride (CZT) detector was conducted. The resulting reconstruction of SPR was compared to a corresponding simulation with a 120 kV bremsstrahlung spectrum simulating a conventional CBCT system.

2. Methods

2.1. Characteristics of ^{155}Eu

^{155}Eu was first investigated as a potential source for mobile X-ray imaging by Stewart[12] in the 1950s. The primary properties that make ^{155}Eu an attractive source for dual-energy imaging are; a half-life that is not excessively long so as to be a serious radiation waste concern, while long enough to ensure reasonable periods between source replacement; two dominant gamma emissions between 50 and 150 keV to eliminate beam hardening; a high specific activity allowing for a high activity in a small volume; and an observationally stable daughter isotope. These characteristics are summarized in Table 1 with γ emissions summarized in Table 2.

^{155}Eu can be produced through neutron irradiation of enriched ^{154}Sm. The (n,γ) reaction channel produces ^{155}Sm which subsequently decays through β^- decay with a 22 minute half-life[13]. A drawback of this reaction channel is the simultaneous production of ^{154}Eu through the (n,γ) reaction of ^{153}Eu which may be produced by neutron irradiation of contaminant ^{152}Sm. The ratio of ^{154}Eu:^{155}Eu can be minimized by high purity ^{154}Sm, a short irradiation time and frequent target reprocessing to remove stable ^{153}Eu. The authors of the paper[13] suggest that enriched ^{154}Sm containing 98.5% ^{154}Sm and 1.25% ^{152}Sm irradiated at 2×10^{14} neutrons/cm^2/s for 2 days should yield 0.17 Ci of ^{155}Eu per gram of samarium. The ratio of ^{154}Eu: ^{155}Eu would be $3 - 8 \times 10^{-4}$ Ci/Ci.

Table 1. Characteristics of ^{155}Eu[14].

Characteristic	Value
Half-life	4.753 yr
Decay mode	β^- (100%)
Q-value	252.1 keV
Molar mass	154.92 g/mol
Specific activity	1.79×10^{13} Bq/g
Daughter nucleus	^{155}Gd

Table 2. γ energies of ^{155}Eu[14] Probabilities correspond to gammas per decay. Energies utilized in the proposed imaging are shown in bold.

Energy (keV)	Probability (%)
12.7	0.01
13.8	0.02
18.8	0.05
24.6	0.01
26.5	0.32
31.4	0.01
40.8	0.03
45.3	1.33
58.0	0.07
60.0	1.13
86.1	0.15
86.5	**30.70**
105.3	**21.15**
146.1	0.05

When imaging with a radioactive source, one must consider the volume of the source required to acquire images in a realistic timeframe. The following calculation was performed to determine an approximate source size required for image acquisition with dual energies at 86.5 keV and 105.3 keV. If too large a source size is required, spatial resolution may be compromised.

Firstly, the counts of each gamma energy per pixel required to maintain a σ = 2% uncertainty due to Poisson counting statistics was calculated with Eq. (1).

$$N = \sigma^{-2} \tag{1}$$

The detector was assumed to be 500 mm from imaging isocentre (ADD) with a pixel size of 1 mm (*d*) and a total area of 500 × 500 mm^2 (side length of *l* = 500 mm). If the source is 1000 mm from isocentre (SAD), this pixel size equates to 0.67 mm at the isocentre plane, with a 333 mm field of view. The fractional area (*a*) of a single pixel at the edge of the detector in the 4π geometry surrounding the source was approximated with Eq. (2).

$$a = \frac{d^2}{4\pi((SAD+ADD)^2+(l/2)^2)} \quad (2)$$

A rotation speed of 1 revolution per minute was assumed with angular binning of 2 degrees. This equates to an acquisition time of t_p = 0.33 s per projection. The activity *A* required to deliver *N* counts of each gamma energy per pixel per projection angle after traversing a 200 mm thick water phantom was calculated with Eq. (3).

$$A = \frac{N}{exp(-\mu_w(E)D)} \frac{f(E)}{a} \frac{1}{t_p} \quad (3)$$

Where, μ_w is the attenuation coefficient of water at gamma energy *E*, *D* is the thickness of a water phantom, here estimated to be 200 mm, and *f*(*E*) is the fraction of gammas of energy *E* emitted per decay of ^{155}Eu. The specific activity of a pure sample of ^{155}Eu was calculated with Eq. (4)

$$s = \frac{N_A \ln 2}{t_{1/2} M_A} \quad (4)$$

Using Eq.'s (3) and (4), the mass of ^{155}Eu required is

$$m = A/s \quad (5)$$

Using the values defined in the text and Table 1, a spherical source of diameter 4.0 mm and 4.2 mm were required for the 86. 5 keV and 105.3 keV gammas respectively. In the following Geant4 Monte Carlo simulations, a conservative spherical source of 5.0 mm diameter was used. Assuming 100% ^{155}Eu purity, this corresponds to an activity of 6.15 × 10^{12} Bq.

2.2. Monte Carlo simulation

The Geant4 Monte Carlo toolkit[15] was used to model the DECBCT system with the geometry and materials outlined above. All simulations were performed with Geant4 version 10.0.0.p03 with the EmStandard_Opt4 electromagnetic physics processes enabled. This physics constructor makes use of the Evaluated Photon Data Library 1997[16].

2.2.1. Source spectra

To include the effects of source self-attenuation, a preliminary simulation with a 5.0 mm diameter source of ^{155}Eu material surrounded by an air sensitive detector shell was conducted. The Geant4 General Particle Source (GPS) was used with ^{155}Eu ions of zero kinetic energy to generate primary events. These primaries decayed with the Geant4 Radioactive Decay version 4.0 dataset. All emissions exiting the ^{155}Eu source were collected by the sensitive detector. A plot of collected emissions with and without source attenuation are shown in Fig. 1. The collected photon emissions with source attenuation were used as a phase-space file for further imaging simulations. Electrons were not included in imaging simulations as they significantly slow processing and would be attenuated in air before reaching the imaged object.

The source for subsequent simulations was modelled as a 5.0 mm diameter sphere of air. A histogram of 1 keV bin width containing the photon energy distribution collected in the ^{155}Eu source simulation was used with Geant4 GPS. All primary particles were now photons. The primary photons were restricted to a conical initial direction covering the detector panel. To shape the conical emission to the panel area, a lead collimator was placed in the Geant4 geometry to form a pyramid shaped primary beam, matching the detector area.

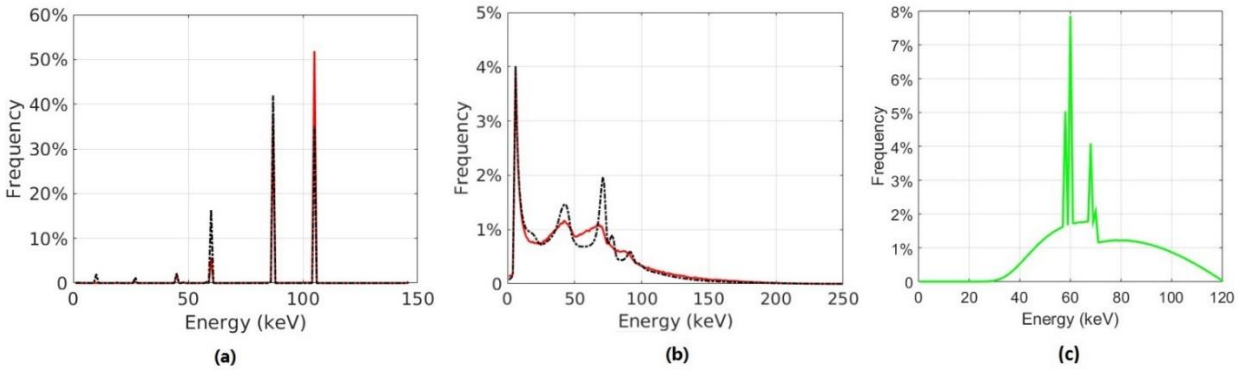

Figure 1. ^{155}Eu spectra generated by Geant4 with (red) and without (black) source self-attenuation. (a) Photon energy spectrum, (b) electron energy spectrum. (c) 120 kV bremsstrahlung spectrum used for polyenergetic X-ray tube comparison.

2.2.2. Phantom

A head phantom with a geometry suggested by Herman[17] was placed at the centre of rotation of the imaging system. The phantom simulated a human head structure with skull, brain and four types of soft tissue materials. The chemical compositions and densities of the tissues are shown in Table 3. A cross-section of the phantom is shown in Fig. 2. The outer dimensions of the head phantom were 17.3 cm × 12.9 cm. The Geant4 simulation geometry is shown in Fig. 2(b).

Table 3. Elemental fractions by weight and density of 6 tissues included in the head phantom.

Tissue	H	C	N	O	P	Na	S	Cl	K	Density (g/cm^3)
Cranium[18]	0.005	0.212	0.040	0.435	0.002	0.081	0.003	0.176	0.001	1.610
Brain[18]	0.107	0.145	0.022	0.712	0.004	0.002	0.002	0.003	0.003	1.035
Cerebrospinal fluid (CSF)	0.112	0	0	0.888	0	0	0	0	0	0.900
Haematoma	0.107	0.145	0.022	0.712	0.004	0.002	0.002	0.003	0.003	1.050
Carcinoma	0.107	0.145	0.022	0.712	0.004	0.002	0.002	0.003	0.003	1.200
Meningoma	0.107	0.145	0.022	0.712	0.004	0.002	0.002	0.003	0.003	1.150

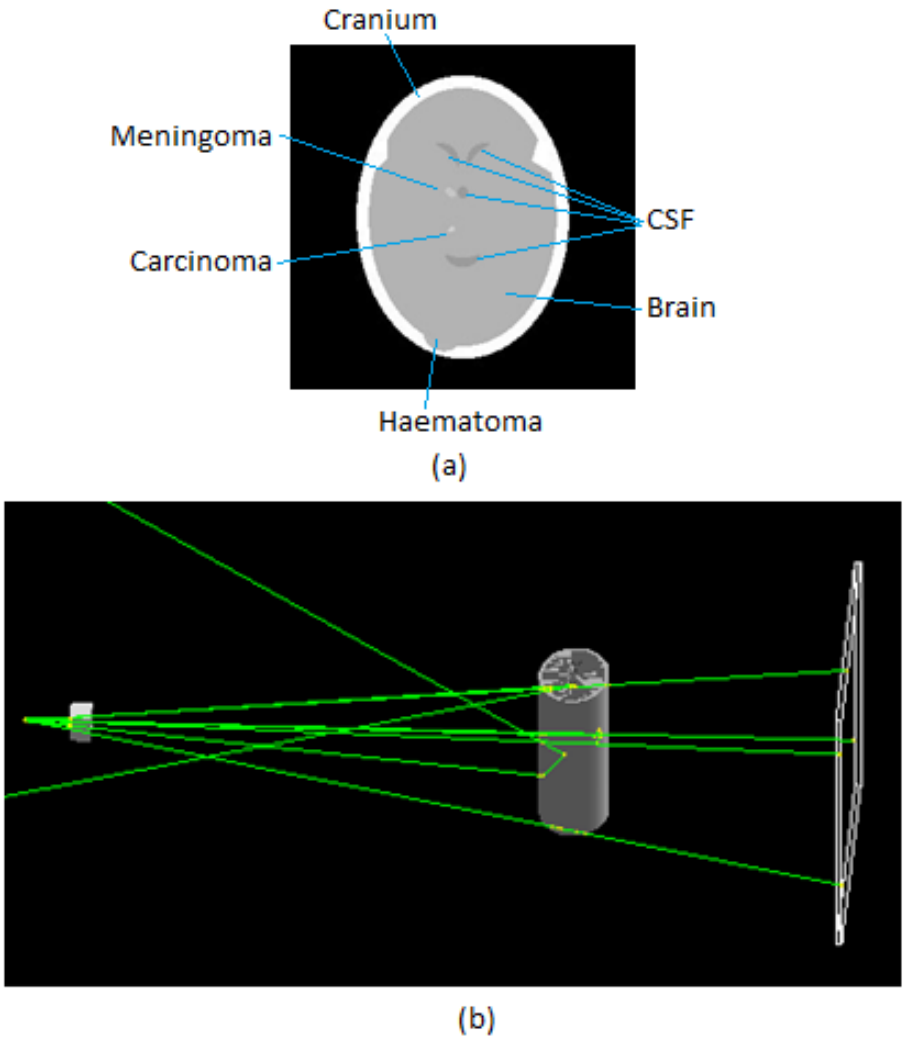

Figure 2. (a) Cross-section of the head phantom used in the imaging simulations. The white region represents cranial bone, the main inner region represents brain tissue. All dark grey regions are CSF, the upper small ellipse is a meningioma and the lower small ellipse is a carcinoma. (b) Simulation geometry in Geant4. Primary photons are emitted from the source volume on the left, pass through a lead collimator, interact or traverse the cylindrical phantom, and are incident on the pixelated detector panel.

2.2.3. Pixelated detector

Current flat panel imaging systems are often composed of a scintillating material bonded to an amorphous silicon (aSi) thin film transistor (TFT) array. The high atomic number scintillating material is used to improve the photon detection efficiency of the device. The readout of these systems is typically

not spectroscopic, but rather energy integrating. Pixelated direct detection semiconductors, and cadmium-zinc-telluride (CZT) detectors in particular, are experiencing growing interest from the medical imaging community. The high atomic number and suitability for room temperature operation of these devices make them ideal for spectroscopy in the energy range of the ^{155}Eu emissions. A comparison of imaging efficiency with a conventional flat panel consisting of CsI bonded to aSi and CZT panels has been performed by Le *et al*.[19].

A pixelated CZT detector panel was simulated in the Geant4 imaging simulations. The panel was 10 mm thick with 1 mm pixel sizes and a total area of 500 × 500 mm^2. The panel was positioned 500 mm from the centre of rotation of the imaging system. The panel was simulated as a solid slab of cadmium-zinc-telluride with a density of 5.8 g/cm^3. Photon interactions in the detector panel were considered, including fluorescence. Energy deposited in each pixel was recorded and tallied in 1 keV bin widths. Therefore, the output of each simulation was an energy spectrum acquired in each detector pixel.

2.2.4. Conventional cone beam CT simulation

To compare the proposed imaging system with a more conventional CBCT system, the ^{155}Eu source spectrum was replaced by a typical 120 kV tungsten target X-ray tube spectrum. The geometry and detector material was left as in the ^{155}Eu simulation, however, all energy depositions were integrated so as to produce a single output value per pixel. Although conventional CBCT systems make use of aSi detector materials, the objective of this simulation was to highlight the differences in reconstructed images due to the use of the different source spectra.

2.3. Image reconstruction

The advantage of reconstructing DECT images for proton therapy dose calculation with an iterative algorithm known as total-variation superiorization with diagonally relaxed orthogonal projections (TVS-DROP) when compared to the traditional filtered backprojection (FBP) has been presented in previous

work[20]. The TVS-DROP algorithm (referred to as TVS1-DROP* by Penfold *et al*.[21]) was once again used in the current work to reconstruct the 86.5 keV and 105.3 keV data. For details on the algorithmic implementation of TVS-DROP, the reader is referred to Zhu and Penfold[20].

Before starting the iterative reconstruction, data processing of the measured energy spectra from each pixel was required. A simulation of 10^{11} primary photons without the phantom in place was used to acquire an I_0 scan. To correct for panel Compton scattered 105.3 keV photons contributing to counts in the 86.5 keV channel, a linear fit to counts in the neighboring 3 energy bins larger than 86.5 keV were backprojected to the 86.5 keV bin. The backprojected counts were subtracted from the total 86.5 keV counts. To reduce noise in individual pixel energy spectra, the scatter correction was performed for each pixel by averaging the pixel spectra of the neighboring 3×3 pixels.

With the phantom at the centre of rotation of the imaging system, 180 simulations were performed with 10^{11} primary photons per projection angle with an angle spacing of 2 degree. A consistent number of primary photons and projection angles were used in the 120 kV simulations. Air KERMA in air values of (9.9 ± 0.6) μGy and (9.6 ± 0.7) μGy in a 20 mm diameter sphere of air at isocenter were determined from Geant4 simulations for the ^{155}Eu and bremsstrahlung spectrum, respectively. The scatter correction processing as described above was performed for all projection angles for the Eu^{155} simulations.

2.4. SPR calculation by DECBCT images

The advantage of DECT imaging for proton therapy dose calculation has been investigated by several authors[7,8]. The advantage lies in the ability to calculate the SPR of tissues in a more direct manner than with SECT. With DECT, the two attenuation coefficient images produced by image reconstruction may be processed to provide two separate images quantifying electron density and effective atomic number (Z_{eff})[22-24]. After converting Z_{eff} to mean excitation energy with the method proposed by Yang *et al.*[9], the SPR of a pixel can be calculated with Eq. (6).

$$SPR = \hat{\rho}_e \ln[\frac{2m_e c^2 \beta^2}{I_m(Z_{eff})\,(1-\beta^2)} - \beta^2] \,/\, \ln[\frac{2m_e c^2 \beta^2}{I_{water}(1-\beta^2)} - \beta^2] \quad (6)$$

here $\hat{\rho}_e$ is the electron density of the material relative to that of water, m_e is the rest electron mass, c is the speed of light in vacuum, β is the speed of the proton relative to the speed of light and $I_m(Z_{eff})$ and I_{water} are the mean excitation energies of the material and water respectively.

The Z_{eff} obtained by DECT was defined in the following manner. Let the attenuation coefficient of an element of atomic number Z at energy E be written as

$$\mu(E) = \rho_e \; {}_e\sigma(Z, E), \quad (7)$$

where ρ_e is the electron density and ${}_e\sigma$ is the total electronic cross-section. If we have two fixed photon energies and take the ratio of the attenuation coefficients, the energy independent electron density is cancelled and we are left with a function of atomic number only as shown in Eq. (8).

$$\frac{\mu_{E_1}}{\mu_{E_2}} = \frac{{}_e\sigma(Z,E_1)}{{}_e\sigma(Z,E_2)} = g(Z) \quad (8)$$

As the ratio of attenuation coefficients can be measured and the atomic number is unknown, we require the inverse of this function, i.e.

$$Z_{eff} = g^{-1}\left({}^{\mu_{E_1}}/_{\mu_{E_2}}\right) = f({}^{\mu_{86.5}}/_{\mu_{105.3}}) \quad (9)$$

Attenuation coefficients for 86.5 keV and 105.3 keV were obtained from NIST XCOM for atomic numbers 6 – 15. Z was plotted as a function of the resulting ratio. A fourth degree polynomial function was fit to this data to provide the function f of Eq. (9) (see Fig. 3.). This function was applied to the ratio of each reconstructed pixel value of the DECBCT simulations.

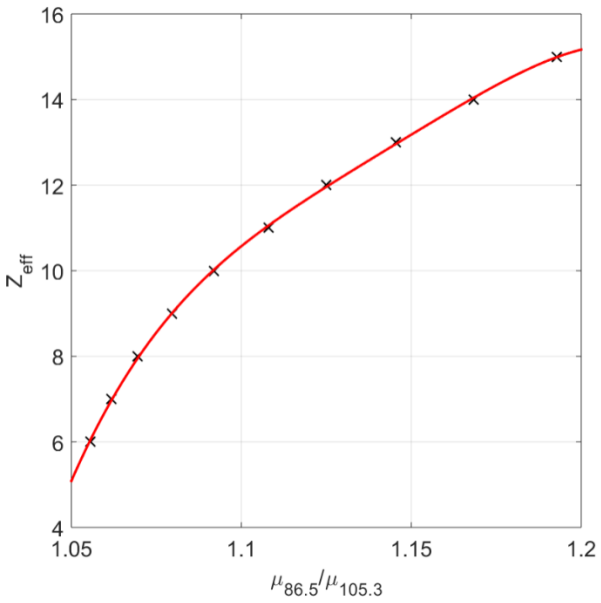

Figure 3. Relationship between atomic number and ratio of attenuation coefficients at 86.5 keV and 105.3 keV. NIST XCOM data points are shown in black and the fourth degree polynomial fit to the data shown in red.

A stoichiometric calibration of the natural logarithm of mean excitation energy as a function of Z_{eff} was performed as described in Yang *et al.* [9] and Zhu and Penfold[11]. In this process, the chemical composition and density of ICRU 44 tissues were used to calculate mean excitation energies with Eq. (10) and Z_{eff} with Eq. (9).

$$\ln I_m = \frac{\sum \frac{\omega_i Z_i}{A_i} \times \ln I_i}{\sum \frac{\omega_i Z_i}{A_i}} \tag{10}$$

Here ω_i is the weight of element i in a given tissue, Z is the atomic number and A is atomic weight. I_i represents the mean excitation energy of element i. The relationship between Z_{eff} and ln I_m was approximated with a piecewise linear fit to the data, as described in Zhu and Penfold[11].

2.5. Analysis of SPR

2.5.1. Reference SPR calculation

To compare the accuracy of SPR calculated by DECBCT with that derived from CBCT, a reference SPR image was required. This image was obtained by applying Eq. (6) to all pixels with the chemical compositions and densities of tissues presented in Table 2. Here, the electron density was calculated with Eq. (11)[25].

$$\rho_e = \rho N_g / \rho^w N_g^w \tag{11}$$

Where ρ is the density of tissue, N_g is the number of electrons per unit volume in the tissue, ρ^w is the density of water, and N_g^w denotes the number of electrons per unit volume in water.

The mean excitation energy, I, of the tissues was calculated with Eq. (10) and the proton kinetic energy set to 219 MeV, as in Yang *et al.*[9].

2.5.2. SPR with conventional CBCT

Schneider *et al*.[25] suggested the use of a stoichiometric calibration to transfer X-ray CT images to SPR values for proton therapy dose calculation. This process was applied for the 120 kV spectra and ICRU 44 tissues used in the current work. It is equivalent to the calibration of ln I_m as a function of Z_{eff} described above, however, SPR replaces ln I_m and the attenuation coefficient replaces Z_{eff}. SPR was calculated with Eq. (6) using the method outlined in Section 2.5.1 but with ICRU 44 tissues instead of the phantom tissues. The attenuation coefficients for ICRU 44 tissues with the 120 kV spectra were obtained from NIST XCOM[26]. Fig. 4 illustrates the stoichiometric calibrations for DECT and SECT.

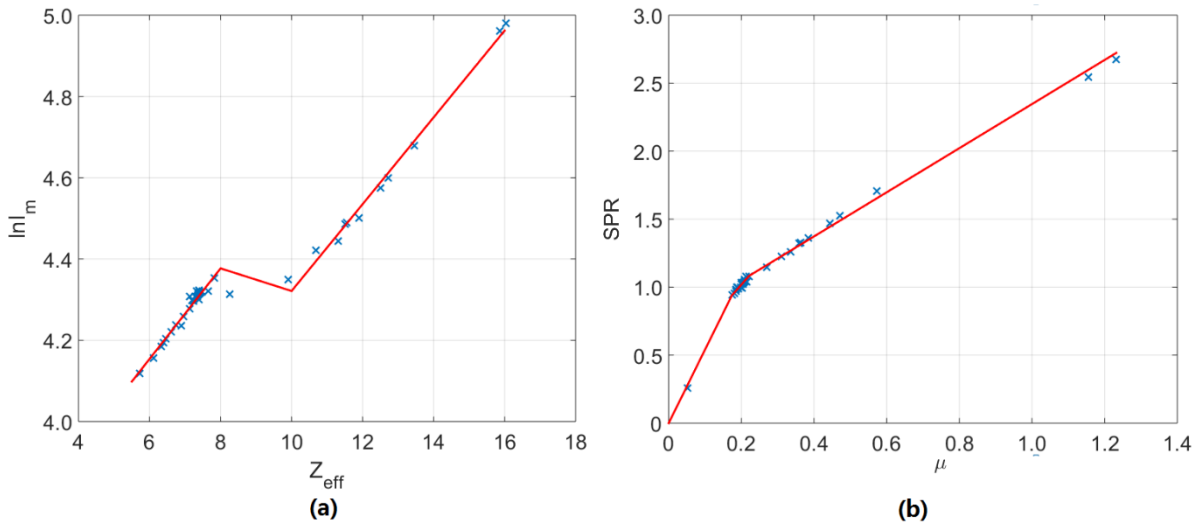

Figure 4. Stoichiometric calibration functions for (a) DECT and (b) SECT. Crosses correspond to data points calculated for ICRU 44 tissues, lines represent a piecewise linear fit to the data.

3. Results

3.1. Acquired energy spectra

An example of the energy spectrum collected by a single pixel, located in the central region of the panel, is shown in Fig. 5. In addition to the original 86.5 keV and 105.3 keV peaks, several other peaks are now present. The origin of these peaks are summarized in Table 4. The peaks are caused by characteristic X-rays originating in the pixel of photoelectric interaction being detected in a neighboring pixel. As a result, a peak is seen in energy bins corresponding to the energy of the characteristic X-ray, and also the energy bin corresponding to the difference between the original photon energy and the characteristic X-ray energy. In the future these peaks may be included in the counts for the respective photon peaks, but due to the difficulty with subtracting the scatter background from these energy bins, they were not utilized in the current work.

As discussed in Section 2.3, a small contribution from Compton scattered 105.3 keV photons can be seen to contribute to counts in the 86.5 keV peak. By comparing the relative height of the peak to the

background from acquisitions with and without the phantom, it was determined that the majority of the Compton scattered photons originate from interactions in the panel, rather than interactions in the phantom.

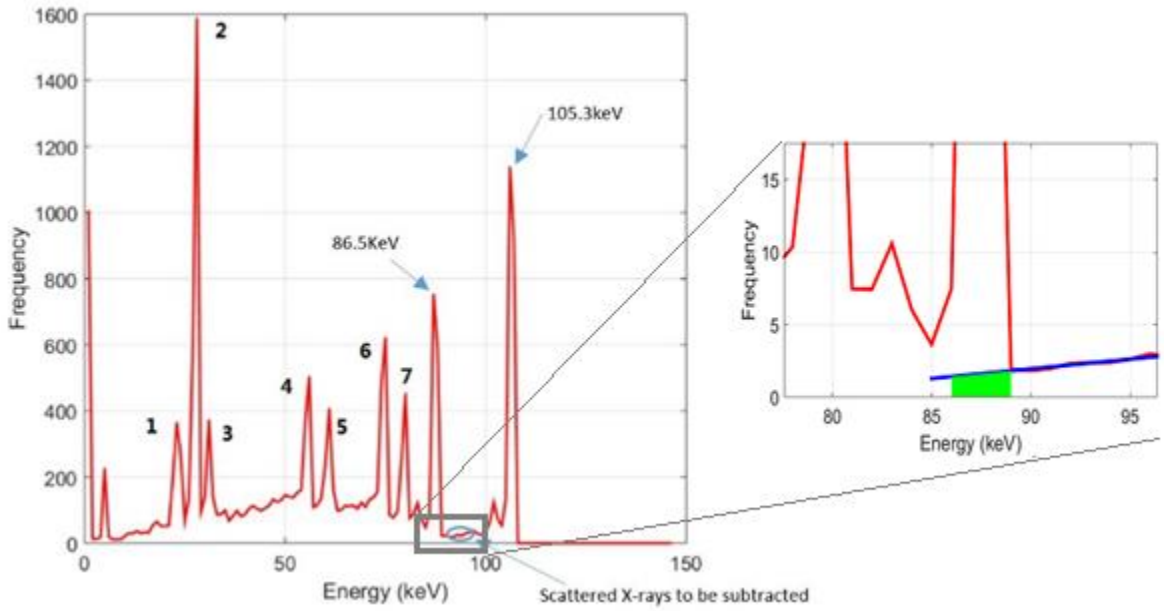

Figure 5. Example energy spectra acquired in a single pixel of the CZT detector. The insert contains a zoomed image illustrating how 105.5 keV scattered X-rays were subtracted from the 86.5 keV photopeak. The blue line is a straight line fit to the three bins immediately larger than the 86.5 keV bin and the green region is the subtracted scattered photon contribution.

Table 4. Origin of dominant peaks appearing in detected spectra not present in source spectrum.

ID	Energy bin (keV)	Origin
1	23	Cd K_α (23.2 keV)
2	27	Te K_α (27.5 keV)
3	31	Te K_β (31.0 keV)
4	55	86.5 keV - Te K_β
5	60	86.5 keV - Te K_α
6	73	105.3 keV - Te K_β
7	78	105.3 keV - Te K_α

3.2. Reconstructed CBCT images

Attenuation coefficient images for the 86.5 keV and 105.3 keV peaks reconstructed with TVS-DROP are shown in Fig. 6 (a) and (b). Also shown are images reconstructed with FBP and TVS-DROP using data acquired with the 120 kV source spectrum in Fig. 6 (c) and (d). As the attenuation coefficients are different for each image, custom window settings were used. The lower window level was set to half the reference value for brain tissue, and the upper level set to 1.1 times the expected value for the bone.

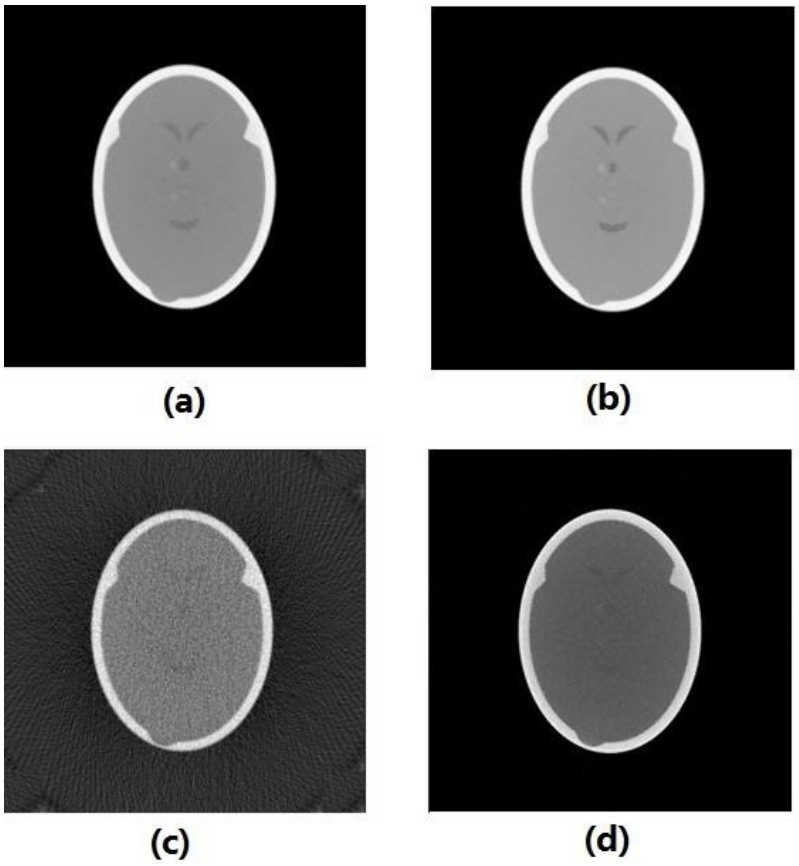

Figure 6. A slice of the 3D reconstructed images for (a) 86.5 keV, (b) 105.3 keV, (c) 120 kV spectrum reconstructed with the FDK-FBP algorithm, and (d) 120 kV spectrum reconstructed with the TVS-DROP algorithm.

Table 5. Summary of reconstructed pixel values for the cranium and brain regions of the images shown in Fig. 4. Simulated values correspond to mean pixel values ± 1 standard deviation over a region of

interest. Reference values at 120 kV were calculated with 10 cm water filtration applied to the incident spectrum to account for beam hardening in the phantom.

		86.5 keV with TVS-DROP	105.3 keV with TVS-DROP	120 kV with FDK-FBP	120 kV with TVS-DROP
Cranium	Simulated	0.315 ± 0.008	0.279 ± 0.005	0.435 ± 0.042	0.475 ± 0.034
	Reference	0.320	0.280	0.482	
	% diff.	*-1.56%*	*-0.36%*	*-9.75%*	*-1.47%*
Brain	Simulated	0.181 ± 0.003	0.175 ± 0.002	0.197 ± 0.032	0.212 ± 0.007
	Reference	0.184	0.173	0.210	
	% diff.	*-1.63%*	*1.16%*	*-6.19%*	*-0.95%*

The noise reduction and associated superiority in contrast resolution when using monoenergetic imaging and the TVS-DROP algorithm are evident. A summary of the reconstructed values for the cranium and brain regions of the images shown in Fig. 6 is presented in Table 5. With the exception of the FDK-FBP reconstruction of the 120 kV spectrum, all measured values agree with reference values within one standard deviation. The greatest difference can be seen in the standard deviation values, indicating differing degrees of noise in the images.

3.3. SPR accuracy with DECBCT and CBCT approaches

Images obtained following conversion of the DECBCT and 120 kV CBCT images to SPR are shown in Fig. 7 and compared to the reference image. Since the conversion of the 120 kV images is obtained by a simple mapping with a linear function, the images do not appear different to those shown in Fig. 6. However, the conversion of the DECBCT images to SPR requires a ratio of the two images and as such the noise in the resulting image is amplified when compared to the two original images. Even so, superior contrast resolution is still evident when using the ^{155}Eu spectrum.

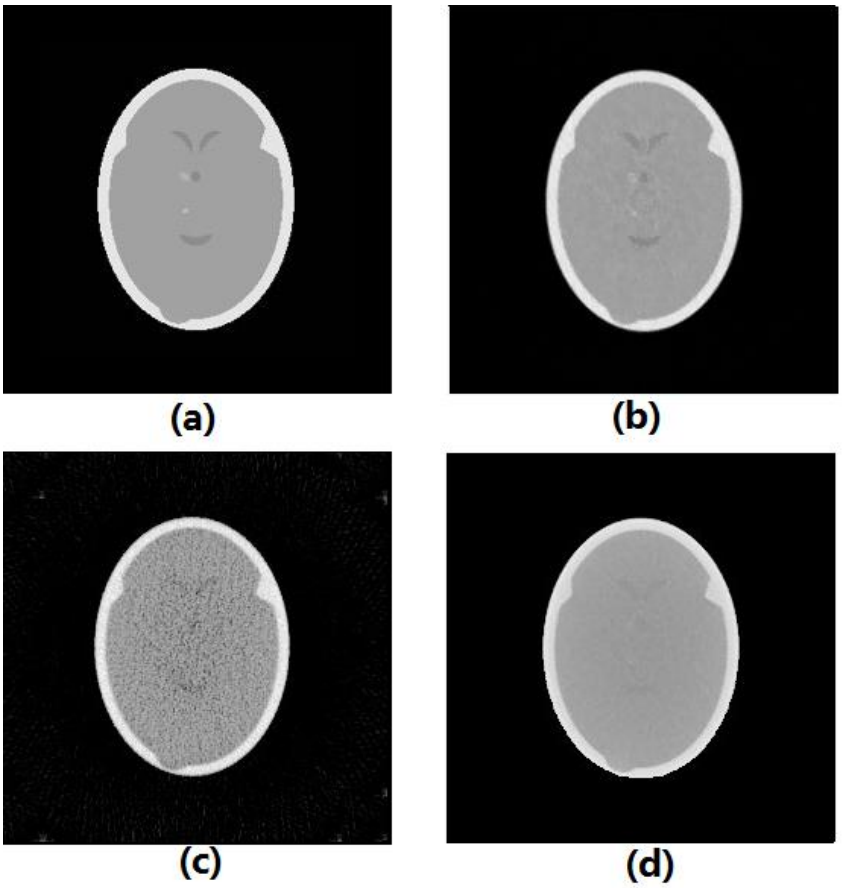

Figure 7. (a) Reference SPR image. Reconstructed SPR images using (b) the DECBCT approach, (c) the 120 kV CBCT image reconstructed with FDK-FBP, and (d) using the 120 kV CBCT image reconstructed with TVS-DROP.

To compare the quantitative accuracy of the SPR images, a histogram of pixel values was generated for each reconstructed image, as well as the reference SPR image. The histogram is shown in Fig. 8. The pixelwise relative difference with respect to the reference phantom was also calculated and the frequency historgram of the error maps are shown in Fig 9. Comparing the location of peak values and width of the peaks of Fig. 8 demonstrates the superior accuracy and precision, respectively, of the ^{155}Eu DECBCT SPR image. This is further supported by the relative error plots shown in Fig. 9. A comparison of the cranium and brain values for the three reconstructed images is provided in Table 6. SPR accuracy

within 1% was obtained when using ^{155}Eu DECBCT. The accuracy was reduced for the conventional CBCT approaches.

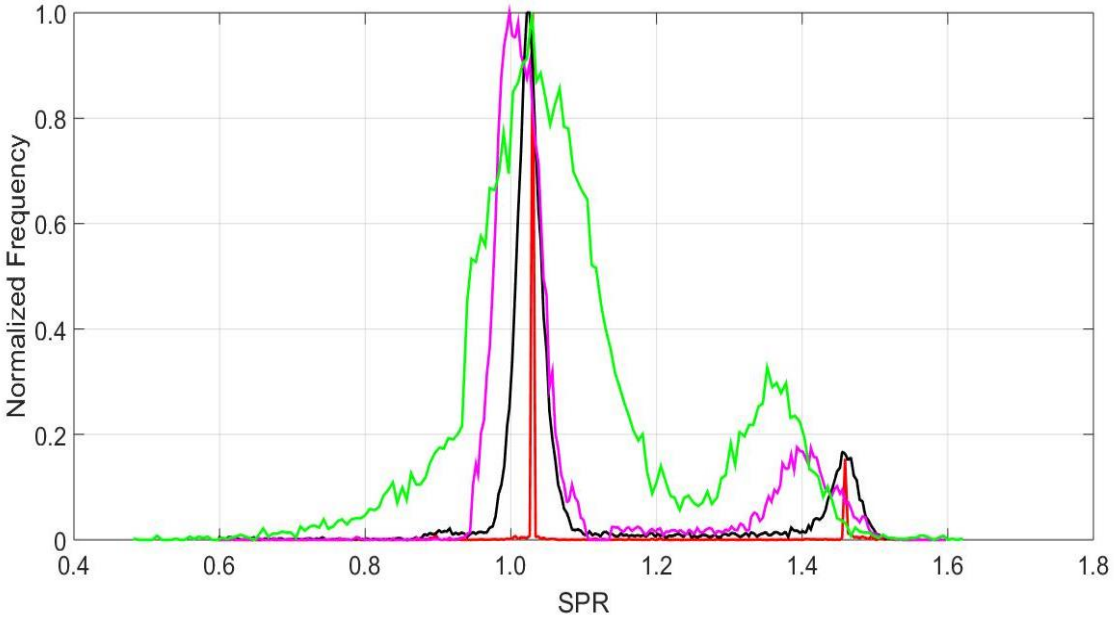

Figure 8. Histogram of SPR images. Reference (red), DECBCT (black), FDK-FBP 120 kV (green) and TVS-DROP 120 kV (pink).

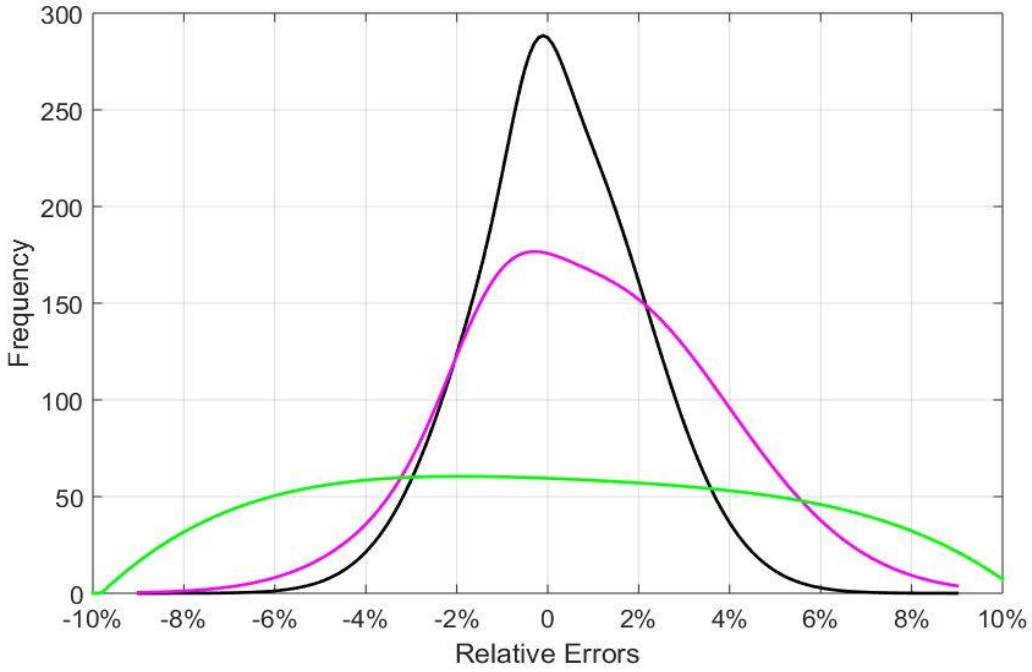

Figure 9. Frequency histogram of pixel-wise relative errors in the reconstructed images shown in Fig. 7. DECBCT (black), FDK-FBP 120 kV (green) and TVS-DROP 120 kV (pink).

Table 6. The SPR comparisons for different algorithms.

Tissue	Reference SPR	^{155}Eu DECBCT	% diff.	120 kV with FDK-FBP	% diff.	120 kV with TVS-DROP	% diff.
Cranium	1.463	1.455 ± 0.024	-0.55%	1.360± 0.046	-7.04%	1.406 ± 0.042	-3.90%
Brain	1.031	1.022 ± 0.017	0.87%	1.042 ± 0.088	1.07%	1.013 ± 0.020	-1.75%

4. Discussion

As schemes for online adaptive radiotherapy continue to evolve, the need for quantitatively accurate 3D imaging immediately prior to treatment increases. This is particularly true for proton therapy due to the sensitivity of Bragg peak positioning upon estimated tissue SPR. For this purpose, a DECBCT imaging system based on ^{155}Eu and a CZT detector panel has been proposed in the current work. The potential

advantages in terms of SPR accuracy for online adaptive proton therapy dose calculation have been presented.

Calculations showed that a source diameter of approximately 5 mm would be required to allow imaging with 1 revolution per minute while ensuring sufficient counts per pixel for 2% Poisson counting uncertainty for a 1 mm^2 pixel size. Reconstructed images did not show significant degradation of spatial resolution with this large source size, however further work is required to quantify the effect this may have on dose calculation accuracy for adaptive radiotherapy. By modifying the parameters discussed in Section 2.1 it was found that doubling the pixel size reduced the required source diameter by 30% while allowing for 5% counting uncertainty allowed for a reduction of source diameter of approximately 50%. Increasing the acquisition time has the smallest effect on required source size. The calculations also assumed 100% purity of the ^{155}Eu source. The fraction of ^{155}Eu nuclei in the source will be less than 1 in reality and decrease over time. It is envisaged that source decay would be accounted for in the rotation speed of the imaging system.

Quantitatively accurate reconstructions of attenuation coefficients for both gamma emissions were presented. Superior contrast resolution due the absence of beam hardening and Compton scatter removal was demonstrated when compared to images generated with conventional 120 kV bremsstrahlung spectra. A method for conversion of the monoenergetic attenuation coefficient images to SPR was presented. Reconstructed SPR values were within 1% of the reference values calculated from the known chemical composition and density of the materials used in the Geant4 simulation. This was compared to errors of 6.6% and 3.9% for cranium SPR when using a 120 kV source spectrum. A quantitative comparison of spatial resolution and contrast resolution will be conducted in future work with appropriate phantoms.

A head phantom was used to demonstrate the concept in the current work. Further work is required to demonstrate the functionality of the proposed imaging concept with larger treatment sites such as the abdomen and thorax. These sites typically make use of bow-tie filters to reduce the range of X-ray fluence at the detector panel. Furthermore, conventional X-ray tubes allow for an increase in mAs to compensate for the extra attenuation experienced when traversing the body. The only corresponding control mechanism in the proposed ^{155}Eu imaging system is a longer acquisition time. This may be achieved by a variable rotation speed, accounting for variable patient thicknesses.

The limited count-rate of ^{155}Eu imaging is advantageous, however, when considering the need to avoid count pile-up in the solid state detector panel. While the critical time to avoid pile-up in the detector is heavily dependent on design and construction, one can expect to avoid significant pile-up contribution with count rates of 1 MHz or less[27]. Indeed, one manufacturer quotes pixelated detector capabilities of 10^7 photons/s/pixel. For the proposed imaging concept, it is envisaged that maximum count rates on the order of $10^4 – 10^5$ photons/s/pixel would be experienced outside the imaged object. Pile-up is therefore not thought to be a limiting factor. Furthermore, the detector simulated in the current work was 10 mm thick, which is larger than pixelated systems currently available on the market. Due to the large atomic number and thus high photoelectric cross-section, reducing the thickness to 2 mm reduces the photoelectric absorption in the detector by only 0.3% at 105.3 keV. Further simulation and experimental work is required to optimize the system design, however, it is not anticipated that detector thickness will significantly affect the detection efficiency at 105.3 keV.

Advances in conventional CBCT are still taking place and need to be considered in future comparisons with ^{155}Eu-based imaging. In particular, dual-energy CBCT systems and detectors with antiscatter grids are currently being investigated. Dual energy cone beam CT with conventional flat panel detectors and X-ray tubes have being explored for image guided radiotherapy[28]. These systems are in a prototype stage and as such comparisons with our approach are not yet feasible. CBCT systems with antiscatter

grids have been investigated by Schafer *et. al*[29]. It was determined that although the antiscatter grid could improve HU accuracy, CNR was compromised and thus the authors did support the use of antiscatter grids for CBCT.

5. Conclusion

A novel dual energy cone beam CT system consisting of a ^{155}Eu source and a pixelated CZT detector panel for applications in adaptive proton therapy has been presented. A realistic source size was used for Monte Carlo CT simulations of a head phantom. A method to convert the reconstructed monoenergetic emissions of ^{155}Eu to SPR was presented. Images generated with the ^{155}Eu-CZT system were found to be quantitatively more accurate and contain less noise than those reconstructed with a typical 120 kV bremsstrahlung source spectrum. The proposed imaging modality provides a new alternative for 3D imaging for adaptive radiotherapy and proton therapy in particular.

References

1. Yan D, Vicini F, Wong J, Martinez A. Adaptive radiation therapy. *Physics in medicine and biology.* 1997;42(1):123.
2. Foroudi F, Wong J, Haworth A, et al. Offline adaptive radiotherapy for bladder cancer using cone beam computed tomography. *Journal of medical imaging and radiation oncology.* 2009;53(2):226-233.
3. Veiga C, Alshaikhi J, Amos R, et al. Cone-beam computed tomography and deformable registration-based "dose of the day" calculations for adaptive proton therapy. *International Journal of Particle Therapy.* 2015;2(2):404-414.
4. Kurz C, Nijhuis R, Reiner M, et al. Feasibility of automated proton therapy plan adaptation for head and neck tumors using cone beam CT images. *Radiation Oncology.* 2016;11(1):64.
5. Landry G, Nijhuis R, Dedes G, et al. Investigating CT to CBCT image registration for head and neck proton therapy as a tool for daily dose recalculation. *Medical physics.* 2015;42(3):1354-1366.
6. Kurz C, Dedes G, Resch A, et al. Comparing cone-beam CT intensity correction methods for dose recalculation in adaptive intensity-modulated photon and proton therapy for head and neck cancer. *Acta Oncologica.* 2015;54(9):1651-1657.
7. Guan H, Dong H. Dose calculation accuracy using cone-beam CT (CBCT) for pelvic adaptive radiotherapy. *Physics in medicine and biology.* 2009;54(20):6239.
8. Hatton J, McCurdy B, Greer PB. Cone beam computerized tomography: the effect of calibration of the Hounsfield unit number to electron density on dose calculation accuracy for adaptive radiation therapy. *Physics in medicine and biology.* 2009;54(15):N329.

9. Yang M, Virshup G, Clayton J, Zhu X, Mohan R, Dong L. Theoretical variance analysis of single- and dual-energy computed tomography methods for calculating proton stopping power ratios of biological tissues. *Physics in medicine and biology.* 2010;55(5):1343.
10. Hudobivnik N, Schwarz F, Johnson T, et al. Comparison of proton therapy treatment planning for head tumors with a pencil beam algorithm on dual and single energy CT images. *Medical physics.* 2016;43(1):495-504.
11. Zhu J, Penfold SN. Dosimetric comparison of stopping power calibration with dual-energy CT and single-energy CT in proton therapy treatment planning. *Medical Physics.* 2016;43(6):2845-2854.
12. Stewart PJ. Method for Radiography. *US Patent Office.* (1954;US2675368.
13. F.N.Case EHA, N.H.Cutshall. Production Study of Gadolinium-153. *Isotopes Division.* 1969;Oakridge National Laboratory.
14. KAERI NDCa. Table of γ -rays. *[online].*Available at : http://atom.kaeri.re.kr/.
15. Agostinelli S. Geant4 collaboration. *Nucl Instrum Methods A.* 2003;506(250):01368-01368.
16. D.E. Cullen JHH, L.Kissel. EPDL97: The Evaluated Photon Data Library '97 Version. *UCRL.* 1997;6 Rev.5.
17. Herman GT, Davidi R. Image reconstruction from a small number of projections. *Inverse problems.* 2008;24(4):045011.
18. Richmond C. ICRP publication 23. *International Journal of Radiation Biology and Related Studies in Physics, Chemistry and Medicine.* 1985;48(2):285-285.
19. Le HQ, Ducote JL, Molloi S. Radiation dose reduction using a CdZnTe-based computed tomography system: Comparison to flat-panel detectors. *Medical physics.* 2010;37(3):1225-1236.
20. Zhu J, Penfold SN. Total Variation Superiorization in Dual-energy CT Reconstruction for Proton Therapy Treatment Planning. *Inverse Problems submitted.* (2016.
21. Penfold S, Schulte RW, Censor Y, Rosenfeld AB. Total variation superiorization schemes in proton computed tomography image reconstruction. *Medical physics.* 2010;37(11):5887-5895.
22. Bazalova M, Carrier J-F, Beaulieu L, Verhaegen F. Dual-energy CT-based material extraction for tissue segmentation in Monte Carlo dose calculations. *Physics in medicine and biology.* 2008;53(9):2439.
23. Torikoshi M, Tsunoo T, Sasaki M, et al. Electron density measurement with dual-energy x-ray CT using synchrotron radiation. *Physics in medicine and biology.* 2003;48(5):673.
24. Landry G, Parodi K, Wildberger JE, Verhaegen F. Deriving concentrations of oxygen and carbon in human tissues using single-and dual-energy CT for ion therapy applications. *Physics in medicine and biology.* 2013;58(15):5029.
25. Schneider U, Pedroni E, Lomax A. The calibration of CT Hounsfield units for radiotherapy treatment planning. *Physics in medicine and biology.* 1996;41(1):111.
26. Berger MJ, Hubbell J, Seltzer S, et al. XCOM: photon cross sections database. *NIST Standard reference database.* 1998;8:87-3597.
27. Feuerlein S, Roessl E, Proksa R, et al. Multienergy Photon-counting K-edge Imaging: Potential for Improved Luminal Depiction in Vascular Imaging. *Radiology.* 2008;249(3):1010-1016.
28. H Li WG, J Bowsher, FF Yin. A dual cone-beam CT system for image guided radiotherapy: initial performance characterization. *Medical physics.* 2013;40(2).
29. Schafer S, W. Stayman J, Zbijewski W, Schmidgunst C, Kleinszig G, H. Siewerdsen J. Antiscatter grids in mobile C-arm cone-beam CT: Effect on image quality and dose. *Medical Physics.* 2012;39(1):153-159.

Chapter 6

Conclusion and future work

6.1 Conclusion

The process of obtaining accurate estimates of the stopping power of patient tissues is fundamentally important in proton therapy. In Chapter 2, a review of previous approaches to this task with X-ray imaging was presented. The critical examination led to new methods being formulated to address the limitations of previous approaches. As dual energy CT (DECT) is able to decompose imaged materials into electron density and effective atomic number, it was identified as a technique that is particularly well suited to the task of stopping power quantification.

The benefit of DECT in proton therapy was discussed and quantified for a particular test case in Chapter 3. By using phantoms of known composition and density, it was demonstrated that dose calculation with DECT was more accurate when compared to the traditional single energy CT (SECT) approach.

Despite the improved accuracy of stopping power ratio calculation, it was determined that improving image quality was imperative if DECT was to be used in a clinical setting. An iterative reconstruction algorithm[15] previously utilized in proton CT was modified for DECT with the goal of noise reduction. Image quality with the new reconstruction approach, as well as effect on proton therapy dose calculation accuracy was investigated in Chapter 4. Results indicated that not only was image quality enhanced, but the accuracy of proton therapy dose calculation with DECT could be further improved when images were reconstructed with total variation superiorization with diagonally relaxed orthogonal projections (TVS-DROP) rather than the conventional filtered backprojection method.

A relatively independent section of the thesis was presented in Chapter 5, describing a novel form of dual energy cone beam CT (DECBCT) for application in adaptive proton therapy. The proposed DECBCT system differed from previous investigations in CT spectra and method of photon detection. Specifically, a radioisotopic source of ^{155}Eu consisting of dual monoenergetic emissions was employed, rather than polyenergetic bremsstrahlung spectra. This approach removed difficulties associated with beam hardening and enabled the use of energy sensitive detector components for scatter correction in the reconstructed image. A pixelated cadmium-zinc-telluride (CZT) detector panel was simulated for this purpose. Simulations with the Monte Carlo toolkit Geant4 allowed for a comparison of stopping power ratio calculation accuracy with the proposed detector and that of a conventional CBCT module commonly used in radiotherapy. Results indicated that such an imaging system has potential to be used for real-time online dose adaption in proton therapy.

6.2 Future work

With the increasing availability of commercial dual energy CT scanners, it is envisioned that this imaging technique will become the standard of care in proton therapy treatment planning. However, for clinical use, a consistent method for utilizing these images in commercial proton therapy treatment planning systems (TPS) must be devised. As an initial step, extension of the popular Geant4 toolkit TOPAS[16] allowing for the conversion of DECT DICOM images to stopping power ratio (SPR) would be of great value.

Perhaps the most exciting avenue for future work lies in the construction of a prototype ^{155}Eu-CZT DECBCT system. A small prototype system would allow for an experimental validation of the simulation results presented in this thesis. Future work must quantify and compare the image quality and accuracy of reconstructed values when using this form of imaging. In addition, the ability to view images of Z_{eff} with DECT and DECBCT may have further applications in soft tissue definition for treatment plan targeting and soft tissue matching in image guided radiotherapy.

DECT is just one of several new directions for image guided radiotherapy. Another interesting branch is that of proton computed tomography (pCT). A number of groups are investigating the use of pCT for proton therapy treatment planning. To achieve pCT images with a spatial resolution comparable to X-ray based imaging, sophisticated detector hardware and computationally intensive image reconstruction algorithms are required. As these new modalities reach maturity, it will be important to quantify the benefit of using these techniques through clinical trials.

Bibliography

[1]R.R. Wilson, "Radiological use of fast protons," Radiology **47**, 487-491 (1946).

[2]R. Wilson, "Brief history of the Harvard University cyclotrons," (2003).

[3]T.I. Yock, N.J. Tarbell, "Technology insight: Proton beam radiotherapy for treatment in pediatric brain tumors," Nature Clinical Practice Oncology **1**, 97-103 (2004).

[4]C. Tobias, J. Lawrence, J. Born, R. McCombs, J. Roberts, H. Anger, B. Low-Beer, C. Huggins, "Pituitary irradiation with high-energy proton beams a preliminary report," Cancer Research **18**, 121-134 (1958).

[5]Particle Therapy Co-Operative Group, "Particle therapy facilities in operation (last update: Sep-2016)," 2016).

[6] Particle Therapy Co-Operative Group, "Particle Therapy Patient Statistics (per end of 2015)," 2016).

[7]H. Bichsel, "Passage of charged particles through matter," (California Univ., Berkeley (USA). Dept. of Physics, 1969).

[8]U. Schneider, E. Pedroni, A. Lomax, "The calibration of CT Hounsfield units for radiotherapy treatment planning," Physics in medicine and biology **41**, 111 (1996).

[9]ICRU, "Tissue Substitutes in Radiation Dosimetry and Measurement," International Commission on Radiation Units and Measurements Report 44 (1989).

[10]R. Rutherford, B. Pullan, I. Isherwood, "Measurement of effective atomic number and electron density using an EMI scanner," Neuroradiology **11**, 15-21 (1976).

[11]M. Yang, G. Virshup, J. Clayton, X. Zhu, R. Mohan, L. Dong, "Theoretical variance analysis of single-and dual-energy computed tomography methods for calculating proton stopping power ratios of biological tissues," Physics in medicine and biology **55**, 1343 (2010).

[12]R.A. Brooks, "A quantitative theory of the Hounsfield unit and its application to dual energy scanning," Journal of computer assisted tomography **1**, 487-493 (1977).

[13]D. Yan, F. Vicini, J. Wong, A. Martinez, "Adaptive radiation therapy," Physics in medicine and biology **42**, 123 (1997).

[14]F. Foroudi, J. Wong, A. Haworth, A. Baille, J. McAlpine, A. Rolfo, T. Kron, P. Roxby, A. Paneghel, S. Williams, "Offline adaptive radiotherapy for bladder cancer using cone beam computed tomography," Journal of medical imaging and radiation oncology **53**, 226-233 (2009).

[15]S. Penfold, R.W. Schulte, Y. Censor, A.B. Rosenfeld, "Total variation superiorization schemes in proton computed tomography image reconstruction," Medical physics **37**, 5887-5895 (2010).

[16]J. Perl, J. Shin, J. Schümann, B. Faddegon, H. Paganetti, "TOPAS: an innovative proton Monte Carlo platform for research and clinical applications," Medical physics **39**, 6818-6837 (2012).